#### POLITECNICO DI TORINO

Master's Degree in Georesources and Geoenergy Engineering



#### Master's Degree Thesis

# Experimental Characterization of the Relative Permeabilities for $CO_2$ -Water Systems

Supervisors

Candidate

Prof. Francesca

Youssef SWEIDAN

**VERGA** 

Co-Supervisors

Costanzo PETER Alessandro SURIANO

November 2025

## Abstract

In 2019, the European Union committed to achieving net-zero greenhouse gas emissions by 2050 through the European Green Deal, emphasizing the urgent need for mitigation technologies such as Carbon Capture and Storage (CCS). The efficiency of geological  $CO_2$  storage strongly depends on the fate of injected  $CO_2$ , which is governed by the relative permeability functions of  $CO_2$ -brine systems. These curves affect plume migration, residual trapping, injectivity, and surface facility design. However, reported measurements in the literature show significant variability, largely due to differences in laboratory protocols and the influence of capillary end effects (CEE).

The thesis focused on finding the best method and practices for measuring the relative permeability for supercritical carbon dioxide  $(scCO_2)$ -brine systems. It described the two methods that measures the relative permeability, steady state (SS) and unsteady state (USS), with the criticalities of using a compressible fluid  $(scCO_2)$ , and their effect on the measurement. The SS method, which adopt the mathematical approach modified intercept method (MIM) for overcoming the CEE is the most accurate, although its time consuming and exhausting. For the USS methods, using local measurement for pressure drop and saturation measurement gives a fast but not precise result for imbibition, while the results for drainage are not reliable due to viscous fingering phenomena.

## Acknowledgements

I would like to express my deepest gratitude to my supervisor, **Prof. Francesca Verga**, for her invaluable guidance and encouragement. Her expertise and continuous support have been fundamental in shaping both my technical understanding and academic growth. I would also like to thank **Dr. Alessandro Suriano** and **Dr. Costazo** Peter for their patience and for following up with me throughout my research, as well as for their technical support during the core flooding experiments. I am also thankful to my colleagues at Politecnico di Torino, whose collaboration and insightful discussions created a stimulating working environment. Their friendship and willingness to share knowledge made this research experience both productive and enjoyable. Finally, I am profoundly grateful to my family and friends for their unconditional love, patience, and encouragement, which have been a constant source of motivation during this journey.

## Table of Contents

$\mathbf{A}$	Abstract List of Figures  V										
Li											
1	Intr	Introduction									
	1.1	Clima	te Change and Need for Decarbonization	. 1							
	1.2		on Capture and Storage Technology								
		1.2.1	Carbon Dioxide Capture								
		1.2.2	Carbon Dioxide Transport								
		1.2.3	Carbon Dioxide Geological Storage	. 4							
	1.3	Carbo	on Dioxide Trapping Mechanisms								
	1.4		of the Work								
2	Res	Reservoir Rock Properties									
	2.1		ity	. 7							
	2.2		ation								
	2.3		ute Permeability								
	2.4	Surfac	ce and Interfacial Tension	. 14							
	2.5	Wetta	bility	. 15							
	2.6	Capill	lary Pressure	. 16							
	2.7	Relati	ive Permeability	. 17							
3	App	Apparatus Used and Procedure Followed for Measurement of $scCO_2$ -Brine									
	Rel	ative F	Permeability in the Laboratory	19							
	3.1	Appar	ratus Used	. 19							
	3.2	Equip	ments	. 20							
	3.3		xperiment Preparation for $CO_2$ -Brine Systems								
	3.4	Procee	dure	. 21							
		3.4.1	Steady State	. 21							
		3.4.2	Unsteady State	. 22							
4	Rel	Relative Permeability Measurement 2-									
	4.1	Steady	y-State Technique	. 24							
	4.2	Unstea	ady State Technique	. 27							
		4.2.1	Fractional Flow Equation								
		4.2.2	Buckley-Leverett Theory								
		4.2.3	Welge's Extension Solution								
		424	Johnson-Bossler-Naumann Method	35							

		4.2.5	Applying for $scCO_2$ -Brine Systems	37				
5	Capillary End Effect							
	5.1	Steady	State Experiments	40				
			Modified Intercept Method					
	5.2	Unstea	ady State Experiments	50				
		5.2.1	Extended JBN Method	50				
	5.3	Endpo	ints Determination	55				
6	Core Sample Selection and the Conditions of the Experiment Effect on							
		-	Permeability Curves	57				
	6.1	Choos	ing the Core Sample	57				
	6.2	Condi	tions of the Experiment	59				
		6.2.1	Thermophysical Properties of the Fluids	59				
		6.2.2	Impact of Thermophysical Properties on Relative Permeability	62				
		6.2.3	Equilibration of the Fluids	64				
7	Disc	cussion	l	66				
8	8 Conclusion							
Bi	Bibliography							

## List of Figures

1.1	Global GHG Emissions by Sector[2]	1
1.2	Local Temperature in 2022 relative to the average temperature in 1951-	0
1 9	1980[5]	2
1.3 1.4	Annual $CO_2$ Emissions from Fossil Fuels and Industry[7] Location of sites where activities relevant to $CO_2$ storage are planned or	
1 -	under way $[9]$	3
1.5	Options for storing $CO_2$ in deep underground geological formations[9]	5
2.1	Conceptual representation of different types of pores in a reservoir rock[21]	8
2.2	Schematic illustration of a helium porosimeter[21]	9
2.3	Schematic of a retort distillation unit[21]	10
2.4	Schematic of a Dean-stark extraction unit[21]	10
2.5	Conceptual illustration of permeability of a reservoir rock[22]	11
2.6	Illustration of displacement apparatus for absolute permeability measure-	
	ment[21]	13
2.7	Linear extrapolation of apparent gas permeability vs reciprocal mean pres-	
	sure[21]	14
2.8	Illustration of cohesive and adhesive forces [24]	14
2.9	The concept of surface tension between two immiscible fluids[20]	15
2.10	The concept of interfacial tension between two immiscible liquids[21]	15
2.11	Contact angle and Wettability [20]	16
2.12	Illustration of the meniscus between wetting and non-wetting phase [26]	16
	Capillary pressure curve [20]	17
2.14	Relative Permeability Curves [28]	18
3.1	RPS700 Main Unit [29]	19
4.1	$CO_2$ density variation with pressure and temperature [32]	26
4.2	$CO_2$ viscosity variation with pressure and temperature [32]	26
4.3	A typical fractional flow curve for a range of relative permeabilities [21]	29
4.4	Schematic of the homogeneous porous media and the volume element $A\phi dx$	
	that is considered for the application of conservation of mass equation for	
	development of Buckley-Leverett theory [21]	30
4.5	$df_w/dS_w$ versus water saturation plot[21]	31
4.6	Buckley-Leverett solution to the physically impossible situation [21]	31
4.7	Water saturation profiles for various $Q_{\text{wi}}$ [21]	32
4.8	Water saturation distribution as function of position at a fixed time t, prior	
	to breakthrough time [21]	33

4.9	Welge's tangent (extension) solution [21]	34
4.10	Determination of average water saturation after breakthrough [20]	34
4.11	Viscous Fingering Phenomena [36]	38
5.1	Capillary End Effect [21]	41
5.2	Sw profile in SS condition in water wet system [37]	44
5.3	Relative permeability curves obtained from the known relative permeability	
	functions [37]	47
5.4	Water saturation profile at SS conditions for different flow rates at same F	
	in a water-wet system [37]	48
5.5	Average water saturation in the core vs reciprocal oil flow rate [37]	48
5.6	Pressure drop in the core vs oil flow rate [37]	48
5.7	Comparison of corrected relative permeability data and original curves [37]	49
5.8	Average water saturation in the core vs reciprocal oil flow rate for oil-wet	40
<b>-</b> 0	systems [37]	49
5.9	Water saturation profile at different injection times [39]	52
	Pressure drop at each section with respect to injected pore volumes [39]	52
	Water fractional flow [39]	53
	Fitted data and measured relative permeability	54 55
0.10	Comparison between SS results and extended JBN results [39]	55
6.1	Effect of wettability on relative permeability curves [40]	58
6.2	$CO_2$ density and viscosity variation with pressure and temperature	59
6.3	Brine density and viscosity variation with pressure and temperature	60
6.4	Brine density variation with salt concentration [41]	61
6.5	Interfacial tension of $CO_2$ -brine system at different pressure, temperature,	0.1
c c	and salinity [17]	61
6.6	Comparison of $CO_2$ -brine relative permeability curves at viscosity ratios	
	of 0.034 and 0.044 under constant interfacial tension (35.9 mN/m) during	co
6.7	drainage and imbibition [42]	62
6.7	Comparison of $CO_2$ -brine relative permeability curves at IFT of 35.9 mN/m	
	and 53.7 mN/m under constant viscosity ratio (0.034) during drainage and imbibition [42]	63
6.8	Illustration of the variation of $CO_2$ and brine solubility with temperature	03
0.0	at constant pressure (90 bars)[16]	65
		,,,,

## Chapter 1

### Introduction

#### 1.1 Climate Change and Need for Decarbonization

One of the biggest concerns in the world today are climate change and global warming. This problem does not affect specific category or area, but it impacts the entire planet. That is why governments are working together and combining their efforts to face this serious threat that if it is not dealt with responsibly, its consequences could be disastrous for the whole planet. In 2019, the European Green Deal was agreed among the European Union countries as a result of combined efforts of their governments to confront the crisis of global warming. This deal aims to reduce net greenhouse gas emissions by at least 55% by 2030 and to achieve climate neutrality by 2050. These goals reflect a growing global agreement on the need to transition to a low-carbon economy through innovation, energy efficiency, renewable energy, and carbon capture technologies[1].

The main cause of global warming and climate change are greenhouse gases, which are mainly emitted from power generation and industry that represented 58% of total emissions in 2019[2] as shown in the figure 1.1. Greenhouse gases naturally exist in the atmosphere and help maintain a habitable temperature by absorbing infrared radiation emitted by the Earth. However, human activities have increased their concentration, which leads to a rise in global temperatures above normal levels.

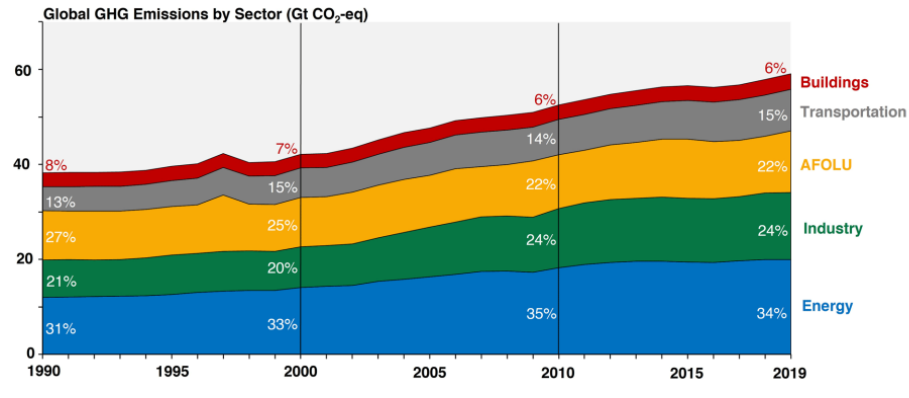


Figure 1.1: Global GHG Emissions by Sector[2]

In 2015, Paris agreement was established by 195 parties at the UN Climate change

conference (COP21) in Paris, France to limit the increase in global temperature level to 1.5 °C above pre-industrial levels to reduce the repercussions of climate change such as severe heatwaves, droughts, sea level rise, and flooding [3, 4]. However, this didn't prevent average temperature in some areas to reach 5 °C above the pre-industrial levels in 2022 as shown in the following figure.

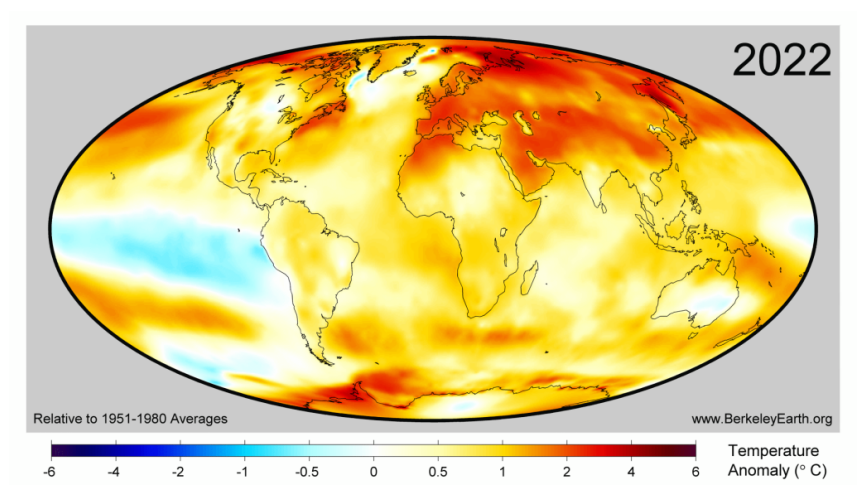


Figure 1.2: Local Temperature in 2022 relative to the average temperature in 1951-1980[5]

CO<sub>2</sub> is the main driver of global warming caused by greenhouse gas emissions on the long term, it represents around 80% of the human-caused greenhouse gas emissions [6], the emissions follow an exponential trend since the onset of industrial revolution breaking a record of 36.3 Gt in 2021, this increase forced governments and policymakers to meet the energy demand by developing environmentally friendly and low-carbon technologies[4].

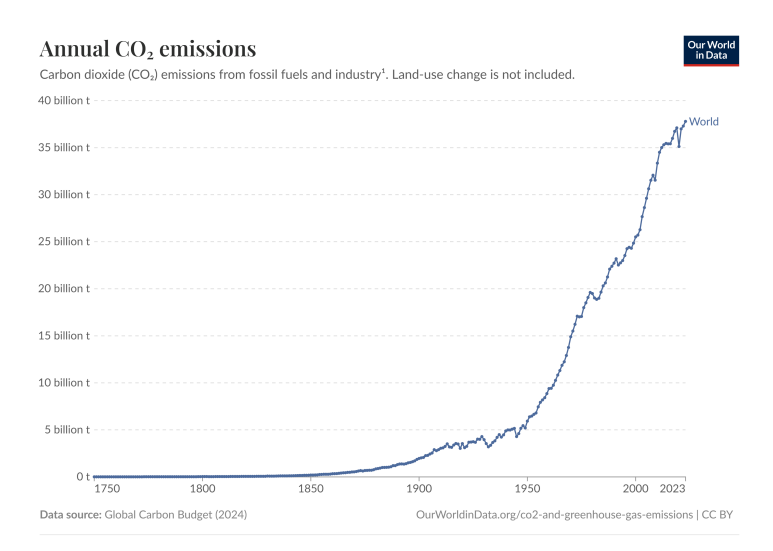


Figure 1.3: Annual CO<sub>2</sub> Emissions from Fossil Fuels and Industry[7]

Among the various solutions explored to reduce greenhouse gas emissions, one promising approach is the underground storage of carbon dioxide. This has sparked extensive research into  $CO_2$  storage and its behavior in subsurface environments.

#### 1.2 Carbon Capture and Storage Technology

Achieving the Paris agreement goal of limiting the global temperature increase to 1.5 °C above pre-industrial levels depends not only on technologies that reduce emissions into the atmosphere, but also on technologies that capture emitted gases and store them underground [8].

Carbon Capture and Storage is the technology that involves capturing  $\mathrm{CO}_2$  emissions from sources such as power generation and industrial processes, transporting it using ships or pipelines to the storage site where they will be injected into deep geological formations for permanent storage.

The first attempt to inject  $CO_2$  into an underground geological formation was in Texas, USA, in 1970, for the purpose of enhanced oil recovery (EOR). In 1996, the first project in the world to store  $CO_2$  underground was launched at the Sleipner Gas Field in the North Sea by Statoil and its partners. This project increased the interest of many countries and oil companies in geological storage as part of the solution to reduce emissions. Today, it has become one of the key options for climate change mitigation [9].

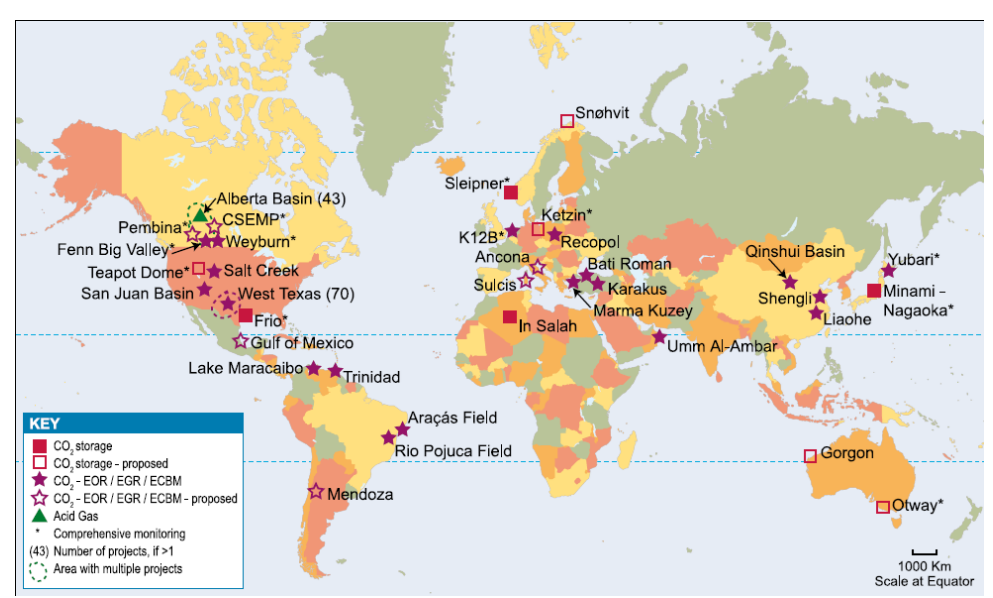


Figure 1.4: Location of sites where activities relevant to  $CO_2$  storage are planned or under way[9]

#### 1.2.1 Carbon Dioxide Capture

The first stage of carbon capture and storage (CCS) technology is the capture of  $CO_2$ , which can be carried out using three main methods. **Post-Combustion capture** is the most popular technique, where  $CO_2$  is captured from flue gases after combustion of fossil fuels. This is typically achieved through solvent absorption, adsorption, calcium looping, and membrane separation [10]. This method is energy intensive due to low concentration of  $CO_2$  in flue gases. Another approach is **Pre-Combustion capture**, in which  $CO_2$  is removed from fossil fuels before combustion. This process begins by applying steam reforming or gasification to the fuels under high pressure and temperature

to produce synthetic gas, a mixture primarily composed of hydrogen and carbon monoxide, then CO undergoes a water-gas shift reaction to convert carbon monoxide and water to additional hydrogen and carbon dioxide. The resulting high  $CO_2$  concentration makes separation more efficient [11]. The  $CO_2$  is the transported and stored, while hydrogen is used for electricity generation. The most effective approach among the three is **Oxyfuel Combustion** where fossil fuels is burned with pure oxygen instead of air, producing a flue gas containing  $CO_2$  and water vapor. This mixture is cooled leading to the condensation of water leaving  $CO_2$  free to be transported and stored [12].

#### 1.2.2 Carbon Dioxide Transport

Following the capture stage, the transportation phase takes place, which can be implemented through three main approaches. **Pipelines** top the list as the most effective way to accommodate the massive volumes of carbon captured from CCS projects, in addition to pre-existence of the pipeline networks from previous activities in most cases, which helps reduce costs and minimize environmental impact. **Truck and rail** are more suitable for small onshore projects where no existing pipeline infrastructure is available and constructing a new one is not economically feasible. For offshore projects that are not served by pipeline networks, **ship transportation** presents a viable alternative, particularly for small-scale operations [13].

#### 1.2.3 Carbon Dioxide Geological Storage

The assessment of a site for a long-term  $CO_2$  storage requires evaluating the following elements:

- Storage Capacity: Directly proportional to the pore volume, where the site must have sufficient pore volume for compressed CO<sub>2</sub> containment.
- **Injectivity:** Is evaluated based on permeability, having a higher permeability reservoir allows higher injection rates.
- **Integrity:** Presence of a sealing layer that ensures the containment of the stored fluid.
- **Depth:** The depth must provide sufficient pressure and temperature, to store CO<sub>2</sub> in supercritical phase which allows storing a large quantity due to liquid like density, and easy flow due to gas-like viscosity.

Storage options is not limited to **depleted oil and gas reservoirs**, rather it extends to include **saline formations**, **unmineable coal seams**, **basalt formations**, **and Organic-rich shales**. The most important are the following:

- Depleted Oil and Gas Reservoirs: A good knowledge about the characteristic of the reservoir is already known, in addition to proven ability to trap gas on a geological timescale.
- Saline Formations: Are spread worldwide and characterized by their large capacity for storing CO<sub>2</sub>. No previous knowledge about the characteristics of the formation and formation original pressure must be exceed to displace water[14].

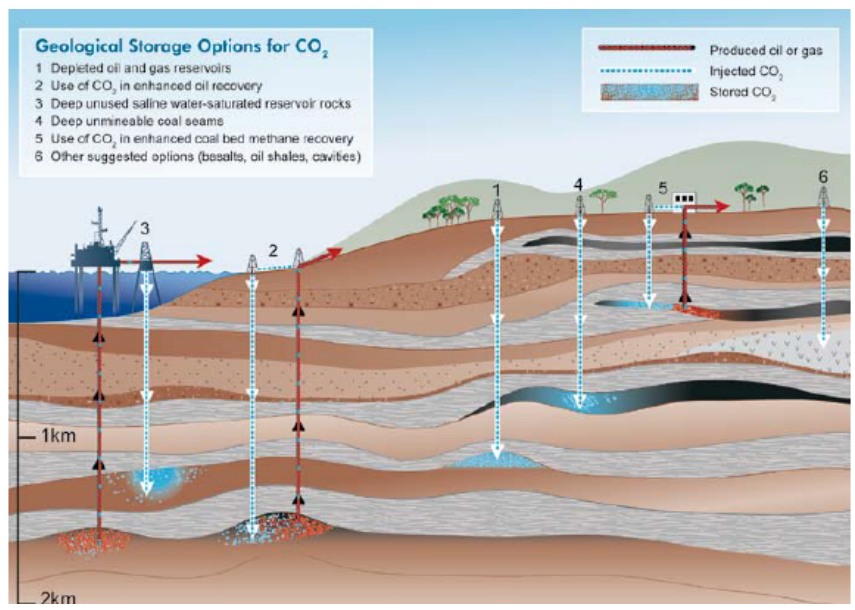


Figure 1.5: Options for storing CO<sub>2</sub> in deep underground geological formations[9]

#### 1.3 Carbon Dioxide Trapping Mechanisms

The fate of injected  $CO_2$  is one of the most frequently raised questions among engineers, environmental scientists, geologists, and even the general public. Concerns about potential leakage and long-term containment remain central to discussions on the safety and effectiveness of geological storage. Stored  $CO_2$  is trapped in different mechanisms:

- Structural/Stratigraphic Trapping: After injection, CO<sub>2</sub> migrates upward due to buoyancy relative to formation water until it encounters an impermeable seal (anticline, fault, pinch-out, unconformity). This mechanism prevents vertical leakage of CO<sub>2</sub>. Once trapped beneath the seal, lateral migration may occur along the top of the aquifer, a process known as hydrodynamic trapping.
- Residual trapping: As the CO<sub>2</sub> plume advances, imbibition of brine at the trailing edge disconnects the once-continuous CO<sub>2</sub> phase into isolated ganglia. These disconnected bubbles remain immobilized by capillary forces, forming residual trapping.
- Solubility Trapping: At the CO<sub>2</sub>-brine interface, CO<sub>2</sub> gradually dissolves into the aqueous phase. Solubility depends on reservoir pressure, temperature, pH, salinity, and brine composition. Dissolved CO<sub>2</sub> increases brine density, leading to convective mixing and downward migration, while less saturated brine replaces it. This process is relatively slow and may take thousands of years for significant dissolution.
- Ionic Trapping: Dissolved CO<sub>2</sub> forms carbonic acid, which dissociates into bicarbonate and carbonate ions. This mechanism depends strongly on pH (enhanced at pH > 6) and represents an intermediate step toward mineral trapping.
- Mineral Trapping: Over long timescales, acidic brine reacts with reservoir minerals, releasing cations such as  $Ca^{2+}$ ,  $Mg^{2+}$ , and  $Fe^{2+}$ . These cations combine with carbonate ions to precipitate stable carbonate minerals (e.g., calcite, magnesite, siderite). Mineral trapping occurs over millennia to geologic timescales and represents the most secure and permanent form of  $CO_2$  storage [15].

The fate of the injected CO<sub>2</sub> plume is distributed among these mechanisms. While mineral trapping represents the most secure and permanent for storage, its contribution is limited due to the geological timescale required for mineralization. Structural/stratigraphic trapping that represents the primary trapping mechanism[16], although effective, pose the greatest concern regarding potential leakage if caprock integrity is compromised. In contrast, residual trapping the secondary trapping mechanism[16], is highly effective in the short and long term, making it a particularly desirable mechanism for ensuring storage security.

Relative permeability and capillary pressures control the spread of CO<sub>2</sub> plumes in the reservoir, in addition to a direct determination of residual trapping quantity [16]. In fact, the author of [15] demonstrated through a 200-year simulation sensitivity analysis that varying relative permeability parameters leads to systematic shifts in the partitioning of CO<sub>2</sub> among different trapping mechanisms. Relative permeability also exerts a direct influence on well injectivity and sizing surface facilities [16], also it is a critical parameter in all mathematical models used to predict CO<sub>2</sub> migration and storage performance. Accordingly, accurate determination of relative permeability curves is essential for reliable design and assessment of CCS projects [17].

#### 1.4 Scope of the Work

Significant variability in relative permeability curves for the  $\rm CO_2$ -water system has been reported in the literature, as highlighted by the Global CCS Institute and Stanford University [18]. This variability cannot be attributed solely to differences in experimental conditions, but rather to the methodologies and protocols applied during laboratory measurements. Two main laboratory approaches are commonly used: the steady-state method, based on simultaneous co-injection of fluids, and the unsteady-state method, which relies on displacement experiments analyzed by history matching. However, there remains considerable debate on the most appropriate protocols to ensure reliable results [16]. The objective of this work is to review these methodologies and identify best practices to obtain the most robust and reproducible relative permeability data for  $\rm CO_2$ -water systems.

## Chapter 2

## Reservoir Rock Properties

Porous media, or reservoir rock, is a subsurface rock capable of storing fluids within its pores and transmitting them through its connected pore network. The lithology varies and may include sandstone, limestone, or dolomite, with either unconsolidated or consolidated structures. To understand and predict fluid flow behavior underground, rock properties are studied through laboratory tests performed on core samples extracted from the reservoir. These tests fall into two categories: Routine Core Analysis (RCAL), which determines formation properties, and Special Core Analysis (SCAL), which characterizes fluid—rock interactions[19].

#### 2.1 Porosity

During sediment deposition, the irregular shape and varying sizes of grains create void spaces between them, known as porosity, within a consolidated rock. These pores that can't be observed by naked eye due to their microscopic size, forms the storage capacity for fluids[20][21]. Generally, this property of reservoir is defined as the ratio of the pore volume to the bulk volume of the rock, and is expressed mathematically as follows:

$$\phi_t = \frac{\text{Pore Volume}}{\text{Bulk Volume}} \tag{2.1}$$

where  $\phi_t$  denotes total porosity.

For reservoir engineers, the property of interest is the *effective porosity*, which represents the fraction of the pore space that can contribute to fluid flow. This may include interconnected pores and, in some cases, dead-end pores, while isolated pores are disregarded since they do not allow hydrocarbon movement. Figure 2.1 illustrates the difference between pore types. Variations between total and effective porosity arise primarily from excessive cementation during sediment deposition, which can isolate portions of the void space[20][21]. Effective porosity can be expressed as:

$$\phi_e = \frac{\text{Interconnected Pore Volume} + \text{Dead-End Pore Volume}}{\text{Bulk Volume}}$$
(2.2)

where  $\phi_e$  denotes the effective porosity.

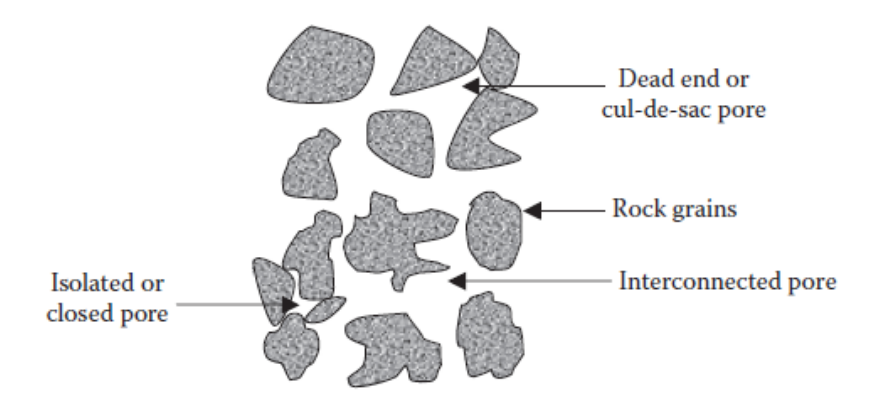


Figure 2.1: Conceptual representation of different types of pores in a reservoir rock[21]

Porosity is classified as *original porosity* or *induced porosity* according to its origin. Primary, or original, porosity is created at the time of deposition due to the irregular shape of sediments, which leave voids between particles. It is commonly present in sandstones. Secondary, or induced, porosity develops later after deposition, due to geological process that causes fracture and vugs. This type is commonly found in limestone [21].

Porosity can be measured by two main techniques: routine core analysis, which is the most common, and well log interpretation, which is indirect method. In routine core analysis, a helium porosimeter is used. This apparatus consists of two chambers, reference chamber and sample chamber connected to a helium supply. The core sample is placed in the sample chamber, and isolated from reference chamber which has a known volume. After pressurizing the reference chamber with helium, the valve between the two chambers is opened until equilibrium is reached (same pressure in the two chambers)[21].

Using Boyle's law  $(P_1V_1 = P_2V_2)$ ,  $V_2$  is calculated, and by subtracting the bulk volume of the core sample (measured using a caliper), the pore volume is obtained. Helium or Nitrogen is chosen to perform this experiment because it is inert, ensuring no reaction occurs between the gas and the rock that could change the original porosity. In addition, its small molecules can penetrate tiny pores rapidly, allowing the experiment to be completed in short time[21].

Porosity can also be determined indirectly from well logs. The three main log types used are the density log, neutron log, and sonic log. These rely on correlations between the measurements and porosity, using certain rock and fluid properties.

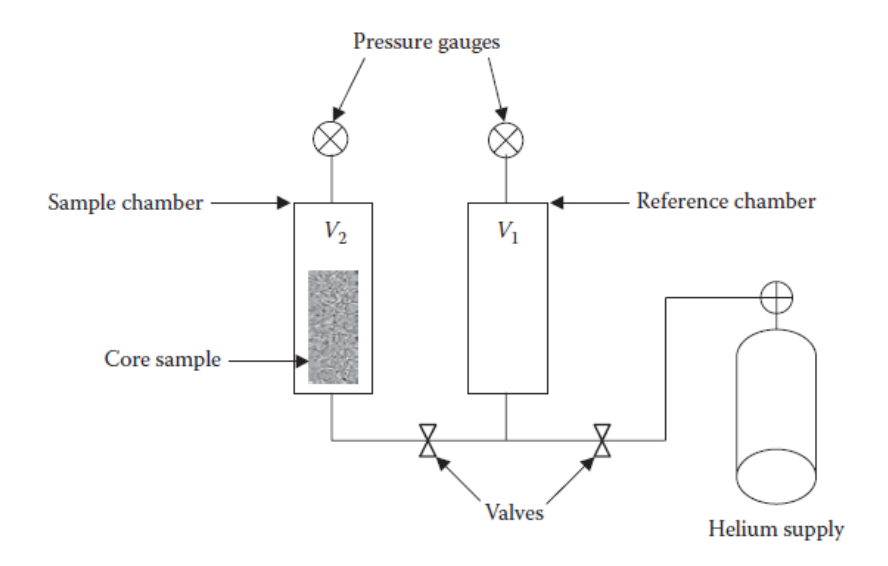


Figure 2.2: Schematic illustration of a helium porosimeter[21]

#### 2.2 Saturation

Porosity is defined as the storage capacity for all fluids present in the reservoir, including water. Saturation represents the fraction of the pore volume occupied by a specific fluid. In other words, it quantifies the volume of the typical reservoir fluids: water, oil, and gas, to estimate the amount of hydrocarbons[21].

The general mathematical expression of saturation is:

fluid saturation = 
$$\frac{\text{total volume of specific fluid}}{\text{pore volume}}$$
 (2.3)

Here, pore volume refers to the effective pore volume. Since all saturations are normalized to the pore volume, the sum of all fluid saturation is 1:

$$S_a + S_o + S_w = 1 (2.4)$$

This simple but important property is one of the pillars of reservoir engineering. It is directly linked to properties such as relative permeability and capillary pressure, which would be meaningless without knowing the saturation of each fluid phase. Moreover, accurate measurement of saturations helps determine pore volume, and therefore porosity, if the bulk volume is known[21].

Saturation can be expressed with different subscripts depending on its meaning. The most important are:

- Critical gas saturation,  $S_{gc}$ : The minimum gas saturation for gas to be mobile.
- Residual gas saturation,  $S_{gr}$ : Gas trapped by water in the reservoir after a displacement process.
- Residual oil saturation, S<sub>or</sub>: Oil trapped by water in the reservoir after a displacement process.

• Irreducible water saturation,  $S_{wi}$ : Minimum fraction of the pore volume occupied by water that cannot be reduced or removed under a pressure gradient[20].

Saturations can be measured by **direct** or **indirect** methods. As for direct measurements, the core of the approach is removing liquids from a solid which is known as leaching. This approach can be performed in two methods, the first one is called *retort distillation* which extract fluids using heat, and the other one is named *Dean-Stark* extraction which uses heat and an organic solvent to extract fluids from pores. While the indirect method is based on well logs that measure saturation at different depths which is not of interest here[21].

- Retort Distillation: The experiment is performed using retort distillation apparatus which include three main components: a heating unit, a condenser tube, and a receiver tube as illustrated in figure 2.3. The core sample is placed in the heating unit and subjected to high temperature, causing oil and water to vaporize. The vapors condense and are collected in the receiver tube. Saturations are then calculated using the equations discussed earlier[21].
- Dean-Stark Extraction: This technique uses distillation with an organic solvent (toluene). The setup includes a long-neck round-bottom flask filled with toluene, a heat source, a condenser, and a graduated tube receiver. Toluene is heated to its boiling point, and the vapor passes through the rock sample, extracting oil and water. The vapor is then condensed, producing two phases: water and a mixed hydrocarbon phase containing oil and toluene. Water, being denser, settles at the bottom of the tube and can be measured directly. Gas and oil saturations are determined indirectly[21].

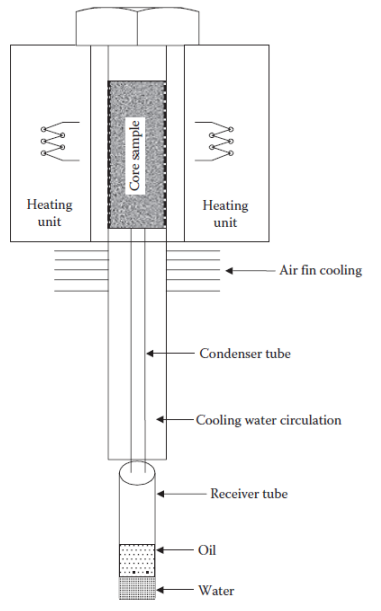


Figure 2.3: Schematic of a retort distillation unit[21]

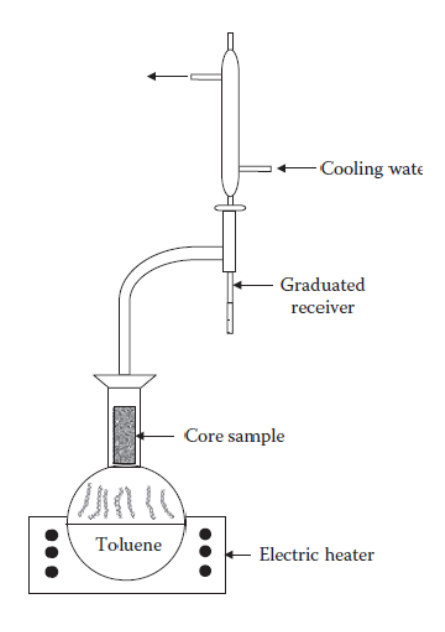


Figure 2.4: Schematic of a Deanstark extraction unit[21]

#### 2.3 Absolute Permeability

Fluid flow through the interconnected pores of the reservoir rock is due to a property called permeability. It describes how easily the formation can transmit fluids. When the rock is completely saturated with a single fluid, this property is referred to as absolute permeability. Since this property is dynamic (requires flow), measuring it in the lab requires conducting flow experiments[21].

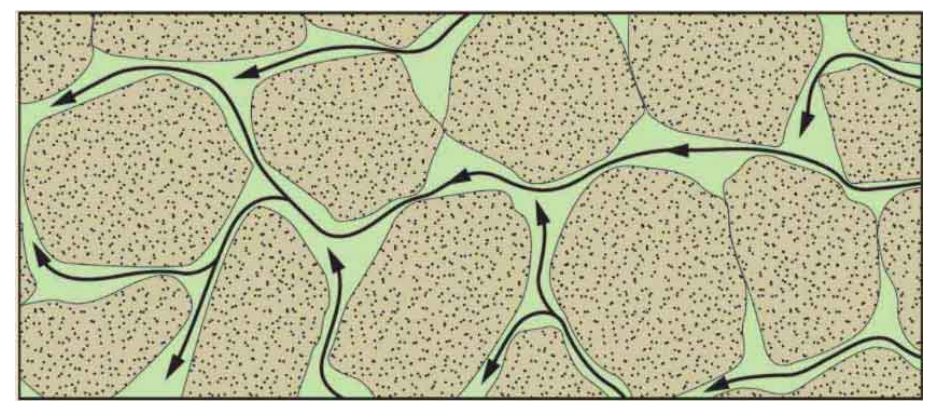


Figure 2.5: Conceptual illustration of permeability of a reservoir rock[22].

The following mathematical equation was developed by Darcy for the flow of water through sand:

$$Q = KA \frac{h_1 - h_2}{L} \tag{2.5}$$

Darcy's experiment is conceptually similar to fluid flow through a core plug. The main difference is orientation: Darcy's test was vertical, whereas core-flooding experiments are typically horizontal. Since Darcy equation was limited only to water as the flowing fluid, some updates were implemented to include other fluids by adding their viscosity, then integrating between limits, the equation become as follows:

$$Q = \frac{kA\Delta P}{\mu L} \tag{2.6}$$

where

Q: flow rate $(m^3/s)$ 

k: absolute permeability  $(m^2)$ 

A: cross-sectional area  $(m^2)$ 

 $\Delta P$ : pressure drop  $(N/m^2)$ 

 $\mu$ : fluid viscosity  $(Ns/m^2)$ 

L: length (m)

The following assumptions was done by Darcy when developing the equation:

- Core plug is saturated with single fluid only
- Incompressible fluid is flowing
- No interactions between the core plug and flowing fluids
- Flow is laminar

#### • Steady state conditions

Absolute permeability is an intrinsic property of the porous rock, as it doesn't depend on the fluid flowing in the rock. In other words, whatever fluid passes through the rock, it will result in the same value of permeability, as the pressure drop is scaled according to the flow rate and viscosity of the fluid. Darcy is the unit used for permeability measurement. Most reservoirs have permeability less than 1 Darcy, and to have a better visualization for permeability values, millidarcy is used, where 1 Darcy = 1000 md.

When dealing with a heterogeneous rock, and for the sake of obtaining accurate measurements of permeability, it is better to perform the laboratory analysis on the whole core instead of core plugs. Experiments performed on cores drilled parallel to the bedding planes determine horizontal permeability  $k_h$ , while vertical permeability  $k_v$  is determined for cores drilled perpendicular to the bedding planes. It must be kept in mind that cores may not be representative of the reservoir due to heterogeneity, in addition to the possibility of alteration of core original permeability during preparation[20][21].

Displacement apparatus is the name given to the apparatus that measure absolute permeability. This flow experiment is performed on core samples that are totally dried, with defined dimensions, using gases or nonreactive liquids, to measure individual variables for the direct application of Darcy equation. The setup of the apparatus is shown in figure 2.6.

- Measuring Absolute Permeability Using Liquids: Fluids used in performing this measurement could be brine, crude oil, or synthetic oil. The dried core plug is placed inside a sleeve that will be placed inside the core holder. The core plug is confined under a certain pressure to restore reservoir conditions, and ensure no flow of liquid between the core plug and sleeve. Reservoir temperature conditions is served by a climatic air bath. Fluid is pumped to the core sample at either a constant rate or constant differential pressure, and data is recorded. Viscosity is measured at reservoir conditions. All variables are available to apply Darcy's equation and determine permeability.
- Measuring Absolute Permeability Using Gases: This method is preferred over liquids because gas is clean, non-reactive, and doesn't alter the pore network. Nitrogen, helium, or air are the gases used. The procedure is mainly the same as for liquids, with the only difference being that only constant differential pressure can be applied. Darcy's equation cannot be applied directly to gases since it was developed for incompressible fluids. The gas flux increases with flow due to pressure drop and gas expansion, so Darcy's has been modified to:

$$Q_2 = \frac{kA(P_1^2 - P_2^2)}{2\mu L P_2} \tag{2.7}$$

where

 $Q_2$ : outlet flow rate $(m^3/s)$  k: absolute permeability  $(m^2)$  A: cross-sectional area  $(m^2)$  $P_1$ : inlet pressure  $(N/m^2)$   $P_2$ : outlet pressure  $(N/m^2)$   $\mu$ : gas viscosity  $(Ns/m^2)$ L: length of the sample (m)

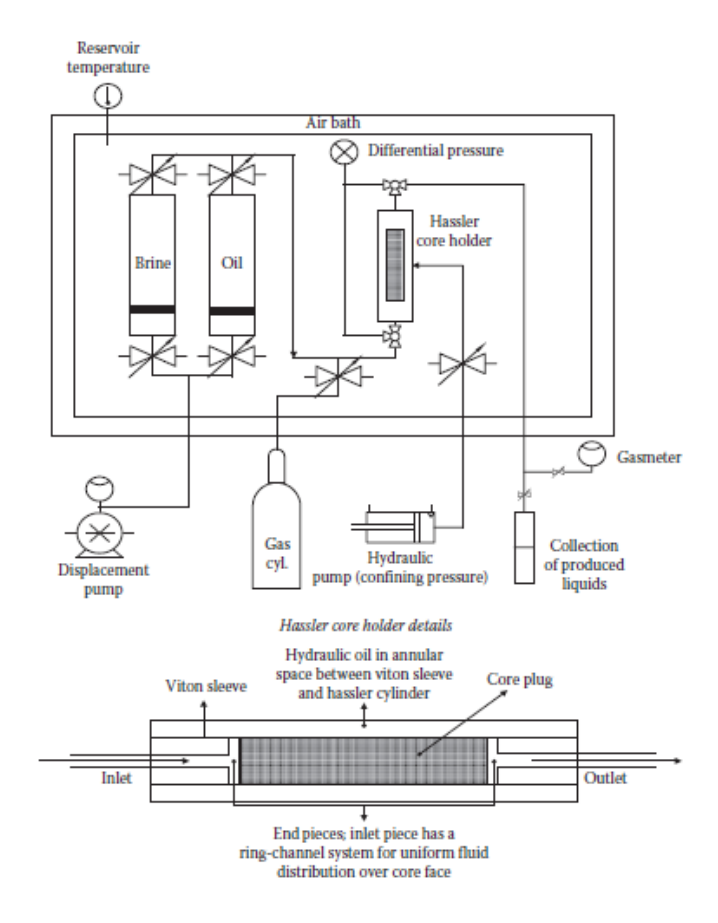


Figure 2.6: Illustration of displacement apparatus for absolute permeability measurement[21]

Another problem associated with using gases is observing absolute permeability higher than the actual liquid-equivalent value. This is known as *klinkenberg effect*, or gas slippage, that occurs when gas molecules have a mean free path comparable to pore size, allowing them to slip at the walls instead of obeying the no-slip boundary condition. To correct for this, a set of permeability measurements is taken at different mean pore pressures. The apparent permeability is plotted against the reciprocal of mean pressure, and the data is extrapolated to infinite mean pressure to obtain the true permeability as illustrated in the following figure [21]:

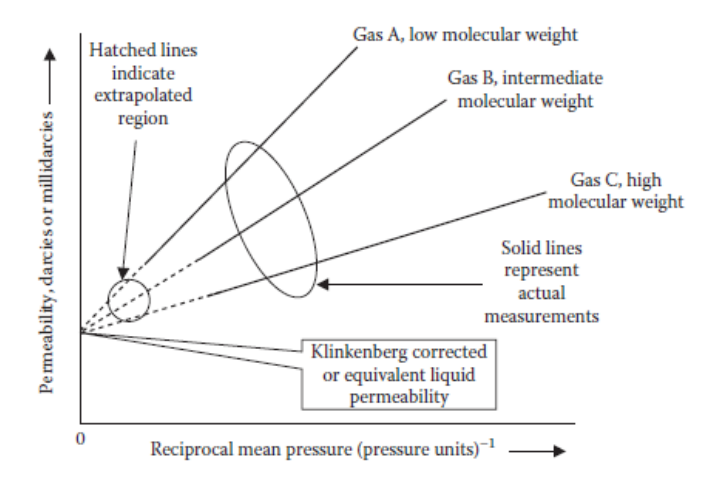


Figure 2.7: Linear extrapolation of apparent gas permeability vs reciprocal mean pressure [21]

#### 2.4 Surface and Interfacial Tension

It is essential to be familiar with cohesive and adhesive forces before defining surface and interfacial tension. Cohesion is the result of attraction between similar molecules, caused by intermolecular forces. In other words, it is the tendency of identical molecules to bond together. A common example of cohesion, is the spherical shape of water droplet, which has strong hydrogen bond, resulting in strong cohesive forces and surface tension. On the other hand, adhesion, is the attraction between molecules of different substances, the tendency of these molecules to stick to each other. Adhesion can occur between liquid–liquid, liquid–solid, or solid–solid interfaces, and may arise from molecular interactions, electrostatic attraction, or mechanical interlocking [23].

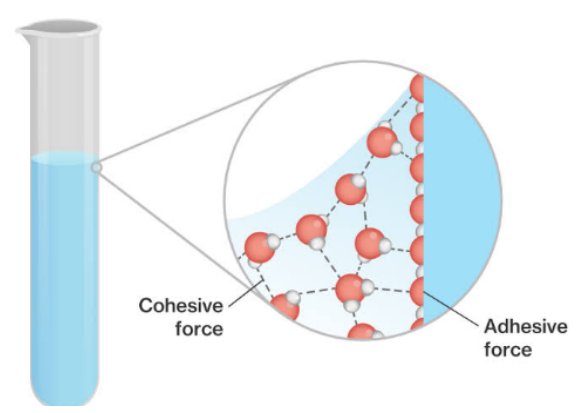


Figure 2.8: Illustration of cohesive and adhesive forces [24]

Since petroleum reservoirs are usually saturated with at least two immiscible fluids, separated by a well-defined interface, the effect of the forces acting at the interface must be considered. Surface tension refers to liquid-gas surface forces and interfacial tension for liquid-liquid interfacial forces. Molecules far from the interface are attracted equally in all directions leading to a net zero attractive force, while molecules at the interface experience a net attractive force towards the bulk of the liquid as illustrated in figures 2.9 and 2.10. This unbalanced attraction on the surface molecules creates a surface that

behave like a stretched membrane with a measurable tension called surface or interfacial tension. It is denoted by the Greek symbol sigma  $(\sigma)$  with unit of force per unit length (N/m)[20][21][25].

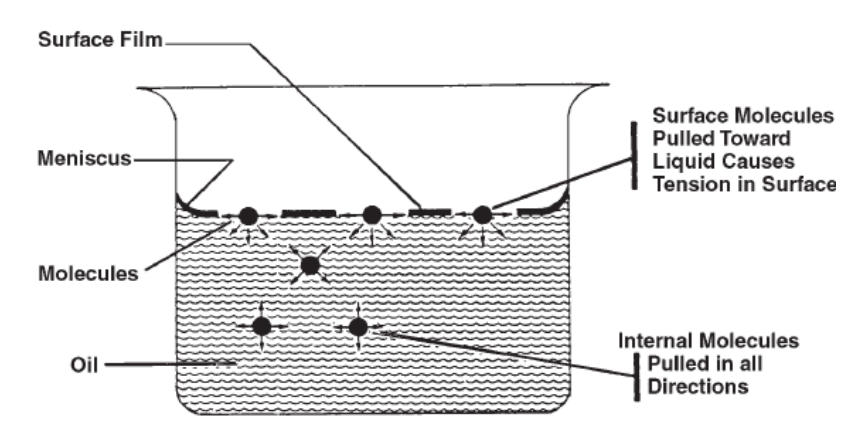


Figure 2.9: The concept of surface tension between two immiscible fluids[20]

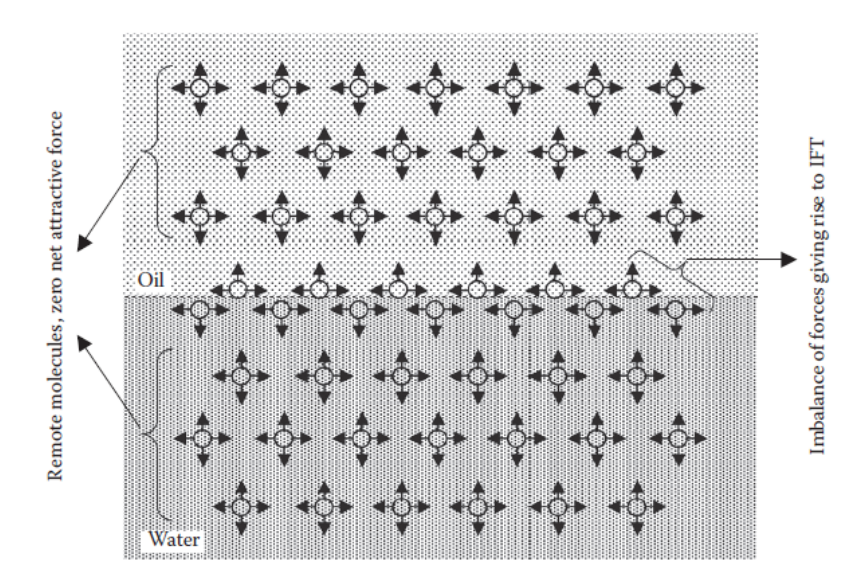


Figure 2.10: The concept of interfacial tension between two immiscible liquids[21]

#### 2.5 Wettability

When two immiscible fluids are present, one tends to spread on the solid surface over the other depending on wettability. If adhesive forces between the solid surface and the fluid dominates over cohesive forces within the fluid, that fluid exhibits a stronger tendency to spread and becoming the wetting phase. Measuring the contact angle between the liquid and solid surface gives an indication of the wettability, a lower contact angle indicates stronger wetting characteristics, whereas a higher contact angle reflects weaker wetting. This property is of particular importance in porous media, as it governs the distribution of fluids within the pore space, where the wetting phase preferentially occupies smaller pores

while the non-wetting phase resides in larger pores [20]. Figure 2.11 gives an example of the wettability of different fluids on a glass plate, water shows the highest tendency to spread with the lowest contact angle, while mercury shows the lowest tendency with the highest contact angle.

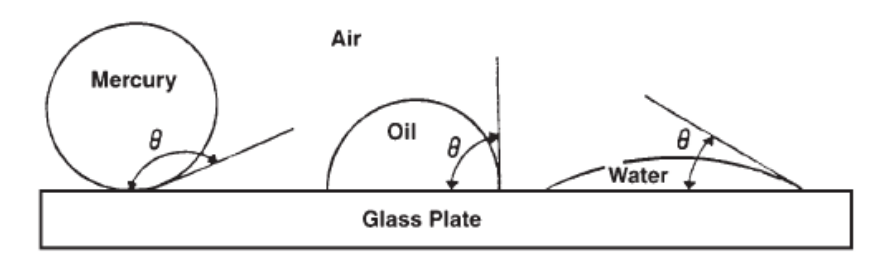


Figure 2.11: Contact angle and Wettability [20]

#### 2.6 Capillary Pressure

When two immiscible fluids come into contact in a porous medium, the wetting phase adheres to the pore walls while the non-wetting phase occupies the pore centers. This arrangement creates a curved interface (meniscus). Mechanical balance of surface or interfacial tension forces at this curved interface requires a pressure difference across it, such that the non-wetting phase pressure is higher than that of wetting phase. This pressure difference is defined as the *capillary pressure*.

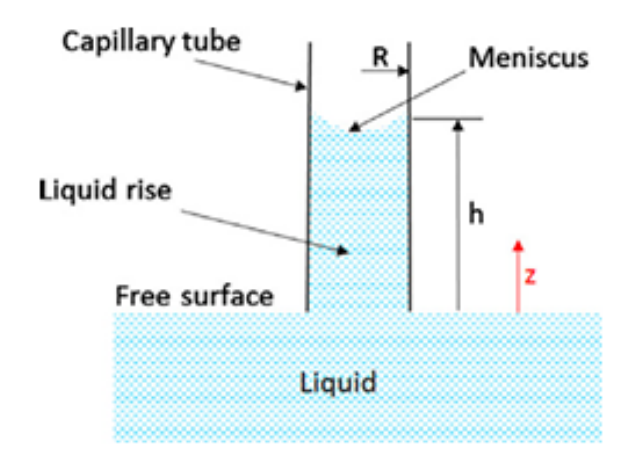


Figure 2.12: Illustration of the meniscus between wetting and non-wetting phase [26]

Capillary pressure is the result of combined effect of interfacial or surface tension, wettability, and pore radius [21]. This pressure difference and capillary rise can be quantified using the following equations:

$$P_c = \frac{2\sigma_{\text{nw-w}}cos\theta}{r} \tag{2.8}$$

$$h = \frac{P_c}{g(\rho_w - \rho_w)} \tag{2.9}$$

```
where P_c: capillary pressure (N/m^2) \sigma_{\text{nw-w}}: non wetting-wetting interfacial tension (N/m) \theta: contact angle (-) r: pore radius (m) h: height of capillary rise (m) g: acceleration due to gravity (m/s^2) \rho_w: density of wetting phase (kg/m^3) \rho_{\text{nw}}: density of non-wetting phase (kg/m^3)
```

In natural reservoir rocks, the pore space is not a single tube but rather a network of interconnected pores with a wide range of pore-throat sizes. For this reason, capillary pressure becomes a function of water saturation. At the free-water level, the water saturation is close to 1 and the capillary pressure is nearly zero. Moving upward into the transition zone, the capillary pressure increases with height, progressively displacing water from larger to smaller pores, so water saturation decreases. Approaching the top of the transition zone, water saturation asymptotically reaches the irreducible value [20]. Figure below give an illustration of how capillary pressure is function of saturation:

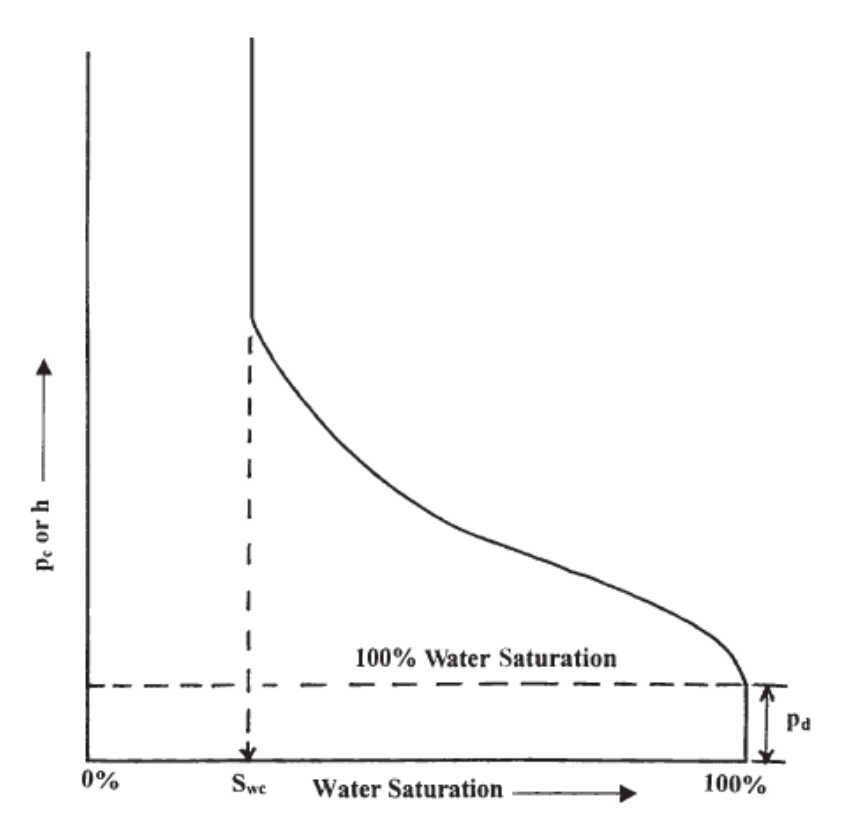


Figure 2.13: Capillary pressure curve [20]

#### 2.7 Relative Permeability

Absolute permeability previously defined refers to a porous medium that is fully saturated with one fluid and is function of rock properties, but reservoirs are usually saturated with

more than one fluid. Darcy's law is extended to include the simultaneous fluid flow of two or more fluid phases present in the porous medium. The effective permeability which is a saturation based function is introduced. It is the apparent ability of the porous medium to transmit one fluid in the presence of other immiscible fluids [27] [21].

To normalize the effect of rock properties and allow comparison between different phases and samples, the concept of relative permeability is introduced. The relative permeability of a phase, is defined as the ratio of effective permeability of that phase to the absolute permeability of the rock. The relation between relative permeability curves is illustrated in the following figure:

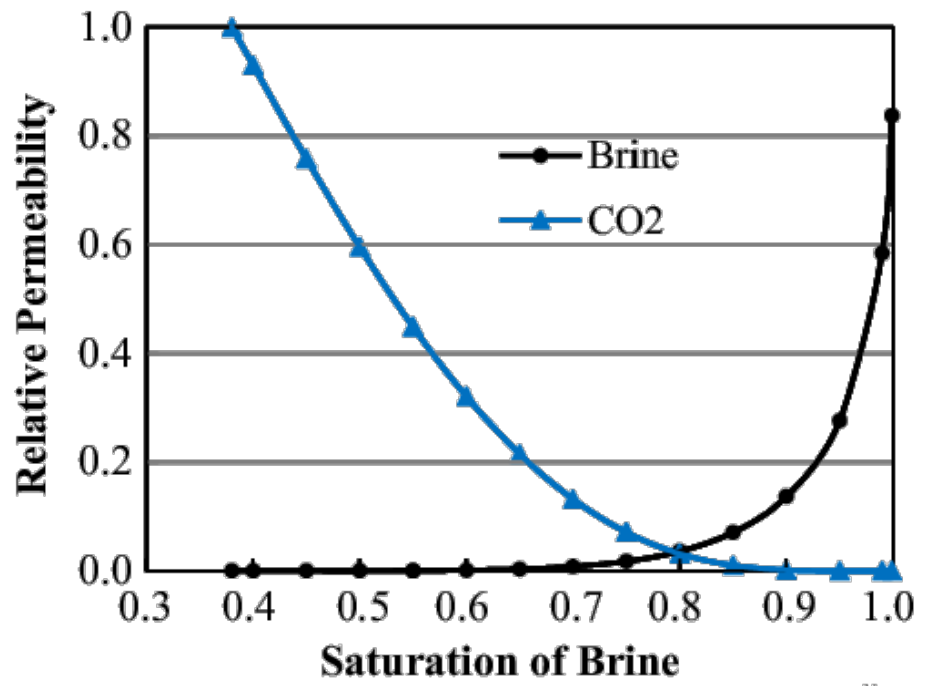


Figure 2.14: Relative Permeability Curves [28]

## Chapter 3

# Apparatus Used and Procedure Followed for Measurement of $scCO_2$ -Brine Relative Permeability in the Laboratory

#### 3.1 Apparatus Used

The RPS-700 apparatus is designed to measure relative permeability in core samples under simulated reservoir conditions using both steady-state and unsteady-state methods. The system includes precision pumps, a core holder, heating units, and advanced instrumentation that enable the simultaneous or sequential injection of multiple fluids under controlled pressure and temperature conditions. The apparatus operates up to 690 bar and 150  $^{\circ}$ C, allowing for accurate determination of relative permeability curves and reliable prediction of reservoir performance [29].

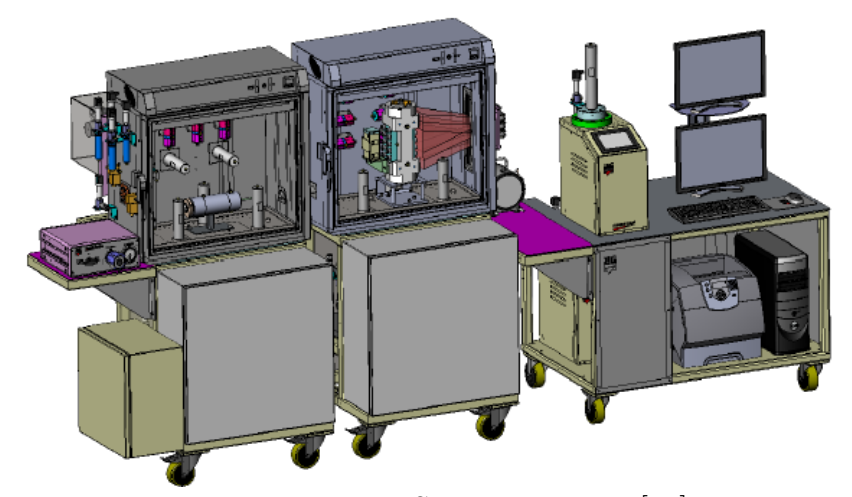


Figure 3.1: RPS700 Main Unit [29]

#### 3.2 Equipments

The RPS-700 apparatus consists of several pieces of equipment, each performing a distinct function within the experimental procedure to ensure the complete execution of the test under the required conditions. The main are the following:

- Liquid Injection Pump: It is a three-piston syringe pump, that provides continuous and constant flow of brine either directly to the core or indirectly into to the accumulator.
- Gas Injection Pump: It is an automatic pump made of two piston for continuous and constant gas injection. It injects  $CO_2$  directly to the core or indirectly to the accumulator from a  $CO_2$  bottle.
- Hydrostatic Core Holder: It houses the core sample installed in an AFLAS sleeve and applies the confining pressure required to simulate the reservoir overburden stress. The confining pressure is generated by injecting silicon oil or clean water into the annular space between the sleeve and the core holder, ensuring radial sealing and preventing side leakage. It also enables controlled fluid injection through the core while allowing pressure measurements via pressure taps.
- Automatic Confining Pump: It is the pump responsible on generating the confining pressure in the core holder by pumping silicon oil or clean water to the annular space between the core holder and the sleeve holding the core sample.
- Automatic Back Pressure System: It is filled with nitrogen and connected to the top of the back pressure regulator in order to control pressure and maintain downstream condition to avoid gas expansion.
- HP/HT Fluid Separator: The role of the separator is to separate the fluids produced from the core at reservoir conditions. It includes a separation bore that separates fluids under gravity, and any change in the interface between the brine and  $CO_2$  corresponds to a change in saturation in the core that can be calculated according to balance equations.
- Ovens: The role of the ovens is to serve the reservoir temperature in order to conduct it at reservoir-like conditions. They apply heat using a forced air fan and heater.

## 3.3 Pre-experiment Preparation for $CO_2$ -Brine Systems

Before performing the experiments, several preparation steps should be done to ensure the system properly conditioned and to obtain accurate and reliable data. This is particularly important when dealing with  $scCO_2$ -brine systems, where some additional procedures should be performed due to the unique characteristics of  $scCO_2$  such as high compressibility.

First the core sample is prepared by choosing a precision right cylinders with parallel end faces, and it is saturated with brine outside RPS700 prior to loading. Then the excess liquid is wiped from the surface without removing fluid from pores, and the weight of the sample is measured and recorded along with its dimensions.

After that, the equipment of the apparatus is prepared by performing some cleaning, and by replacing some accessories taking into consideration the flowing of  $scCO_2$  during the test. For the core holder and HP/HT separator, the AFLAS or CHEMRAZ O-rings is used instead of Viton to avoid sealing destruction in  $CO_2$  applications. Also replace O-rings that are worn, torn, brittle or subjected to to elevated temperature higher than 150 °C for more than 24 hours. For the core holder, all its components must be cleaned by solvents and distilled water, and AFLAS sleeve is used instead of Viton. While for the HP/HT separator, the sapphire window that allow monitoring the interface between the two fluids, must be cleaned with water and solvents then blow air through it to remove any residual fluids, and never remove it unless leak is observed.

Each pump must be filled with the required fluid for the experiment. The automatic confining pump is filled with silicon oil, clean water, or low viscosity oil that can resist high temperature without smoke or explosion in case of leakage to load the confining chamber of the core holder. The back pressure pump is loaded with nitrogen and connected to the top of the back pressure regulator to control pore pressure. For the fluid flow, the liquid injection pump cylinders is filled with brine and the gas injection pump is filled with  $CO_2$  from the  $CO_2$  bottle, to pump them through the core.

#### 3.4 Procedure

After completing all preliminary steps, the system is ready to perform the steady-state and unsteady-state experiments. Each experiment follows a distinct procedure, as they employ different methodologies for determining relative permeabilities. The procedure for each method is described below.

#### 3.4.1 Steady State

- 1. Insert the 100% brine saturated core into the AFLAS sleeve, and load them into the core holder
- 2. After making sure that the core sample is properly installed, and all connections to the core holder are tight, run the automatic confining pump to pressurize the core to 70 bar
- 3. Fill the HP/HT separator with equal amounts of both phases
- 4. Make sure triple pumps are prepared for recirculating mode
- 5. Pressurize the pore circuit to 35 bar and inspect the entire system for leaks (confining pressure must be maintained 35 bar above the pore pressure)
- 6. Close the oven doors, turn it on and set it at the desired temperature
  - 6.a. Continuously monitor confining and pore pressure during heating as pressure will increase due to thermal expansion (Never allow confining pressure to drop below pore pressure + 35 bar)
  - 6.b. Pumps ovens are turned on automatically to the desired temperature

- 6.c. After the core holder temperature stabilizes within 2°C of the target, wait for an hour for complete thermal equilibrium
- 7. Check the consistency of absolute permeability by injecting brine at constant flow rates through the core
  - 7.a. Recommended flow rates is between 1 and 5 ml/min, selected based on the core's air permeability
  - 7.b. Ensure the differential pressure measured across the core doesn't exceed the upper limit of the high pressure differential transducers
  - 7.c. Be sure to flow enough brine through the core sample (10 to 20 PV) to determine the brine permeability
- 8. Increase the system pressure to the desired experimental conditions. Remember to keep the confining at 35 bar higher than the pore pressure. (Note: for scCO2-brine experiments the conditions should be higher than the critical point (31°C and 73.8 bar))
- 9. Store the fluids in the accumulators before injection
- 10. Displace the brine by injecting  $CO_2$  only until the irreducible water saturation is reached (marked by stabilizing of CO2-brine interface in the separator)
- 11. Calculate the irreducible water saturation using the following equation:

$$S_{\text{wi}} = \frac{V_{\text{brine,initial}} - V_{\text{brine,produced}}}{V_{\text{pore}}}$$
(3.1)

where

 $V_{\text{brine,initial}}$ = Brine volume initially saturating the core  $V_{\text{brine,produced}}$ = Brine volume produced measured by the video tracker

 $V_{\text{pore}}$ = Pore volume of the core

- 12. Measure the  $CO_2$  effective permeability at  $S_{wi}$  using Darcy's law
- 13. Start injecting  $CO_2$  and brine simultaneously at increasing water fractional flow for 5-10 stages to determine the imbibition relative permeability curve (keep  $\Delta P < 40$ -50 psi, if exceeded reduce flow rate), SS condition for each step is achieved by stable pressure drop and interface in the separator, relative permeability is calculated through Darcy's law and saturation from the fluids levels in the separator

#### 3.4.2 Unsteady State

- 1. The first 12 steps of steady state method are similar to the unsteady state procedure.
- 2. After reaching irreducible water saturation, a high constant flow rate of brine is pumped into the core sample, to displace the non-wetting phase and obtain the imbibition relative permeability curve
- 3. Pressure drop, effluent volumes, and saturation are monitored continuously after breakthrough to determine relative permeabilities using JBN method

- 3.a. Pressure drop is measured using pressure sensors at the inlet and outlet of the core
- 3.b. Effluent volumes are calculated from the interface in the HP/HT separator
- 3.c. Also saturation is calculated from this interface

## Chapter 4

## Relative Permeability Measurement

Two experimental methods—the steady-state (SS) approach and the unsteady-state (USS) method—are frequently used to establish relative permeability functions. Until a stable equilibrium is achieved, both phases are co-injected using the SS method at regulated fractional flow rates. Under these circumstances, the measured flow rates and pressure gradients can be used to directly calculate relative permeabilities. The technique is timeconsuming and experimentally challenging, despite being thought to be accurate and less impacted by capillary end effects which refer to the accumulation of the wetting phase near the outlet of the core, resulting in a non-uniform saturation profile and influencing the overall pressure drop to compensate for the discontinuity in capillary pressure at the outlet boundary. The USS approach, on the other hand, involves injecting one phase to displace the other while monitoring pressure response and effluent output at a consistent rate. Estimating the relative permeability curves is made possible by the interpretation of these transient data, which is frequently based on the Johnson–Bossler–Naumann (JBN) technique and Buckley-Leverett theory. Although this approach is quicker and easier to use, it is more susceptible to experimental errors and necessitates indirect interpretation, which is occasionally bolstered by historical matching. Although the application considered in this work focuses on  $CO_2$ -brine systems, the underlying methodology remains the same, with additional considerations related to fluid properties, compressibility, and experimental constraints that will be discussed.

#### 4.1 Steady-State Technique

This technique involves the simultaneous injection of two immiscible fluids into a core sample at a constant total flow rate or pressure drop to achieve equilibrium [30]. Once steady-state condition is achieved, indicated by constant outlet flow rates and a stabilized pressure drop across the core [21], pressure drop, flow rate, and saturation values are measured for relative permeability determination. This process is repeated in steps for different fractional flow ratios ( $f_w = \frac{qw}{qt}$ ) generating a series of data points that allow the construction of complete relative permeability curves. Hysteresis is avoided by controlled unidirectional saturation changes[30].

Relative permeability is determined by direct application of Darcy's law for multiphase

flow, according to the following equations:

$$K_{\rm rw}(Sw) = \frac{\mu_w L Q_w}{K A \triangle P_w} \tag{4.1}$$

$$K_{\rm rnw}(Sw) = \frac{\mu_{\rm nw} L Q_{\rm nw}}{K A \triangle P_{\rm nw}}$$
(4.2)

where

 $K_{\text{rw}}(Sw), K_{\text{rnw}}(Sw)$ : relative permeability of the wetting and non-wetting phase respectively (-)

 $\mu_w$ ,  $\mu_{\rm nw}$ : viscosity of the wetting and non wetting phase respectively (Pa.s)

 $Q_w, Q_{\text{nw}}$ : flow rate of wetting and non-wetting phase respectively  $(m^3/s)$ 

L: length of the core (m)

K: absolute permeability  $(m^2)$ 

A: cross sectional area of the core  $(m^2)$ 

 $\triangle P_w$ ,  $\triangle P_{\text{nw}}$ : pressure drop of wetting and non-wetting phase respectively (Pa)

During steady-state conditions, a uniform saturation distribution is usually assumed along the core, even when an adverse mobility ratio is involved, which gives it an advantage over the unsteady state[16]. This assumption arises because steady state requires the overall pressure drop to remain constant over time, which can only be achieved if the capillary pressure is constant throughout the core [31]. If capillary pressure varies spatially, the fluids will continue to redistribute: the non-wetting phase will invade regions of lower capillary pressure while the wetting phase is displaced, leading to fluctuations in both the measured pressure drop and the effluent fractional flow over time. By contrast, when capillary pressure is uniform, no further redistribution occurs, saturation remains stable, and the pressure drop measured across the core is the same for both the wetting and non-wetting phases:

$$\triangle P_C = \triangle P_{\text{nw}} - \triangle Pw$$
, where  $\triangle P_c = 0$  (4.3)

then

$$\Delta P_{\rm nw} = \Delta P_{\rm w} \tag{4.4}$$

This technique is considered the most accurate method for relative permeability determination, as the co-injection of fluids at a constant ratio for long time confines the capillary end effect to a thin zone at the core outlet, making the measured pressure drop primarily governed by viscous forces [16]. Furthermore, it allows the determination of relative permeabilities over a wider range of saturations compared to unsteady-state methods where the displacement propagates with a front leading to a high saturation immediately at the outlet. However, the main drawbacks are the long equilibration times—each step may require several hours to days—and the difficulty of saturation determination when relying only on mass balance. In this case, repeated loading and unloading of the core can cause fluid loss or sample alteration, which reduces the accuracy of saturation and, consequently, the relative permeability measurements [30][21].

The interpretation of the monophasic injection at fw=0 and fw=1 must be held with caution, as the capillary end effect is higher leading to an overestimation or underestimation of the relative permeabilities and the irreducible water saturations, which is a key parameter

when considering  $CO_2$  injection, is hard to reach during non-wetting monophasic injection  $(f_w = 0)$  due to the increased capillary end effect, the lowest obtained saturation is the residual water saturation and the gap with irreducible water saturation can be reduced by accessing to local saturation using in-situ imaging techniques, but this doesn't eliminate the need for history matching techniques for correction [16].

The core principle of the steady-state (SS) method for relative permeability measurement is the application of Darcy's law, which assumes that incompressible fluids flow through the porous medium. For supercritical  $CO_2$ -brine systems, this assumption no longer holds, as supercritical  $CO_2$  is a compressible fluid whose density and viscosity vary substantially with changes in pressure and temperature as shown in the following figures:

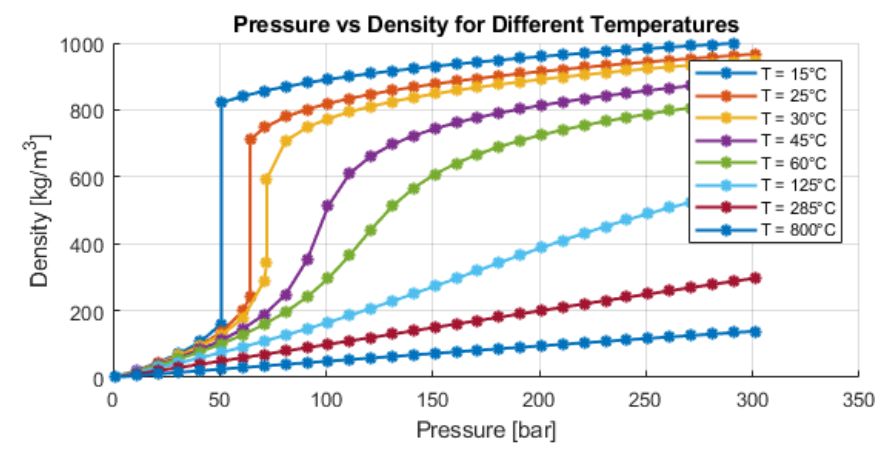


Figure 4.1:  $CO_2$  density variation with pressure and temperature [32]

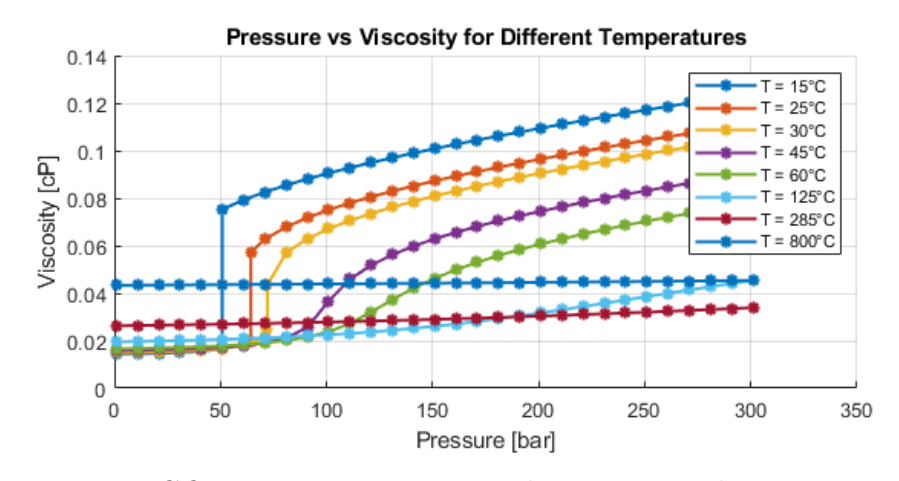


Figure 4.2:  $CO_2$  viscosity variation with pressure and temperature [32]

 $CO_2$  is usually stored in supercritical phase which refer to conditions higher than the critical point (31°C and 73.8 bar), where it can be noticed that a variation of pressure in the near supercritical zone leads to a noticeable variation in density and viscosity.

Although  $scCO_2$  is compressible, but Darcy's law can be still applied as long as the pressure drop along the sample is sufficiently small. When the ratio of pressure drop

over the average pressure of the experiment is less than 10% the variation of density and viscosity can be considered negligible and use the average properties for calculation.

$$P_{\text{avg}} = \frac{P_{\text{in}} + P_{\text{out}}}{2} \tag{4.5}$$

And since volumetric flow rate changes with density variation, it is replaced by mass flow rate  $(\dot{m})$  that is conservative.

$$\dot{m} = \rho q \tag{4.6}$$

The mass flow rate is calculated for the inlet volumetric flow rate and density, and is replaced in Darcy's equation to have it in terms of mass flow rate. The Darcy's equation become:

$$\dot{m} = \frac{k \, k_r \, A \, \rho_{\text{avg}}}{\mu_{\text{avg}}} \cdot \frac{\Delta P}{L} \tag{4.7}$$

When dealing with high pressure drops (low permeability cores for example), variation in fluid properties can no longer be neglected and a correction factor for relative permeability calculation must be applied. In 2013, Ramakrishnan and Chugunov [33]introduced a correction factor to account for fluid compressibility. It shows that for  $scCO_2$  the correction is small (around 4%) confirming that the traditional Darcy's law can be used safely under small pressure drop and high pressure conditions [33]. The correction equation is as follows:

$$k_r = k_r^{(0)} \cdot (1 + C_M) \tag{4.8}$$

where

 $k_r$ : is the corrected relative permeability

 $k_r^{(0)}$ : is the obtained (without correction) relative permeability

 $C_M$ : correction factor

#### 4.2 Unsteady State Technique

Unlike the steady-state technique, the unsteady-state method relies on an immiscible displacement process. In this approach, the core sample—either in its native state or restored after cleaning and aging—is flooded with a displacing fluid at a constant flow rate. The injection continues until the displacing phase fully replaces the displaced phase, while effluent volumes and the global pressure drop are continuously monitored as functions of time. The relative permeabilities are then derived using the Johnson-Bossler-Naumann (JBN) method, which applies Buckley-Leverett displacement theory together with Welge's approach for estimating average saturations. These methods assume linear, incompressible flow, and negligible capillary forces [21].

A history-matching procedure is often employed to recover the missing data at the edges of the relative permeability curves, where capillary end effects can distort experimental measurements. In some cases, however, the entire set of relative permeability curves is determined through history matching. This method is preferred over steady state since it can be done in few hours and with less fluid quantity [16].

The main drawbacks of this method are the capillary end effects, viscous fingering, and channeling, which are difficult to monitor and account for properly, and the uncertainties due to simplifying assumptions [30].

In the following sections, a detailed description of how to use the USS data to determine relative permeabilities:

#### 4.2.1 Fractional Flow Equation

This equation relates the experimental data obtained to the ratio of relative permeabilities. Fluids flowing across the core are assumed incompressible and according to the continuity equation for each phase:

$$\frac{\partial q_{\text{nw}}}{\partial x} = -\phi A \frac{\partial S_{\text{nw}}}{\partial t} \tag{4.9}$$

$$\frac{\partial q_w}{\partial x} = -\phi A \frac{\partial S_w}{\partial t} \tag{4.10}$$

Additionally,

$$\frac{\partial S_{\text{nw}}}{\partial t} + \frac{\partial S_w}{\partial t} = 0 \tag{4.11}$$

since

$$S_{\text{nw}} + S_w = 1$$
, everywhere (4.12)

So.

$$\frac{\partial}{\partial x}(q_{\text{nw}} + q_w) = 0 \tag{4.13}$$

which means that total flow rate is constant across the core and fractional flow variation is not due to changes in total flow rate.

Darcy's law for multi phases is:

$$q_{\rm nw} = -\frac{k_{\rm nw}A}{\mu_{\rm nw}} \left(\frac{\partial P_{\rm nw}}{\partial x}\right) \tag{4.14}$$

$$q_w = -\frac{k_w A}{\mu_w} \left(\frac{\partial P_w}{\partial x}\right) \tag{4.15}$$

and the capillary pressure in the system is

$$P_c = P_{\text{nw}} - P_w \tag{4.16}$$

Substituting (4.15) and (4.16) in (4.14), to obtain

$$q_{\rm nw} = \frac{k_{\rm nw}A}{\mu_{\rm nw}} \left[ \frac{q_w \mu_w}{k_w A} \right] \tag{4.17}$$

where capillary pressure gradient is neglected due to the assumption of dominating viscous forces at high rates of the experiment [21]

Fractional flow equation is:

$$f_w = \frac{q_w}{q_{\text{nw}} + q_w} \tag{4.18}$$

By substituting equation (4.17) in (4.18) we obtain:

$$fw = \frac{1}{1 + [k_{\rm rnw}\mu_w/k_{\rm rw}\mu_{\rm nw}]}$$
 (4.19)

For the full range of saturations, corresponding relative permeabilities yield a fractional flow curve with the typical S-shape, with a saturation limit between  $S_{\text{wi}}$  and  $1 - S_{\text{nwr}}$  [21]:

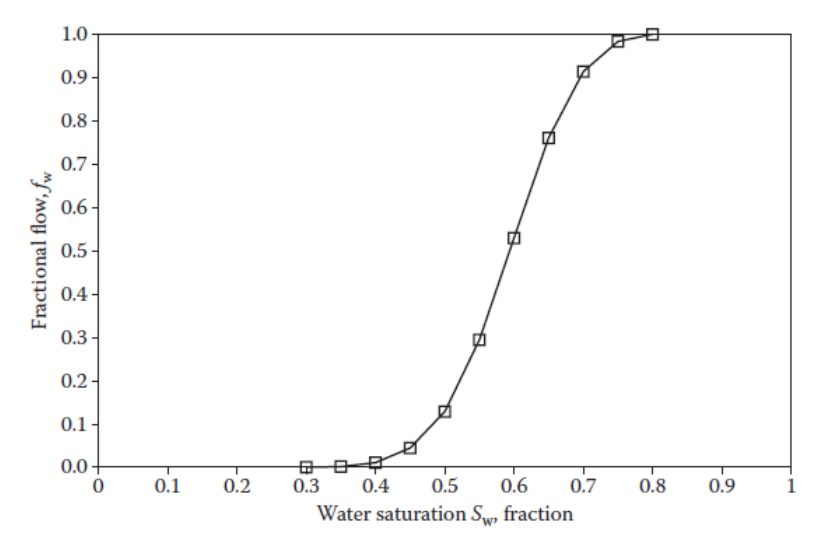


Figure 4.3: A typical fractional flow curve for a range of relative permeabilities [21]

#### 4.2.2 Buckley-Leverett Theory

The basic equation describing two-phase immiscible displacement in one dimension was demonstrated by Buckley and Leverett in 1942. The equation describes the propagation velocity of a plane of constant water saturation traveling through a linear system [21]. This model was based on the following assumptions:

- Immiscible flow for the two incompressible fluids is one-dimensional (By keeping the pressure drop across the core small, the viscosity and density variation is small and the assumption is valid).
- No mass transfer between fluids (Equilibrating the fluids before injection is an essential step in  $scCo_2$  experiments to avoid mass transfer as discussed later).
- Flow is horizontal
- The effects of capillary and gravity forces are neglected due to displacement at high injection rates
- Constant viscosity
- Homogeneous porous media
- Constant injection rate

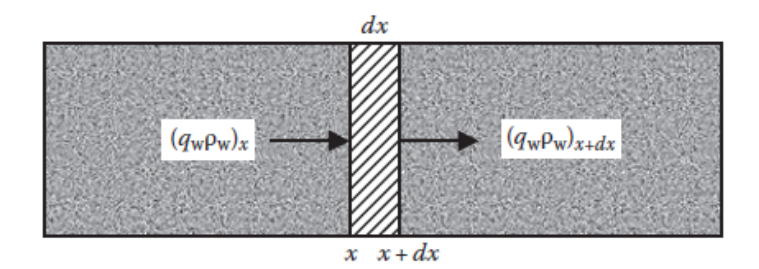


Figure 4.4: Schematic of the homogeneous porous media and the volume element  $A\phi dx$  that is considered for the application of conservation of mass equation for development of Buckley-Leverett theory [21]

It begins by applying conservation of mass of water flowing through a homogeneous porous media:

$$(q_w \rho_w)_x - (q_w \rho_w)_{x+dx} = A\phi dx \frac{\partial}{\partial t} (\rho_w S_w)$$
(4.20)

After algebraic manipulation, this leads to:

$$V_{\rm Sw} = \left(\frac{dx}{dt}\right)_{\rm Sw} = \frac{1}{A\phi} \left(\frac{\partial q_w}{\partial S_w}\right)_t \tag{4.21}$$

Since  $q_w = f_w q_t$  from fractional flow equation, and  $q_t$  is constant as previously proven, then:

$$V_{\rm Sw} = \left(\frac{dx}{dt}\right)_{S_w} = \frac{q_t}{A\phi} \left[ \left(\frac{df_w}{dS_w}\right)_t \right]_{S_w} \tag{4.22}$$

This is the Buckley-Leverett equation, which shows that for a constant total flow rate  $q_t$ , the velocity of a plane of constant water saturation  $(V_{\text{Sw}})$  is directly proportional to the derivative of the fractional flow at that saturation [21]. This demonstrates that intermediate saturation fronts propagate more rapidly than low or high saturations. The reason is that the fractional flow curve has its steepest slope at intermediate saturations, while it flattens near residual and irreducible saturations (Figure 4.3). A typical plot of  $df_w/dS_w$  versus water saturation is illustrated in the following figure:

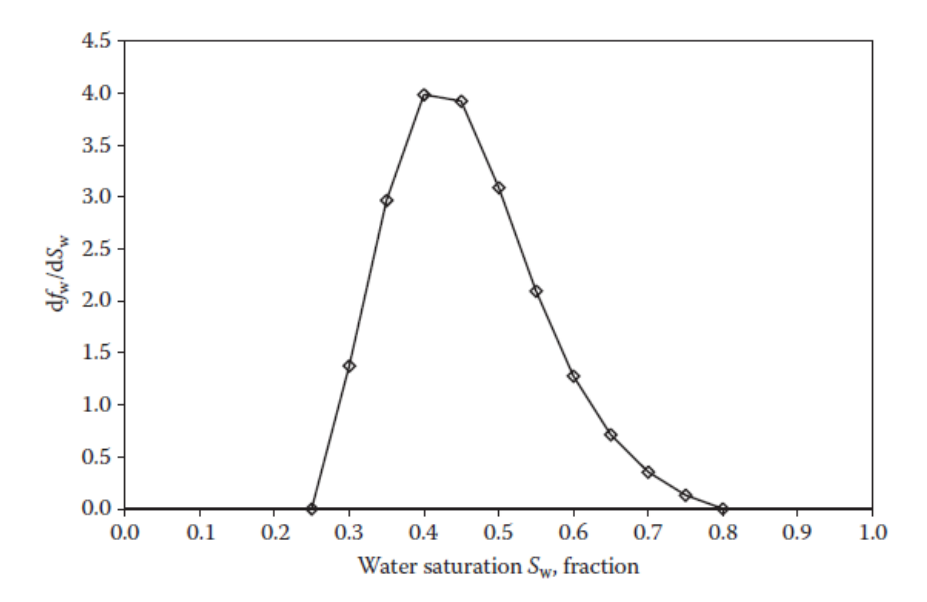


Figure 4.5:  $df_w/dS_w$  versus water saturation plot[21]

Integrating the equation:

$$\int_0^{x_{S_w}} dx = \left(\frac{df_w}{dS_w}\right)_{S_w} \frac{1}{A\phi} \int_0^t q_t dt \tag{4.23}$$

We obtain:

$$X_{S_w} = \frac{W_i}{A\phi} \left(\frac{df_w}{dS_w}\right)_{S_w} \tag{4.24}$$

where  $X_{Sw}$  is the position of a specific saturation, and  $W_i = q_t t$ . From this equation we can plot the position of different saturation planes at a given time by determining the slope of fractional flow versus saturation.

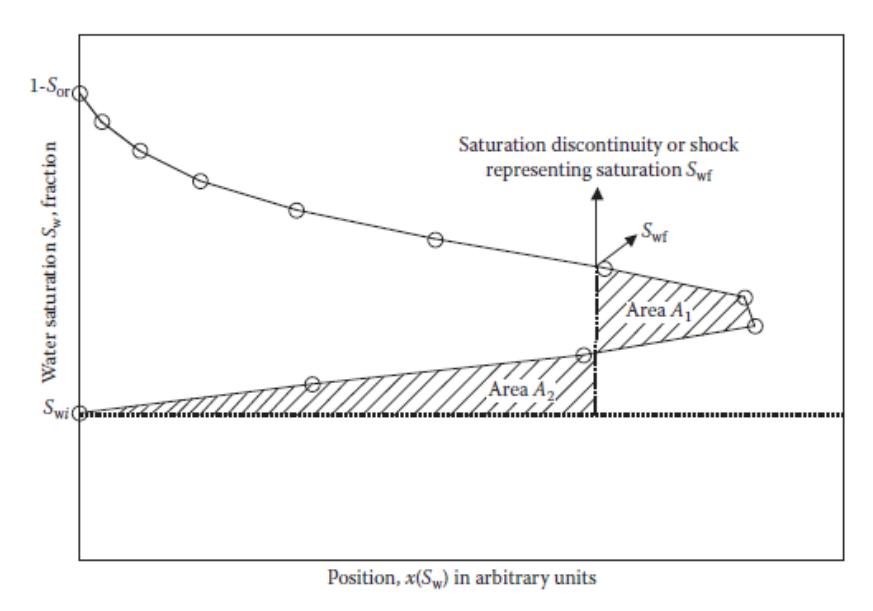


Figure 4.6: Buckley-Leverett solution to the physically impossible situation [21]

Figure 4.6 represents the position of each saturation  $X_{\rm Sw}$  as function of its saturation, where an impossible physical situation occurs where each position have two saturations, in other words different saturation planes overtaking each other, which is physically inconsistent. A saturation discontinuity is defined as a solution for this problem, and this is positioned based on the equality between areas  $A_1$  and  $A_2$  [21]. Saturation in-front the discontinuity is  $S_{\rm wi}$  and behind it is the average saturation  $\bar{S}_w$  in the invaded zone. Dividing (Eq 4.24) by the total length of the porous medium or core sample, the following equation will be obtained:

$$\frac{X_{S_w}}{L} = Q_{wi} \left(\frac{df_w}{dS_w}\right)_{S_w} \tag{4.25}$$

where  $X_{\text{Sw}}/L$  is the normalized positioning of water saturation, and  $Q_{\text{wi}} = W_i/LA\phi$  is the pore volume of water injected. From this equation the saturation profiles for arbitrary amounts of pore volume  $Q_{\text{wi}}$  can be obtained as illustrated in the following figure [21]:

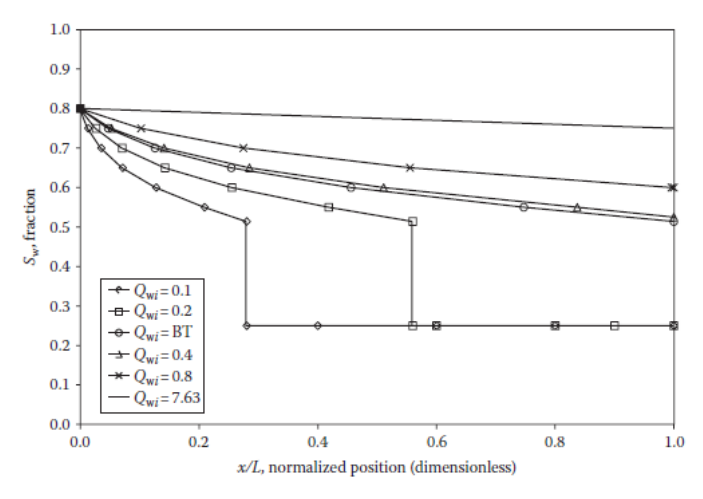


Figure 4.7: Water saturation profiles for various  $Q_{\rm wi}$  [21]

## 4.2.3 Welge's Extension Solution

In 1952, Welge presented a construction to determine the average water saturation behind the front and the relative permeability ratio [21]. Consider the water saturation profile at a fixed time t prior to breakthrough:

Let  $x_1$  denote the distance traveled by the maximum water saturation  $S_w = 1 - S_{\text{or}}$  and let the flood front saturation  $S_{\text{wf}}$  be located at  $x_2$ . A material balance on the invaded region  $[0, x_2]$  gives:

$$W_i = A\phi x_2(\bar{S_w} - S_{wi}) \tag{4.26}$$

where

 $W_i$  is the cumulative water injected at fixed time t  $(m^3)$ 

A is the cross-sectional area  $(m^2)$ 

 $\phi$  is the porosity of the medium (-)

 $x_2$  is the position of the front (m)

 $S_w$  is the average water saturation behind the front (-)

 $S_{wi}$  is the irreducible water saturation (-)

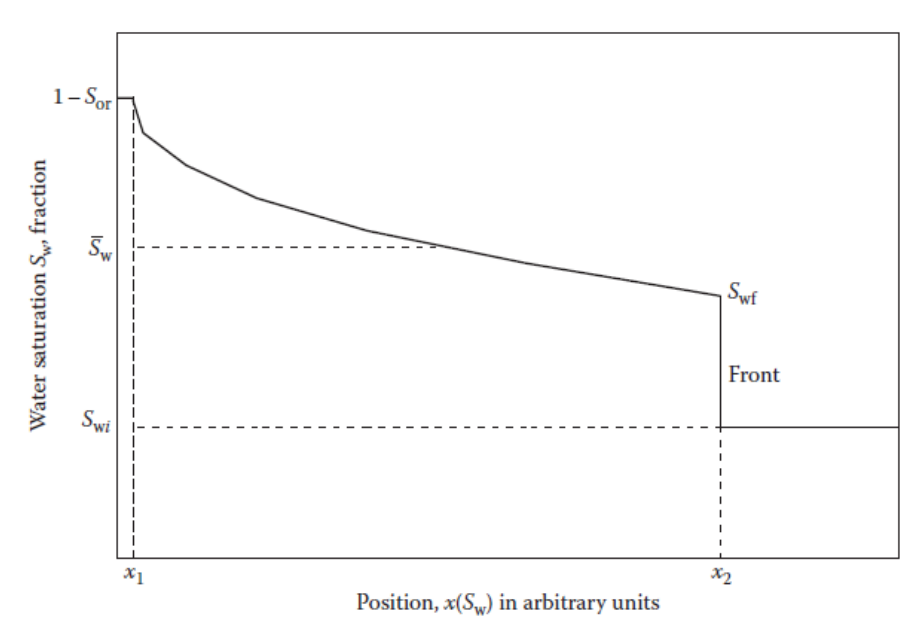


Figure 4.8: Water saturation distribution as function of position at a fixed time t, prior to breakthrough time [21]

By substituting (Eq 4.24) in (Eq 4.26)

$$W_i = A\phi \frac{W_i}{A\phi} \left(\frac{df_w}{dS_w}\right)_{S_{wf}} \left(\bar{S}_w - S_{wi}\right) \tag{4.27}$$

then

$$\bar{S}_w = S_{wi} + \frac{1}{\left(\frac{df_w}{dS_w}\right)_{S_{wf}}} \tag{4.28}$$

The saturation of  $S_{\rm wf}$  is unknown then  $(df_w/dS_w)$  is unknown. The average water saturation in the invaded zone can also be determined by integrating the saturation profile between the inlet and the front[21]:

$$\bar{S}_w = \frac{\int_0^{x_2} S_w \, dx}{\int_0^{x_2} dx} \tag{4.29}$$

After some algebraic manipulations, this leads to:

$$\bar{S}_w - S_{wf} = \frac{1 - f_{wf}}{\left[\frac{df_w}{dS_w}\right]_{S_{wf}}} \tag{4.30}$$

So

$$\left[\frac{df_w}{dS_w}\right]_{S_{wf}} = \frac{1 - f_{wf}}{\bar{S}_w - S_{wf}} = \frac{1}{\bar{S}_w - S_{wi}}$$
(4.31)

Eq 4.31 states that the slope of the fractional-flow curve at the shock saturation  $S_{wf}$  equals the slope of the straight line that (i) joins the shock point  $(S_{wf}, f_{wf})$  to  $(\bar{S}_{w}, 1)$  and

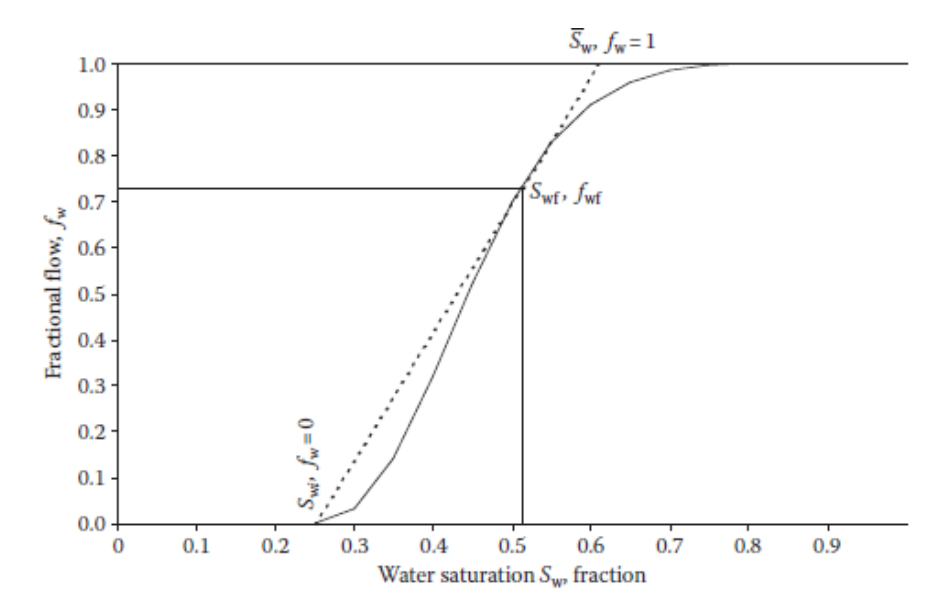


Figure 4.9: Welge's tangent (extension) solution [21]

(ii) joins the initial point  $(S_{wi},0)$  to  $(\bar{S}_w,1)$ . This is satisfied by a single straight line passes through  $(S_{wi},0)$ , tangent to  $f_w(S_w)$  at  $(S_{wf},f_{wf})$ , and intersects  $f_w=1$  at  $(\bar{S}_w,1)$  [21]:

When the front exceeds breakthrough, the saturation at the outlet can be obtained through a tangent line to the fractional flow curve at saturation higher than  $S_{\rm wf}$ , this will correspond to the water saturation  $(S_{\rm wL})$  and fractional flow  $(f_{\rm wL})$  at the outlet (x=L). The average water saturation inside the medium can be obtained by extrapolating the tangent to  $f_w = 1$  [21].

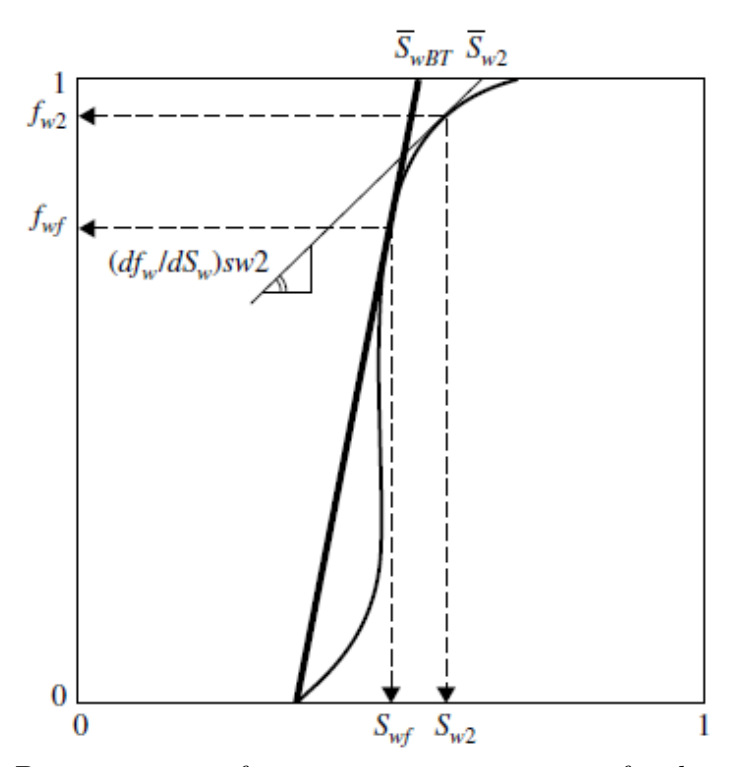


Figure 4.10: Determination of average water saturation after breakthrough [20]

The average water saturation equation according to Eq 4.28 becomes:

$$\bar{S}_w = S_{wL} + \frac{1 - f_{wL}}{\left[\frac{df_w}{dS_w}\right]_{S_{wL}}} \tag{4.32}$$

And according to Eq 4.22 at x=L:

$$Q_{wi} = \frac{1}{\left(\frac{df_w}{dS_w}\right)_{S_{wI}}} \tag{4.33}$$

where  $Q_{\rm wi}$  is the pore volume of water injected, and  $1-f_{\rm wL}=f_{\rm nwL}$  is the fractional flow of non-wetting at the outlet end that can be obtained by differentiation of the cumulative non-wetting phase produced with respect to the water injected  $(f_{\rm nwL}=dQ_{\rm nwp}/dQ_{\rm wi})$  [21], then:

$$S_{wL} = \bar{S}_w - Q_{wi} \frac{dQ_{op}}{dQ_{wi}} \tag{4.34}$$

The average water saturation can be calculated from from the experimental data recorded as:

$$\bar{S}_w = S_{wi} + \frac{\text{cumulative volume of non-wetting phase produced}}{\text{pore volume of the sample}} = S_{wi} + Q_{nwp}$$
 (4.35)

that leads to the determination of the water saturation at the outlet end from Eq 4.34. Also the relative permeability ratio can be determined from Welges method using the following equations:

$$f_{wL} = \frac{1}{1 + \left[\frac{k_{rnwL}\mu_w}{k_{rwL}\mu_n w}\right]} \quad \text{or} \quad f_{oL} = \frac{1}{1 + \left[\frac{k_{rwL}\mu_n w}{k_{rnwL}\mu_w}\right]}$$
 (4.36)

when rearranging:

$$\frac{k_{rwL}}{k_{rnwL}} = \frac{\mu_w}{\mu_n w} \frac{(1 - f_{nwL})}{f_{nwL}} \tag{4.37}$$

## 4.2.4 Johnson-Bossler-Naumann Method

In 1959, Johnson, Bossler, and Naumann developed a method (commonly referred to as the JBN method) to determine the individual relative permeabilities of fluids from unsteady-state core-flooding experiments. The method requires as input the pore volumes of fluids injected, the pressure drop across the sample, and the viscosities of the fluids. Average and outlet water saturations are obtained using Welge's approach. Because the saturation profile during unsteady-state displacement is non-uniform and evolves with time, Darcy's law cannot be applied directly at a single saturation; the measured pressure drop represents the combined effect of multiple saturation regions. To overcome this, Johnson et al. applied Buckley–Leverett theory to relate the movement of the saturation front to the fractional flow observed at the outlet, thereby eliminating the need for direct local saturation measurements inside the core [21].

The development of the method begins by the pressure drop across the sample, obtained by integrating the pressure gradient along the core:

$$\Delta P = -\int_0^L \frac{\partial P}{\partial x} \, dx \tag{4.38}$$

expressing the pressure gradient by Darcy's law for non-wetting phase:

$$\frac{\partial P}{\partial x} = -\frac{\mu_{\text{nw}} u_{\text{nw}}}{k k_{rnw}} \tag{4.39}$$

and using  $u_{\text{nw}} = u f_{\text{nw}}$  (with  $u = q_t/A$  and  $f_{\text{nw}} = q_{\text{nw}}/q_t$ ) gives

$$\frac{\partial P}{\partial x} = -\frac{\mu_{\text{nw}} u f_{\text{nw}}}{k k_{rnw}} \tag{4.40}$$

where

k is the base permeability (absolute, or effective permeability to nonw-wetting phase at initial conditions of  $S_{wi}$ )  $(m^2)$ 

 $f_{\rm nw}$  is the fractional flow of non-wetting phase (-)

 $k_{rnw}$  is the relative permeability to non-wetting phase (-)

 $\mu_{\rm nw}$  is the viscosity of non-wetting phase (Pa.s)

u is the average velocity of approach, Q/A (m/s)[21]

To replace the unobservable distance by a measurable outlet quantity, Buckley-Leverett theory relates front advancement to the outlet (instantaneous) fractional flow  $f'_w$ :

$$dx = dx_{S_w} = LQ_w \, df'_w = L \frac{df'_w}{f'_{wL}} \tag{4.41}$$

where

 $f'_w$  : is the water fractional flow at the outlet

 $f'_{wL}$ : is the outlet fractional flow at the shock front saturation

substituting them in  $\Delta p$ :

$$\Delta P = -\frac{\mu_{\text{nw}} u L}{k f'_{wL}} \int_0^{f'_{wL}} \frac{f_{\text{nw}}}{k_{rnw}} df'_w$$
 (4.42)

$$\int_{0}^{f'_{wL}} \frac{f_{\text{nw}}}{k_{rnw}} df'_{w} = -\frac{k f'_{wL} \Delta P}{\mu_{\text{nw}} uL}$$
(4.43)

before injecting water at the beginning of the experiment, Darcy's law can be written as:

$$\left(\frac{u}{\Delta P}\right)_i = -\frac{kk_{rnw,\text{max}}}{\mu_{\text{nw}}L} \tag{4.44}$$

where  $k_{rnw,max}$  is the maximum relative permeability at  $S_{wi}$ , substituting it in Eq.4.43:

$$\int_0^{f'_{wL}} \frac{f_n w}{k_{rnw}} df'_w = \frac{f'_{wL}}{k_{rnw,\text{max}}} \frac{\left(\frac{u}{\Delta P}\right)_i}{\left(\frac{u}{\Delta P}\right)}$$
(4.45)

Relative injectivity  $I_r$  was defined by Rapport and Leas in terms of intake capacity  $(u/\Delta P)$  [21]:

$$I_r = \frac{\left(\frac{u}{\Delta P}\right)}{\left(\frac{u}{\Delta P}\right)_i} \tag{4.46}$$

substituting it in Eq 4.45 and differentiating with respect to  $f'_{wL}$ :

$$\frac{f_{nwL}}{k_{rnwL}} = \frac{d\left(\frac{f'_{wL}}{I_r}\right)}{df'_{wL}} \tag{4.47}$$

using the relation in Eq 4.33, the following equation can be obtained for determination of relative permeability to non-wetting phase:

$$k_{rnwL} = f_{nwL} \frac{d \left[ 1/Q_{wi} \right]}{d \left[ 1/(Q_{wi}I_r) \right]}$$
(4.48)

and using the relative permeability ratio from Welge's solution (Eq 4.30) the relative permeability to water is obtained as:

$$k_{rwL} = k_{rnwL} \frac{\mu_w (1 - f_{nwL})}{\mu_{nw} f_{nwL}}$$
(4.49)

In summary, for each time step, one evaluates  $S_{wL}$  (outlet/shock saturation inferred via Buckley-Leverett) and computes the corresponding  $k_{rnwL}$  and  $k_{rwL}$ . Repeating over the dataset yields the full relative-permeability curves [21].

## 4.2.5 Applying for scCO<sub>2</sub>-Brine Systems

JBN method was originally developed for oil-water systems under some assumptions that are violated by scCO2-water systems. Not taking into consideration this violation and challenges introduced by  $CO_2$  leads to a significant measurement errors and thus wrong relative permeability curves.

One of the fundamental assumptions of the JBN method is that the flowing fluids are incompressible. However, this assumption is not valid when one of the fluids is supercritical  $CO_2$  (scCO<sub>2</sub>), which is a compressible fluid whose viscosity and density vary significantly with pressure and temperature. The variation of  $CO_2$  properties was discussed in Section 4.1 "Steady-State Technique" and illustrated in the accompanying graphs showing the dependence of density and viscosity on pressure and temperature. This compressibility variation causes unsteady injection rates, since changes in  $CO_2$  density lead to fluctuations in the volumetric flow rate, thereby violating the Buckley-Leverett assumption of a constant total flow rate [34].

Another assumption of the JBN method that is violated in the case of  $CO_2$  displacement is the piston-like displacement at the fluid front, where the injected phase uniformly pushes the defending phase, maintaining a sharp and stable saturation front.

The viscosity of  $scCO_2$  typically ranges between 0.03–0.08 cP, which is significantly lower than that of brine (0.5–1 cP). This large viscosity contrast produces an unfavorable

mobility ratio  $(M \gg 1)$  when the less viscous fluid  $(scCO_2)$  displaces the more viscous fluid (brine). Such unfavorable mobility conditions lead to viscous fingering, a phenomenon characterized by interfacial instability between two fluids of contrasting viscosities. As a result,  $CO_2$  penetrates the brine non-uniformly and propagates preferentially through high-permeability channels, surpassing the saturation front due to its higher mobility. Some of these fingers reach the outlet prematurely, causing an early breakthrough of  $CO_2$  [35, 32].

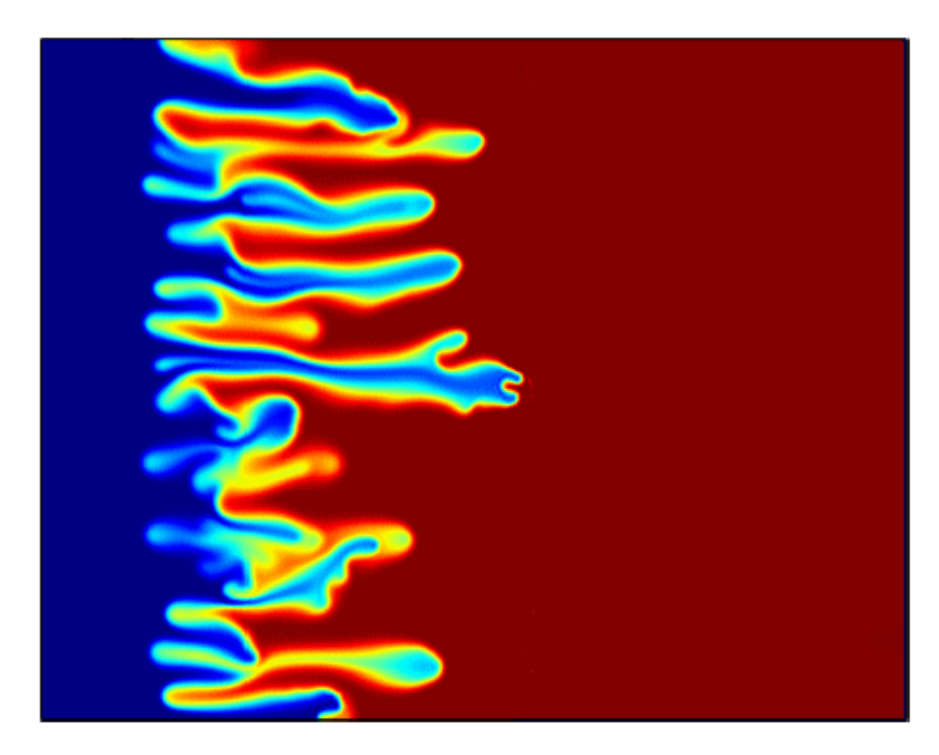


Figure 4.11: Viscous Fingering Phenomena [36]

Applying Welge's extension solution to determine the average and front water saturation in systems exhibiting viscous fingering leads to substantial errors. When  $CO_2$  reaches the outlet before fully displacing brine, the calculated average water saturation is overestimated, while the front saturation becomes physically unrealistic. This occurs because the slope of the tangent on the fractional flow curve no longer represents the true advancing front, but rather a distorted mixture of fingered regions and bypassed zones.

Furthermore, the JBN method determines the non-wetting phase relative permeability using the fractional flow of the non-wetting phase at the outlet  $(f_{\text{nw,L}})$ , assuming that this fractional flow arises from a piston-like displacement. In the presence of viscous fingering, the non-wetting phase  $(CO_2)$  reaches the outlet much earlier than a piston-like displacement front. Consequently, the measured  $f_{\text{nw,L}}$  corresponds to preferential flow through channels rather than the arrival of a stable front, resulting in a rapid rise in  $f_{\text{nw,L}}$  while the brine saturation in the core remains high.

Using such a fractional flow in the JBN formulation for the non-wetting phase relative permeability links the computed  $k_{r,\text{nw}}$  values to erroneous saturation dynamics instead of the smooth front advance on which the method is based. This leads to an overestimation of the non-wetting phase relative permeability because a high  $f_{\text{nw,L}}$  is observed at a relatively

small pressure drop, which the JBN formulation interprets as a high mobility of the non-wetting phase. Consequently, since the total mobility is shared between the two phases, this overestimation of  $k_{r,\text{nw}}$  results in an underestimation of the wetting phase relative permeability.

Therefore, the presence of viscous fingering invalidates one of the fundamental assumptions of the JBN analysis, making the obtained relative permeability curves during drainage non-representative of the true two-phase flow behavior in  $scCO_2$ -brine systems.

# Chapter 5

# Capillary End Effect

## 5.1 Steady State Experiments

One of the greatest challenges in measuring relative permeability curves is the capillary end effect (CEE). This phenomenon originates from the discontinuity in capillary pressure at the outlet of the core: within the porous medium, the capillary pressure is finite, whereas at the exit into the free-flow region, capillary pressure drops to zero (all fluids are at the same pressure). To balance this discontinuity, an accumulation of the wetting phase occurs near the outlet, creating a non-uniform saturation profile and influencing the pressure drop measured across the entire core. The capillary end effect was first observed and described by Leverett in 1941 [21] [37].

This localized enrichment of the wetting phase artificially increases its apparent mobility, leading to an overestimation of the wetting-phase relative permeability. Conversely, the non-wetting phase experiences additional resistance near the outlet, causing an underestimation of its relative permeability. Experimental studies indicate that the capillary end effect can result in errors of up to 15% in wetting-phase saturation, 12% in wetting-phase relative permeability, and 28% in non-wetting-phase relative permeability [37] [38].

The saturation gradient profile in a linear system can be obtained from the combination of Darcy's law and capillary pressure equation as follows:

$$-dP_w = \frac{q_w \mu_w \, dL}{k_w A} \tag{5.1}$$

$$-dP_{nw} = \frac{q_{nw}\mu_{nw}\,dL}{k_{nw}A}\tag{5.2}$$

$$dP_c = dP_{nw} - dP_w (5.3)$$

By combining these 3 equations:

$$\frac{dP_c}{dL} = \frac{1}{A} \left[ \frac{q_w \mu_w}{k_w} - \frac{q_{nw} \mu_{nw}}{k_{nw}} \right]$$
 (5.4)

where

 $dP_c$  is the capillary pressure gradient within the core of length L,

A is the cross-sectional area of the core,

 $q_w$  and  $q_{nw}$  are the volumetric flow rates of the wetting and the non-wetting phases, respectively,

 $\mu_w$  and  $\mu_{nw}$  are the viscosities of the wetting and the non-wetting phases, respectively,  $k_w$  and  $k_{nw}$  are the permeabilities of the wetting and the non-wetting phases, respectively [21].

Since the capillary pressure is function of saturation, and saturation is function of length, then:

$$\frac{dP_c}{dL} = \frac{dP_c}{dS_w} \cdot \frac{dS_w}{dL} \tag{5.5}$$

Combining Eq 4.4 and 4.5:

$$\frac{dS_w}{dL} = \frac{1}{A} \left[ \frac{q_w \mu_w}{k_w} - \frac{q_{nw} \mu_{nw}}{k_{nw}} \right] \cdot \frac{1}{\frac{dP_c}{dS_w}}$$

$$(5.6)$$

This equation represents the change in wetting-phase saturation with length [21].

It can be observed from the equation that high flow rates can change saturation profile faster than low flow rates, which reduces the magnitude of capillary end effect, and that was confirmed by Richardson et al. 1952 when he conducted an experiment on a core sample and measured the relative permeability relationships at different flow rates and he noticed a good correspondence between the theoretical and experimental saturation gradients and a reduction in capillary end effect at high flow rates [21].

A qualitative illustration of the influence of the capillary end effect on the saturation profile is presented in the following figure:

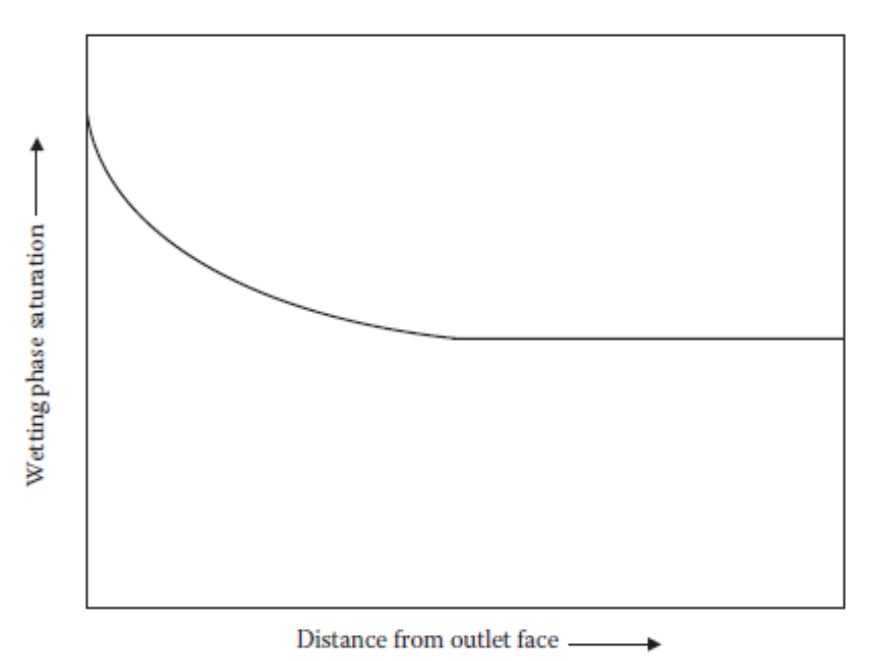


Figure 5.1: Capillary End Effect [21]

The extent of the capillary end effect is governed by the ratio of viscous to capillary forces, commonly expressed through the capillary number:

$$Ca = \frac{\mu v}{\sigma} \tag{5.7}$$

where  $\mu$  is the viscosity of the displacing fluid, v is the Darcy velocity, and  $\sigma$  is the interfacial tension. When viscous forces dominate, the capillary end effect zone is confined to a smaller region, which can be achieved by using higher flow rates and higher fluid viscosities. Conversely, at lower flow rates and viscosities, capillary forces dominate and the capillary end effect extends further into the core. In addition, a shorter core length does not increase capillary forces themselves, but it allows the capillary end effect zone to occupy a larger fraction of the sample length. This enhances its impact on the average saturation profile and leads to distortions in the measured relative permeabilities.

The effect of the capillary end effect is more pronounced during single-phase flow than during multiphase co-injection. For intermediate fractional flows  $(0 < f_w < 1)$ , the viscous forces of both fluids act simultaneously, confining the saturation gradient to a narrow zone at the outlet. By contrast, at the endpoints  $(f_w = 0 \text{ and } f_w = 1)$ , when only one phase is mobile, the capillary discontinuity dominates and the distortion of relative permeability data becomes significant.

At  $(f_w = 0)$ , only the non-wetting phase is flowing. To satisfy the condition of vanishing capillary pressure at the outlet, the saturation gradient of the wetting phase develops earlier in the core, raising the average wetting saturation above the irreducible value. This increases the resistance to non-wetting flow and leads to an underestimation of the non-wetting endpoint relative permeability.

At  $(f_w = 1)$ , only the wetting phase is flowing. The immobility of the non-wetting phase causes water saturation to rise above its true endpoint value  $(1-S_{nwr})$ , which corresponds to an apparent reduction in  $S_{nwr}$ . This excess water accumulation near the outlet enhances the apparent mobility of the wetting phase, resulting in an overestimation of the wetting endpoint relative permeability

Several techniques have been proposed to reduce the capillary end effect (CEE): (i) raising the total flow rate to increase viscous forces relative to capillary forces; (ii) testing longer cores so the CEE zone occupies a smaller proportion of the sample; and (iii) adding capillary-connected core segments at one or both ends to shift the capillary discontinuity outside the measurement interval. These methods face practical and interpretational limits. High rates risk turbulent flow and invalidate Darcy-based analysis; long plugs may exceed core-holder capacity or introduce additional heterogeneity; and end extensions complicate handling and may still differ from reservoir rock. Thus, while these measures can attenuate CEE, they are not universally representative of reservoir conditions [16].

The experimental approaches, when successful, can minimize the capillary end effect (CEE) but cannot eliminate it completely. In contrast, mathematical methods are more precise in this regard, as they aim to remove the effect entirely from the calculation. Huang and Honarpour (1996) introduced a mathematical method that couples relative permeability and capillary pressure; however, its applicability is limited because it requires the existence of a specific  $k_r$ - $p_c$  relationship, which may not always hold [37].

Gupta and Maloney (2014) proposed the Intercept Method, which relies on performing steady-state experiments at constant fractional flow but varying total rates. By plotting the average water saturation against  $1/q_o$ , the unaffected saturation can be obtained from the intercept with the y-axis, while the non-wetting phase relative permeability is determined from the slope of a  $\Delta p$  vs.  $q_{nw}$  plot, with the wetting-phase relative permeability then obtained from flow partitioning. Although this method provides correct results, it was based on an incorrect assumption that the ratio  $L_{cee}/L$  is constant, whereas later work demonstrated that  $L_{cee} \propto 1/q_o$  [37].

Reed and Maas (2018) validated the robustness of the Intercept Method through numerical experiments and real datasets, showing that it remains reliable even when relative permeability curves do not follow Corey-type functions. Andersen (2017, 2021) developed a related forward-modeling approach that also uses intercept-type analysis, but it requires assuming a specific functional form of capillary pressure and introduces new definitions such as "effective relative permeability," which limits its generality [37].

Nazari and Jamiolahmadi (2019) attempted to correct CEE by formulating a system of eight nonlinear equations with eight unknowns, which they solved using a least-squares algorithm in MATLAB. Their method provided reliable estimates of the relative permeabilities and the unaffected water saturation from four steady-state experiments at each fractional flow. However, other calculated parameters, such as the average saturation and pressure drop within the CEE region, as well as the CEE length, were found to be inconsistent and unreliable [37].

Among all these methods, the **Modified Intercept Method** of Goodarzian and Sorbie (2023) currently offers the most rigorous and general framework. It corrects the erroneous assumption of Gupta and Maloney by showing that  $L_{cee}/L$  is a function of flow rate, and crucially, it does not require specifying the shape of the capillary pressure function or introducing additional parameters. Instead, it uses only mass balance and general pressure equations, requiring only the existence of a small unaffected zone to deliver corrected relative permeability curves. In addition to that it works for all wetting systems [37].

## 5.1.1 Modified Intercept Method

#### Correcting the Wrong Assumption of the Original Intercept Method

As mentioned previously, the original Intercept Method presented by Gupta and Maloney (2014) was based on a incorrect assumption that the ratio  $L_{cee}/L$  is constant. The Modified Intercept method proved that it is proportional to the inverse of oil flow rate. Consider the following schematic representing the saturation profile in affected and unaffected region of a water-wet system:

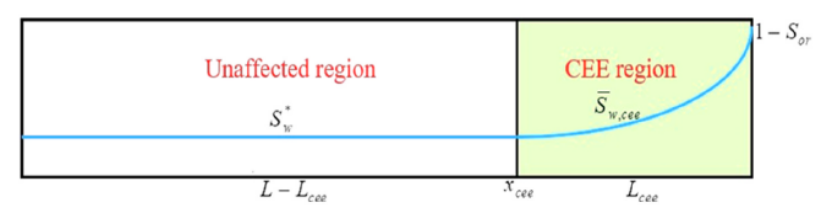


Figure 5.2: Sw profile in SS condition in water wet system [37]

Here,  $S_w^*$  is the water saturation in the unaffected region,  $\bar{S}_{w,\text{cee}}$  is the average water saturation in the affected region,  $x_{cee}$  is the location where CEE region starts, and  $L_{\text{cee}} = L - x_{\text{cee}}$  is the length of the affected region [37].

Starting from Darcy's law for each phase and the definition of capillary pressure:

$$q_w = -kA\lambda_w \nabla p_w \tag{5.8}$$

$$q_o = -kA\lambda_o \nabla p_o \tag{5.9}$$

$$p_c = p_o - p_w \tag{5.10}$$

We obtain:

$$\nabla p_c = \frac{q_w}{kA\lambda_w} - \frac{q_o}{kA\lambda_o} \tag{5.11}$$

Considering a 1-D displacement process in x-direction, then:

$$\frac{dp_c}{dx} = \frac{1}{kA} \left( \frac{q_w}{\lambda_w} - \frac{q_o}{\lambda_o} \right) \tag{5.12}$$

Using the chain rule  $\frac{dp_c}{dx} = \frac{dp_c}{dS_w} \frac{dS_w}{dx}$ , the following equation is observed:

$$dx = kA \frac{\frac{dp_c}{dS_w}}{\left(\frac{q_w}{\lambda_w} - \frac{q_o}{\lambda_o}\right)} dS_w$$
 (5.13)

Integrating over the affected region:

$$\int_{x_{cee}}^{L} dx = \int_{S_w^*}^{1-S_{or}} kA \frac{\frac{dp_c}{dS_w}}{\left(\frac{q_w}{\lambda_w} - \frac{q_o}{\lambda_o}\right)} dS_w$$
 (5.14)

$$L - x_{cee} = L_{cee} = kA \int_{S_w^*}^{1 - S_{or}} \left[ \frac{\frac{dp_c}{dS_w}}{\left(\frac{q_w}{\lambda_w} - \frac{q_o}{\lambda_o}\right)} \right] dS_w$$
 (5.15)

Defining F as  $q_w/q_o$ ,

$$L_{cee} = \frac{1}{q_o} kA \int_{S_w^*}^{1-S_{or}} \left[ \frac{\frac{dp_c}{dS_w}}{\left(\frac{F}{\lambda_w} - \frac{1}{\lambda_o}\right)} \right] dS_w = \frac{a}{q_o}$$
 (5.16)

where a is a constant that depends on F, but not on the absolute flow rates. Thus, for fixed F,  $q_oL_{cee} = a$  remains constant, and the CEE length decreases as  $q_o$  increases [37].

Pressure drop of the oil phase in the CEE region is:

$$\Delta p_{cee} = \int dp_o = \int_{L_{cee}}^{L} \frac{q_o}{kA\lambda_o} dx = \int_{S_w^*}^{1-S_{or}} \frac{q_o}{kA\lambda_o} kA \frac{\frac{dp_c}{dS_w}}{\left(\frac{q_w}{\lambda_w} - \frac{q_o}{\lambda_o}\right)} dS_w$$
 (5.17)

$$= \int_{S_w^*}^{1-S_{or}} \frac{\frac{dp_c}{dS_w}}{\left(1 - \frac{\lambda_w F}{\lambda_o}\right)} dS_w$$

Average water saturation in the CEE region:

$$\bar{S}_{w,\text{cee}} = \frac{\int_{x_{cee}}^{L} S_w \, dx}{\int_{x_{cee}}^{L} dx} \tag{5.18}$$

Substituting Eq 4.13 in Eq 4.18

$$\bar{S}_{w,\text{cee}} = \frac{\int_{S_w^*}^{1-S_{or}} S_w \frac{\frac{dp_c}{dS_w}}{\left(\frac{F}{\lambda_w} - \frac{1}{\lambda_o}\right)} dS_w}{\int_{S_w^*}^{1-S_{or}} \frac{\frac{dp_c}{dS_w}}{\left(\frac{F}{\lambda_w} - \frac{1}{\lambda_o}\right)} dS_w}$$

$$(5.19)$$

It is demonstrated from these expressions that, while the CEE length  $L_{\text{cee}}$  decreases as the oil flow rate increases, the oil-phase pressure drop  $\Delta p_{\text{cee}}$  and the average water saturation  $\bar{S}_{w,\text{cee}}$  in the CEE region depend only on F. Thus, for fixed F, both remain constant irrespective of the absolute flow rates [37].

#### Determination of Water Saturation in the Unaffected Region

According to mass balance, the average water saturation in the system is:

$$\bar{S}_w L = S_w^* (L - L_{cee}) + \bar{S}_{w,cee} L_{cee}$$
 (5.20)

Where  $\bar{S}_w$  is the average water saturation in the whole system, L is the total length of the system,  $S_w^*$  is the water saturation in the unaffected region,  $L_{cee}$  is the length of the CEE region, and  $\bar{S}_{w,\text{cee}}$  is the average water saturation in the CEE region[37]. According to Eq 4.16,  $L_{cee} = a/q_o$  then

$$\bar{S}_w L = S_w^* \left( L - \frac{a}{q_o} \right) + \bar{S}_{w,\text{cee}} \frac{a}{q_o}$$
 (5.21)

Dividing by L:

$$\bar{S}_w = S_w^* \left( 1 - \frac{a}{q_o L} \right) + \bar{S}_{w,\text{cee}} \frac{a}{q_o L} = S_w^* + \frac{a}{L} \left( \bar{S}_{w,\text{cee}} - S_w^* \right) \frac{1}{q_o}$$
 (5.22)

According to Eq 4.22, repeating the steady-state experiment at a fixed ratio F and varying the injection flow rates produces a straight-line relationship between the average water saturation  $\bar{S}_w$  and the reciprocal of oil flow rate  $1/q_o$ . The intercept of this line on the y-axis corresponds to the water saturation in the unaffected region,  $S_w^*$  [37].

## **Determination of Relative Permeabilities**

The oil phase pressure drop in the system is the sum of pressure drop in the unaffected region and affected region as follows:

$$\Delta p_{\text{oil-total}} = \Delta p_{\text{unaffected region}} + \Delta p_{\text{capillary end effect region}} = \frac{q_o(L - L_{\text{cee}})}{k A \lambda_o} + \Delta p_{\text{cee}}$$
 (5.23)

substituting  $L_{cee} = a/q_o$ ,

$$\Delta p_{\text{oil-total}} = \frac{q_o \left( L - \frac{a}{q_o} \right)}{k A \lambda_o} + \Delta p_{\text{cee}} = \frac{L}{k A \lambda_o} q_o - \frac{a}{k A \lambda_o} + \Delta p_{\text{cee}}$$
 (5.24)

Plotting  $\Delta P_{oil-total}$  vs  $q_o$  for different flow rates but constant F, a straight line with slope  $L/KA\lambda_o$  is obtained. From this slope the oil mobility in the unaffected region is obtained and thus relative permeability to oil for this specific water saturation in obtained  $(k_{ro} = \mu_o \lambda_o)$  [37].

The pressure drop in water phase is:

$$q_w = -kA\lambda_w \left(\nabla p_o - \nabla p_c\right) \tag{5.25}$$

Since capillary pressure gradient in unaffected region is zero and substituting oil gradient, then:

$$q_w = \frac{\lambda_w}{\lambda_o} q_o \tag{5.26}$$

from this equation the mobility of water phase is determined and thus relative permeability of water at a specific water saturation is determined  $(k_{rw} = \mu_w \lambda_w)$ .

For each saturation level, the experiment must be conducted at same ratio F at least 3 times to obtain the straight line and calculate the corresponding relative permeabilities [37].

## Validation of the Approach

To verify the method, a steady state numerical experiment was performed using 1-D simulator on synthetic core with predefined relative permeability and capillary pressure functions,hence, the corresponding "true" relative permeability curves were known. The core properties were:  $L=15\,\mathrm{cm},\,A=20\,\mathrm{cm}^2,\,S_{wc}=0.2,\,S_{or}=0.25,\,\mu_o=3\,\mathrm{cp},\,\mu_w=1\,\mathrm{cp},$  and  $k=50\,\mathrm{mD}$  [37].

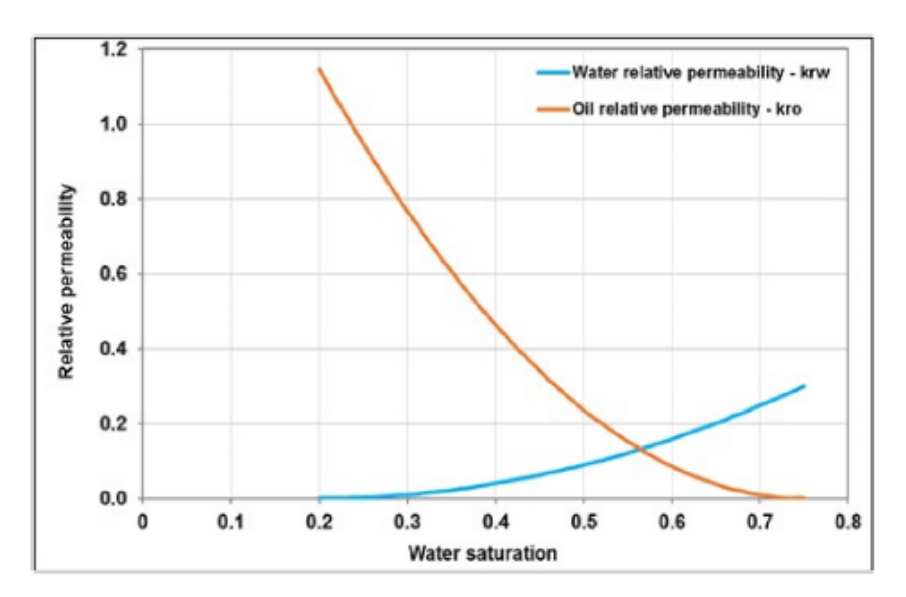


Figure 5.3: Relative permeability curves obtained from the known relative permeability functions [37]

The data obtained from the simulation: average water saturation in the core and pressure difference across the core, are used as input to the Modified Intercept Method. A back inverse calculation is performed to obtain the relative permeability points and construct the relative permeability curves. If the obtained relative permeability points lies exactly on the original true relative permeability curves, then the method is valid [37].

For each data point on the relative permeability curve  $(k_{rw} \text{ and } k_{ro} \text{ vs } S_w)$ , the numerical experiment is performed at least 3 times at a constant ratio F but different flow rates to construct a straight line. For each run, the average water saturation is plotted vs reciprocal oil flow rate to obtain the average water saturation in the unaffected zone from the y-intercept, and pressure drop vs oil flow rate to obtain the mobility of oil from the slope and thus the relative permeability of oil. Water relative permeability is then determined from the relation between oil and water relative permeability. For each F ratio the following figures are obtained [37]:

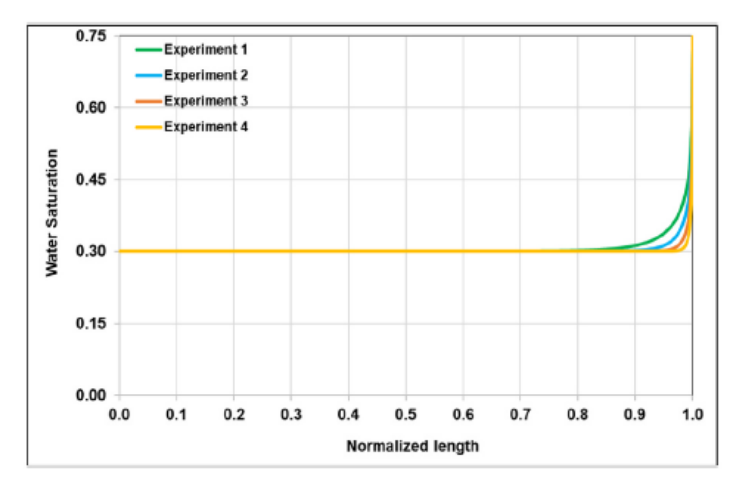


Figure 5.4: Water saturation profile at SS conditions for different flow rates at same F in a water-wet system [37]

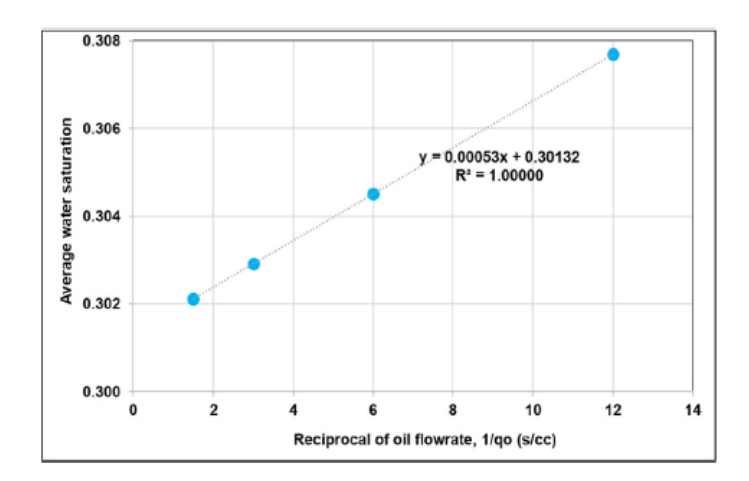


Figure 5.5: Average water saturation in the core vs reciprocal oil flow rate [37]

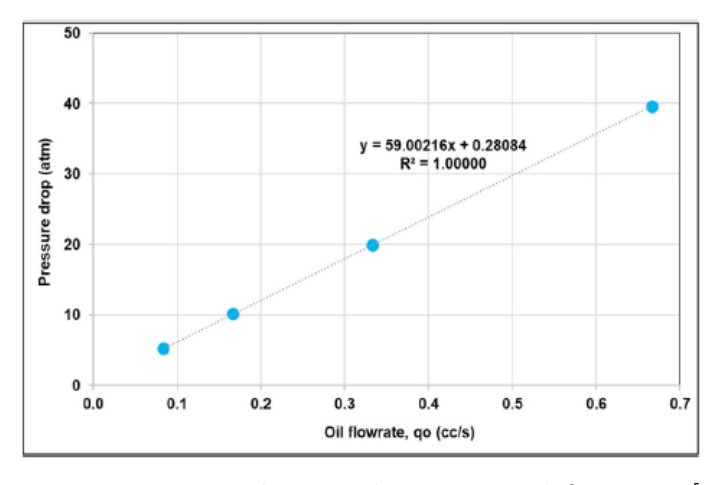


Figure 5.6: Pressure drop in the core vs oil flow rate [37]

This process is repeated for 8 different values of F to obtain several relative permeability points and compare them with the original one, the following figure shows a high accuracy

of the method as the obtained relative permeability points obtained from the Modified Intercept Method lies exactly on the original relative permeability curves:

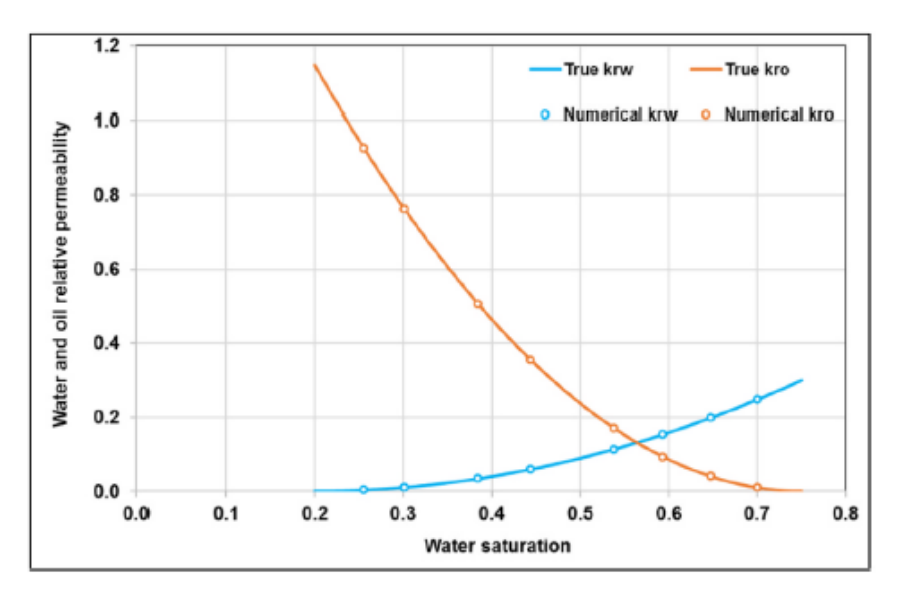


Figure 5.7: Comparison of corrected relative permeability data and original curves [37]

The method was proved to work for water-wet system as for oil-wet and mixed-wet systems, the only difference is that in the oil-wet system the average water saturation in the system will decrease as reciprocal oil flow rate will increase, and this is observed in the graph with a negative slope [37].

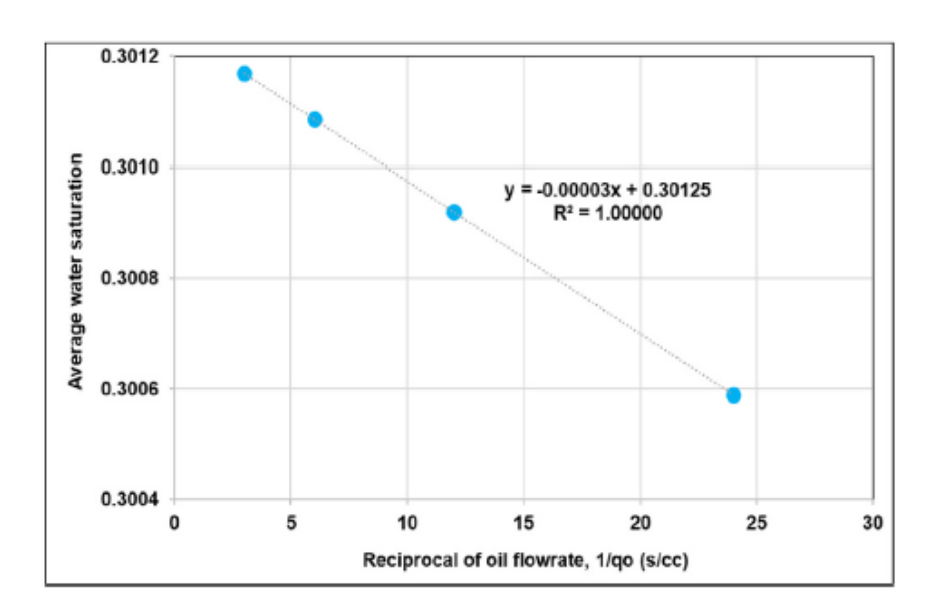


Figure 5.8: Average water saturation in the core vs reciprocal oil flow rate for oil-wet systems [37]

## 5.2 Unsteady State Experiments

The impact of the capillary end effect (CEE) is generally more pronounced in *unsteady-state* (USS) experiments, since there is no co- injection of fluids as in *steady-state* (SS) tests that confines the effect to the very last portion of the core. At the outlet, the capillary pressure inside the porous medium must drop to zero in the external free-fluid region, which creates a discontinuity. To satisfy this boundary condition, the wetting phase accumulates near the outlet.

This accumulation distorts the measured displacement data. Specifically, part of the wetting phase is retained in the outlet zone instead of being produced, which alters the calculated fractional flow  $f_w$ . As a result, the wetting phase appears more mobile than it actually is, leading to an **overestimation of the wetting-phase relative permeability**. Conversely, the non-wetting phase faces additional resistance to flow through this saturated outlet region, which increases the measured pressure drop and leads to an **underestimation of the non-wetting-phase relative permeability**.

## 5.2.1 Extended JBN Method

Chen et al. (2016) extended the JBN method by incorporating local measurements of fractional flow, pressure drop (using pressure taps), and saturation. By applying the same mathematical inversion as in the regular JBN method, the relative permeabilities of both phases can be obtained at each pressure tap, which are located away from the outlet and thus less affected by the capillary end effect, making the results more reliable [39].

The pressure drop of each section is obtained from the pressure taps, while saturation is not inferred from average values as in the conventional JBN method, but directly measured using X-ray Computed Tomography (CT) along the core. The local fractional flow can then be calculated from the saturation profile in two ways: (i) based on a fractional flow analysis, or (ii) using a mass balance approach. Since scanning the whole core takes approximately 6 minutes, the fluids continue to flow during the scan, meaning that the saturation measured near the outlet does not exactly correspond to the saturation measured near the inlet at the same instant. To overcome this, the saturation profiles are treated as instantaneous snapshots when used for calculating local water fractional flow. This approximation introduces only a small error, estimated to be less than 3% for the fractional flow method and less than 7% for the mass balance method. Therefore, in this work, greater emphasis is placed on the fractional flow method [39].

The boundary condition of the fractional flow method is that the fractional flow of the defending phase is always zero at the inlet, since only the invading phase is injected [39]. The initial condition is that, at the onset of injection, the core is fully saturated with the defending phase:

**Boundary condition:** 

$$f_d(x=0, t>0) = 0 (5.27)$$

Initial condition:

$$S_d(x, t = 0) = 1 (5.28)$$

According to Buckley-Leverett:

$$\frac{df_d}{dS_d} = \frac{\phi x}{ut} \tag{5.29}$$

Integrating to get local  $f_d(x,t)$ :

$$f_d(x,t) = f_d(0,t) + \int_{S_d(0,t)}^{S_d(x,t)} \frac{df_d}{dS_d} dS_d$$
 (5.30)

where  $f_d(0,t)$  is always zero according to the boundary condition.

Since CT scans give the saturation as discrete slices x [39], the integral is rewritten as summation:

$$f_d(x=i,t) = f_d(x=1,t) + \sum_{x_0=2}^{x_0=i} \left( \frac{df_d}{dS_d} \Big|_{x_0=1,t} \cdot \left[ S_d(x_0,t) - S_d(x_0-1,t) \right] \right)$$
 (5.31)

where first slice at x-1 is set to  $f_d=0$  as a boundary condition. This equation represents the fractional flow of the defending phase at any position x at any time t.

#### Validation of the Approach

To verify this extended JBN method, Chen et al. performed a primary drainage unsteady state experiment by injecting  $CO_2$  to a 60.8 cm Berea sandstone core fully saturated with brine. Four pressure taps was equipped in the core at different locations from the inlet to monitor the pressure drop continuously using differential pressure transducers. Saturation profile evolution through time and space is obtained using medical X-ray CT scanner by vertically mounting the core holder on a vertical positioning system that move up and down. It provides 60 slices of CT images with a thickness of 1 cm each. The fractional flow of the defending phase is then obtained from the fractional flow method that depends on the saturation profile [39].

The results of the experiment are shown below:

#### Saturation Profile

The following graph represents the evolution of the defending phase (water) saturation profile with injection time. The early profile at 0.05 PV shows that the saturation front of  $CO_2$  is at 20 cm from the inlet. Breakthrough time occurs at 0.20 PV where the saturation of the water at the outlet is around 0.95. As it can be noticed from the saturation profile that local measurements will allow measuring relative permeability at saturation range higher than that when relying only on the outlet measurements [39].

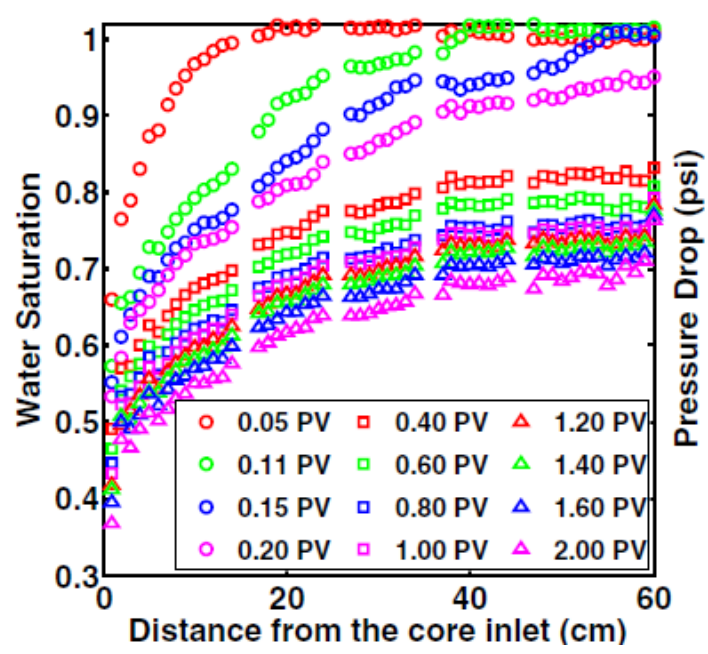


Figure 5.9: Water saturation profile at different injection times [39]

## Pressure Drop

The pressure drop profile shows the impact of capillary end effect on the pressure drop. The global pressure drop is around 3 psi greater than the local measurement of pressure drop. Moreover, it is oscillating by 1 psi most likely due to sudden change of capillary forces when the front arrives to the outlet. Before the arriving of the  $CO_2$  front to the section of the pressure tap, it will show a constant pressure drop due to the flow of brine only [39].

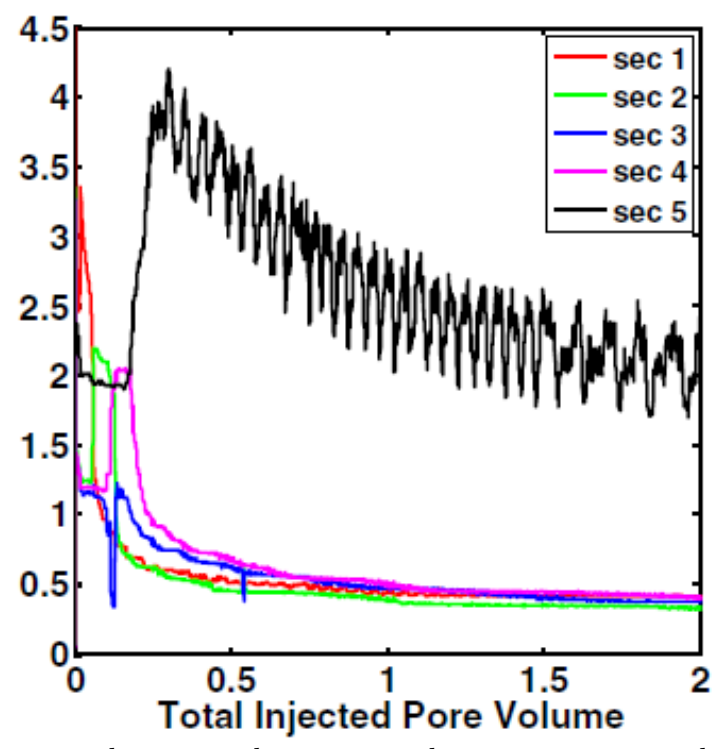


Figure 5.10: Pressure drop at each section with respect to injected pore volumes [39]

#### Water Fractional Flow

The water fractional flow is calculated according to the fractional flow method of the defending phase. As expected the results shows that fractional flow of the defending phase at a specific location is decreasing with time due to the invasion of the injected fluid. Also for a specific time, the fractional flow of the defending phase is increasing from the inlet to the outlet as the the invading phase start displacing from inlet to outlet. At early time before the breakthrough (<0.15 PV), the fractional flow shows 1 after the front as this zone is not invaded yet.

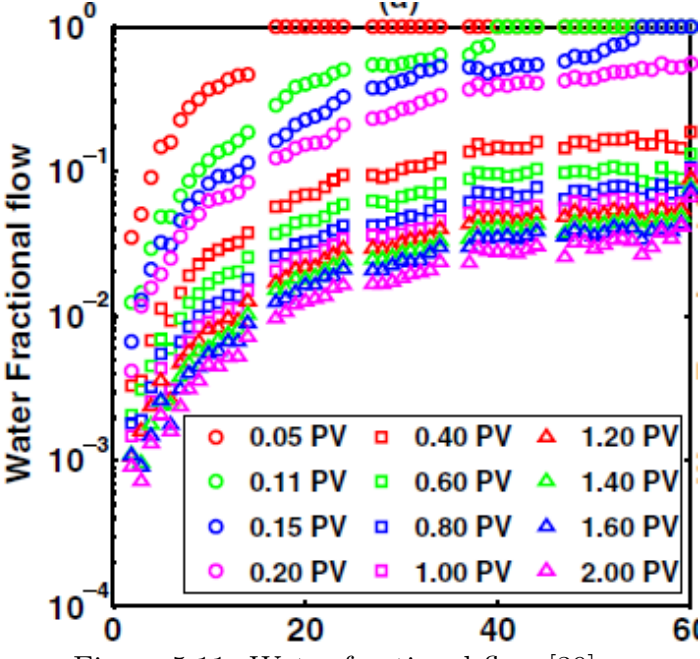


Figure 5.11: Water fractional flow [39]

#### Relative Permeability Calculation

After having the pressure drop, saturation profile, and the fractional flow of the defending phase at each section, relative permeability of the defending phase and thus the relative permeability of the injected phase at each section can be calculated using the following equations of the JBN method:

$$k_{rd} = \frac{f_d L Q_t \mu_d}{KA} \frac{d\left(\frac{1}{t_d}\right)}{d\left(\frac{\Delta P}{t_d}\right)}$$
(5.32)

$$k_{ri} = k_{rd} \frac{\mu_i (1 - f_{d2})}{\mu_d f_d} \tag{5.33}$$

where  $t_d$  is the injected pore volume.

Since the defending relative permeability depends on differentiating  $d(1/t_d)/d(\Delta p/t_d)$ , using the raw data will lead to a wrong estimation of the relative permeability because of the noisy pressure measurement. The data of  $1/t_d$  vs  $\Delta p/t_d$  should be fitted with a third degree polynomial to remove the noise and produce reliable relative permeability values. The first 3 points (0.25-0.35 PV) are not used for calculation since data have large spacing due high pressure drop changes at the beginning where flow regime is not yet

stable, so any small error in pressure drop will reflect a big error in the derivative and thus in the relative permeability calculation [39]. The following graphs show the fitted data and relative permeability calculated from extended JBN method at each section and from regular JBN method using global pressure drop:

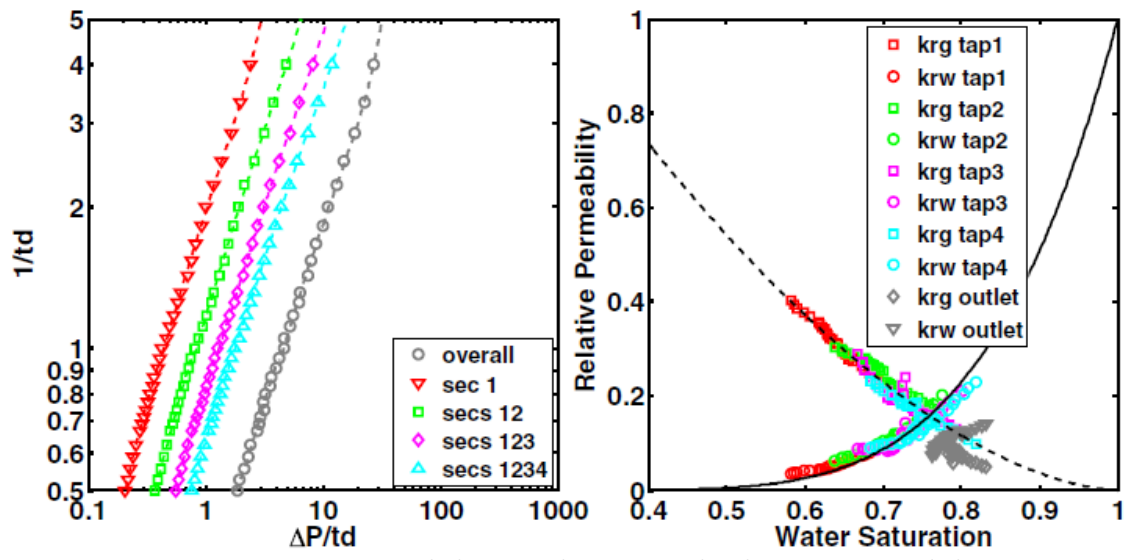


Figure 5.12: Fitted data and measured relative permeability

The relative permeability obtained from pressure taps using extended JBN method follows a Corey-type model with  $S_{wr} = 0.28$ ,  $n_w = 4.53$ ,  $n_g = 1.68$  fitting parameters, with saturation ranges that overlap between taps, and tap 1 produces the lowest water saturation. On the other hand the relative permeabilities obtained by regular JBN method are 40% lower than the Corey fit with a very limited water saturation range (0.76-0.83) compared to the range obtained by the extended method (0.58-0.82) [39].

These obtained relative permeability data have some uncertainty that can be divided into two categories: First category is the uncertainty related to saturation measurement from CT scans limits (0.4%), the second category is the uncertainty in calculating relative permeability from pressure drop, local fractional flow, and absolute permeability. The uncertainty in pressure drop measurement is 3% due to sensor fluctuations and noise. Water fractional flow measured using fractional flow method has uncertainty about 3% as previously indicated. Since absolute permeability changes within the core, its uncertainty is about 10%. This leads to an 11% uncertainty in the brine relative permeability and 10% in  $CO_2$  relative permeability by applying uncertainty propagation to relative permeability equations [39].

The extended JBN method is compared with a steady state experiment results conducted under the same conditions at the same rock. The comparison shows a consistency between the extended method results and steady state results, The results are within  $\pm 40\%$  of the Corey-type fits, but this difference is not due to conceptual bias in the method as in regular JBN method due to capillary end effect, but due to experimental uncertainties discussed before, which is considered acceptable. So extended JBN method can be considered a time saving method, but it requires in-situ measurements for relative permeability measurements [39].

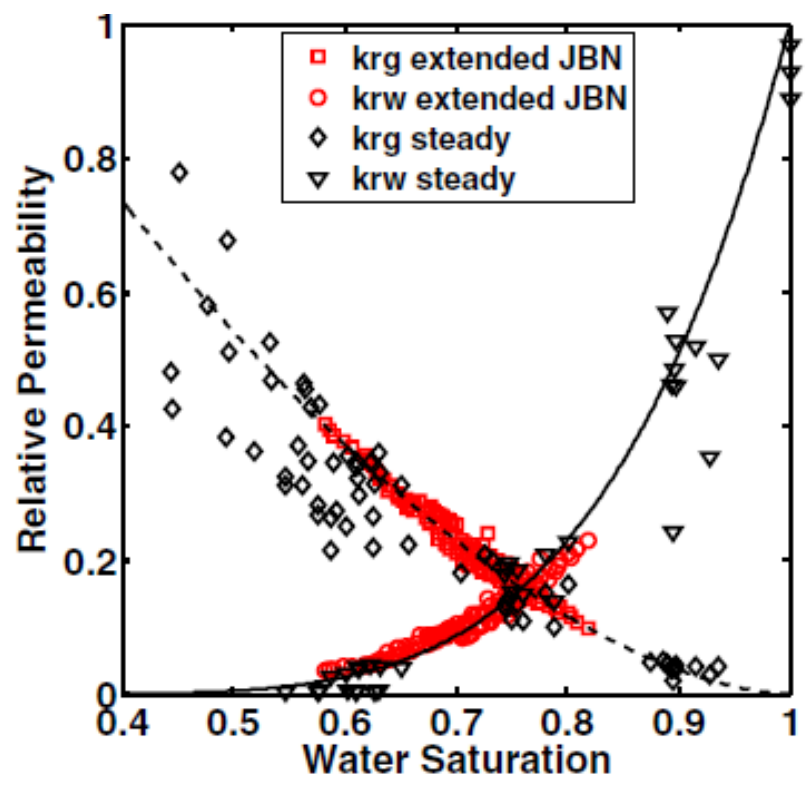


Figure 5.13: Comparison between SS results and extended JBN results [39]

## 5.3 Endpoints Determination

Since the irreducible water saturation is difficult to achieve experimentally, the endpoint relative permeabilities are not directly observed. These endpoints, however, are key parameters in  $CO_2$  storage and multiphase flow modeling projects [16].

To determine the endpoints of the relative permeability curves, the Corey model is widely adopted. The Corey model is an empirical correlation developed to describe the relationship between relative permeability and fluid saturation. It expresses the relative permeability of each phase as a power-law function of the normalized saturation. The Corey-type equations applied for curve fitting are given as:

$$k_{rw}(S_w) = k_{rw}^{\text{max}} \left(\frac{S_w - S_{wi}}{1 - S_{wi}}\right)^{n_w}$$
(5.34)

$$k_{rCO_2}(S_w) = k_{rCO_2}^{\text{max}} \left( 1 - \frac{S_w - S_{wi}}{1 - S_{wi}} \right)^{n_{CO_2}}$$
(5.35)

Here,  $n_w$  and  $n_{CO_2}$  are the Corey exponents, typically ranging between 2 and 5, that control the curvature of the relative permeability functions. By tuning these exponents together with the endpoint values  $(k_{rw}^{\text{max}}, k_{rCO_2}^{\text{max}})$ , the experimental data can be matched, allowing the determination of the endpoint relative permeabilities.

In both SS and USS experiments, the intermediate points of the relative permeability curves are experimentally obtained, while the irreducible water saturation is determined beforehand. These measured relative permeability data points serve as reference values to be fitted using the Corey equations. A trial-and-error approach is then applied by adjusting the estimated endpoints and Corey exponents until an optimal match with the experimental data is achieved.

# Chapter 6

# Core Sample Selection and the Conditions of the Experiment Effect on Relative Permeability Curves

## 6.1 Choosing the Core Sample

Since relative permeability curves are directly influenced by wettability, and trapping and injectivity in CCS models depend on these curves, it is essential to use core samples that preserve the original wettability in order to obtain reliable measurements.

For example, if a strongly water-wet undergoes wettability alteration to a weaker waterwet state, the irreducible water saturation decreases while the residual saturation of the non-wetting phase is reduced. This results in a shift of the entire relative permeability curves, as illustrated in the following figure:

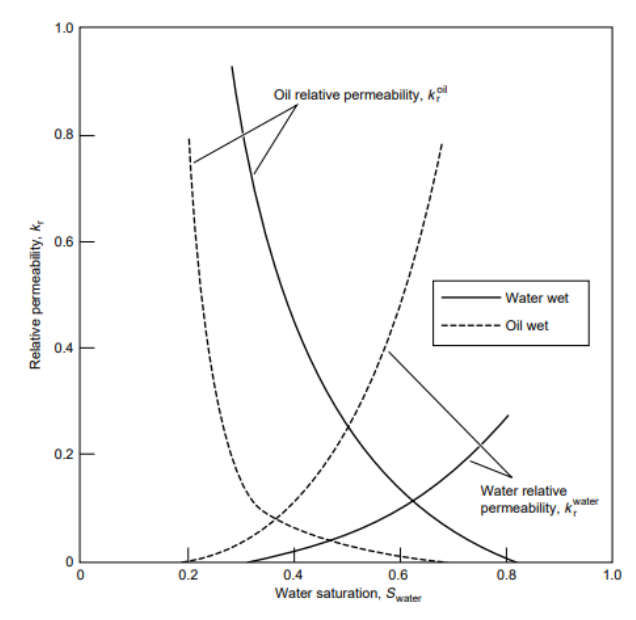


Figure 6.1: Effect of wettability on relative permeability curves [40]

For this reason, preserved/native cores are preferred, as they have higher probability of maintaining the original reservoir wettability compared to cleaned/dried cores, where cleaning fluids may remove natural surface coatings and alter wettability [21].

Another recommendation is to select core plugs away from the mud-invaded zone of the retrieved whole core, since drilling mud filtrate may change saturation and wettability. Recovered cores should be preserved without delay, as exposure to air and weathering may alter the wetting characteristics. In preserved cores, direct determination of porosity, absolute permeability, and irreducible saturation prior to testing is not possible, since destructive procedures cannot be applied. Instead, these properties are often estimated from end-trim data, and later validated from the core itself after completion of the experiment [21][30].

If preserved cores are unavailable and cleaned/dried samples must be used, they should be cleaned with non-reactive solvents to minimize alteration of wetting properties. The cores should then be aged by keeping them in contact with reservoir fluids under reservoir-like conditions for a period of several weeks, in order to restore wettability. Although the validity of this restoration process is debated, it remains the only practical option in the absence of preserved cores [21].

Because the capillary end effect becomes more pronounced when low-viscosity fluids such as supercritical  $CO_2$  are used, it is preferable to employ longer cores to ensure that a region unaffected by end effects exists within the sample. However, the achievable core length is often constrained by the limitations of the experimental apparatus.

Finally, since  $CO_2$ -brine relative permeability experiments should be done with brine that is equilibrated with  $CO_2$ , and original brine is not equilibrated, prior to the experiments flush the equilibrated brine at a low rate until the effluent composition matches that of the injected brine, thereby eliminating dissolution and chemistry transients that would

bias the curves.

## 6.2 Conditions of the Experiment

Carbon Capture and Storage (CCS) projects prefer injecting  $CO_2$  in its supercritical phase, since under these conditions  $CO_2$  combines a liquid-like density, which enables storing large volumes, with a gas-like viscosity, which facilitates flow. Supercritical conditions are reached at depths greater than  $\sim 800 \,\mathrm{m}$ , where  $CO_2$  exceeds its critical point (31°C and 72.9 atm) [14]. Above this threshold, a wide range of pressure and temperature states can be encountered in practice. In addition, formation brine salinity can vary from  $10,000 \,\mathrm{mg/L}$  to more than  $400,000 \,\mathrm{mg/L}$ . Variations in pressure, temperature, and salinity directly influence fluid properties such as viscosity, density, contact angle, and interfacial tension. These in turn control irreducible and residual saturations as well as the shape of the relative permeability curves. For this reason, experimental conditions must closely reproduce those of the reservoir core; otherwise, the measured relative permeability curves will not be representative [17].

## 6.2.1 Thermophysical Properties of the Fluids

## Density and Viscosity

(a)  $CO_2$  density variation with pressure and

temperature [17]

At storage conditions,  $CO_2$  is typically in the supercritical state and often close to its critical point. In this region, both density and viscosity vary strongly with pressure and temperature, as illustrated in the correlations of Span and Wagner for density and Fenghour et al. for viscosity:

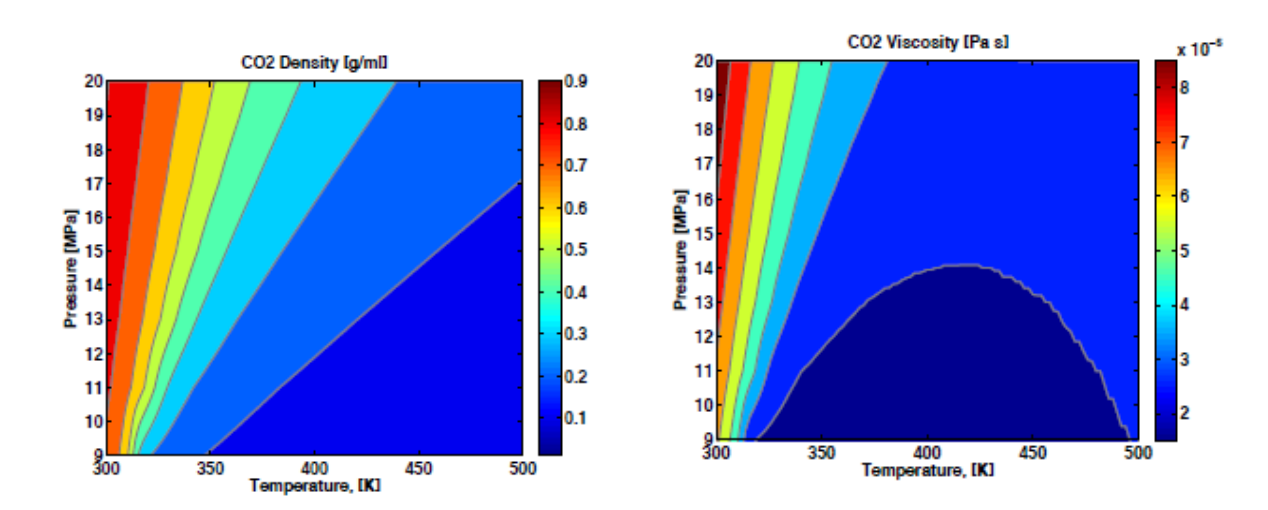
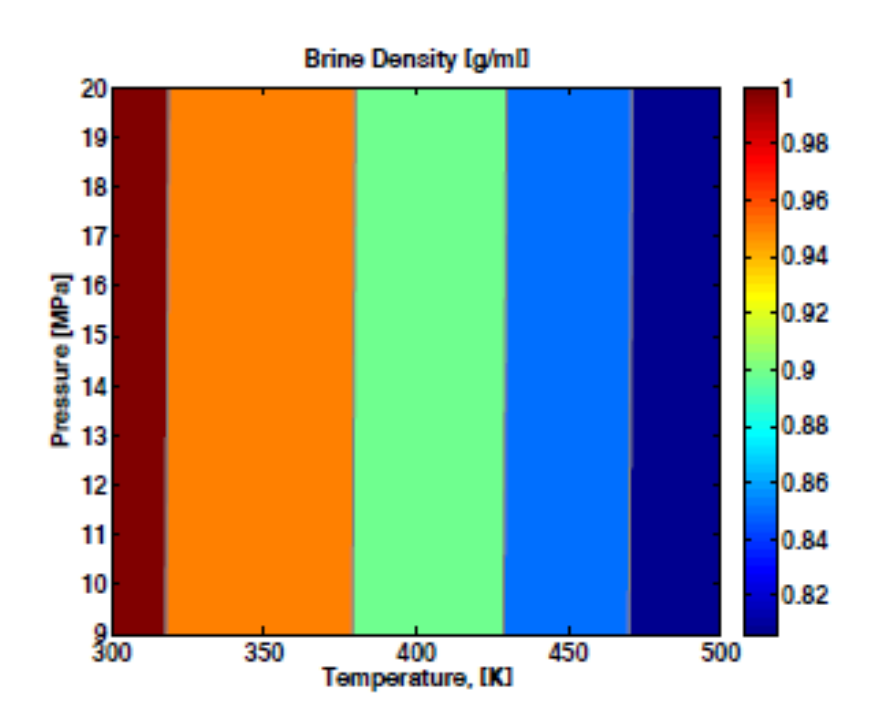


Figure 6.2:  $CO_2$  density and viscosity variation with pressure and temperature.

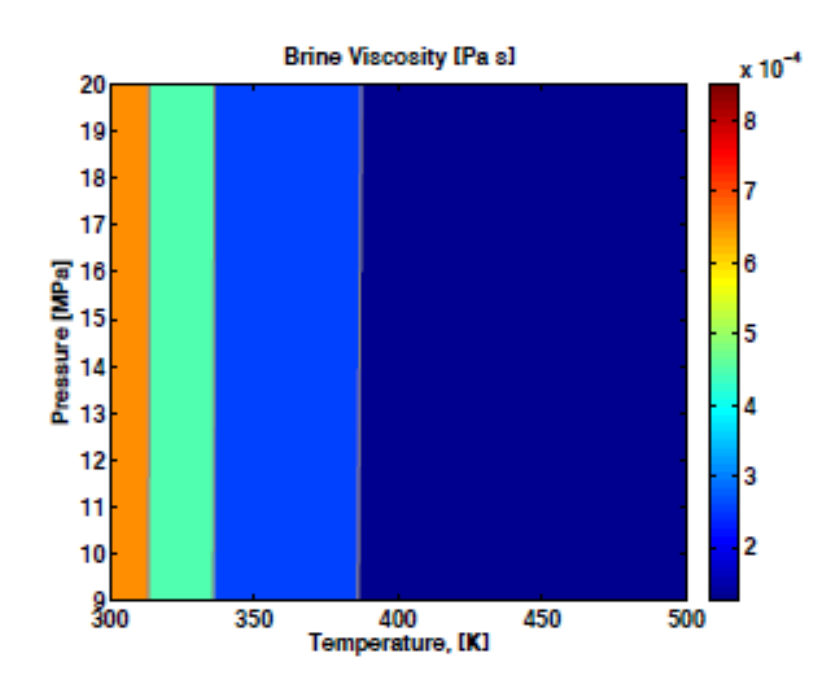
temperature [17]

(b)  $CO_2$  viscosity variation with pressure and

In contrast, brine requires a significant temperature variation to show noticeable changes in density and viscosity, while pressure has negligible influence. The density of brine, however, is strongly controlled by salinity: as salinity increases, density also increases. For instance, an aquifer with a salinity of  $10,000\,\mathrm{mg/L}$  will have a distinctly lower density than one with  $400,000\,\mathrm{mg/L}$  at the same pressure and temperature conditions.



(a) Brine density variation with pressure and temperature [17]



(b) Brine viscosity variation with pressure and temperature [17] Figure 6.3: Brine density and viscosity variation with pressure and temperature.

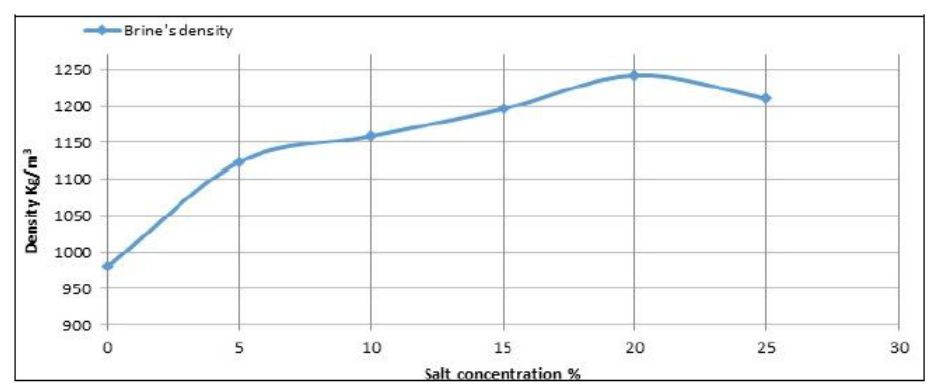


Figure 6.4: Brine density variation with salt concentration [41]

The decrease in brine density at high salt concentrations occurs due to the solubility limit. Once the brine becomes saturated, the excess salt remains as solid particles, increasing the total volume of the mixture without contributing to the dissolved mass. This apparent decrease therefore represents the limit of salt dissolution and not that the solution become lighter [41].

## Interfacial Tension $CO_2$ -Brine System

The interfacial tension of  $CO_2$ -brine systems is a function of pressure, temperature, and brine salinity. It ranges from 20 mN/m at low temperature, low salinity, and high pressure, to 55 mN/m at high temperature, high salinity, and low pressure conditions according to the dataset provided by Li et al. that is illustrated in the following figure [17]:

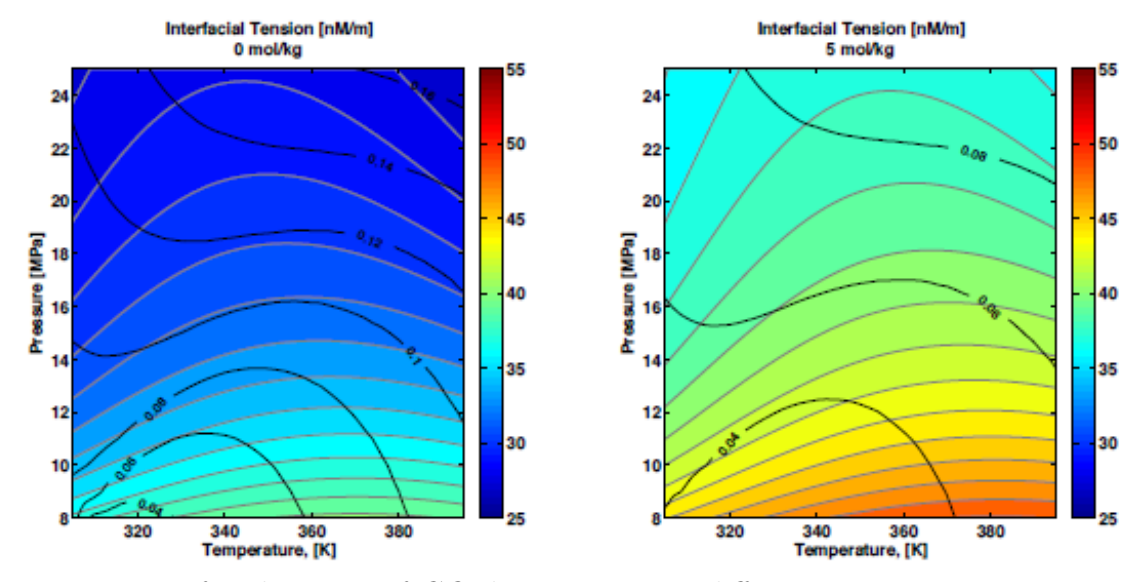


Figure 6.5: Interfacial tension of  $CO_2$ -brine system at different pressure, temperature, and salinity [17]

#### Wettability

Wettability is a rock-fluid interaction property that describes the preferential affinity of a rock surface for one fluid relative to another. Its variation is not determined solely by fluid conditions but strongly depends on the mineralogical composition of the rock. For quartz and calcite, the  $CO_2$ -brine system remains strongly water-wet, with negligible influence of pressure and salinity variations. In contrast, mica shows a transition from water-wet to intermediate-wet as both  $CO_2$  pressure and brine salinity increase. For silica, an increase in brine salinity from 0.01 M to 5 M NaCl leads to a gradual increase in contact angle, shifting the system from water-wet to mixed-wet conditions. In addition, as the pressure crosses the critical point, a sharp increase of about 20° in contact angle is observed, whereas beyond this point only minor variations occur [17].

# 6.2.2 Impact of Thermophysical Properties on Relative Permeability

Jeong et al.(2017) conducted several experiments to study the separate effect of viscosity ratio and interfacial tension on relative permeability curves.

## Influence of Viscosity Ratio

Two steady-state experiments were performed at different pressure and temperature conditions, selected to alter the viscosity of  $CO_2$  and thus the viscosity ratio, while keeping the interfacial tension constant. The viscosity ratios of the first and second experiments were 0.044 and 0.034, respectively, with an interfacial tension of 35.9 mN/m in both cases [42]. The results are illustrated in the following figure:

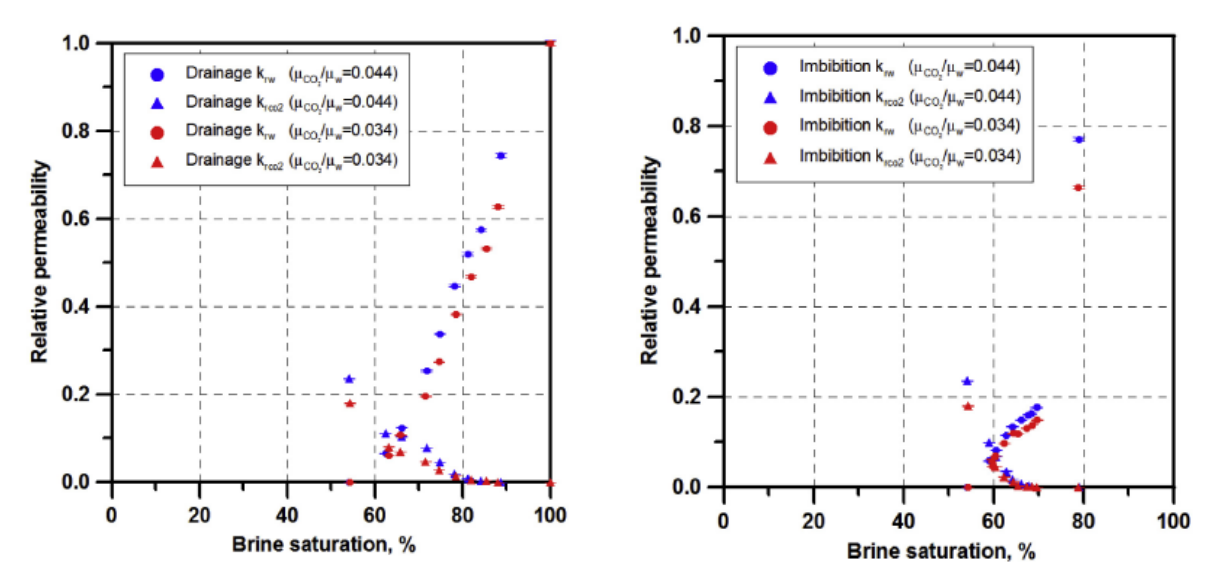


Figure 6.6: Comparison of  $CO_2$ —brine relative permeability curves at viscosity ratios of 0.034 and 0.044 under constant interfacial tension (35.9 mN/m) during drainage and imbibition [42]

The results show that the relative permeability of both phases increases as the viscosity ratio rises, while the residual brine saturation remains nearly unchanged. At the pore scale, brine adheres to the pore walls in thin films, whereas  $CO_2$  occupies the pore centers and must pass through pore throats. For flow to occur, viscous forces driving  $CO_2$  must overcome capillary resistance at the throats. As the viscosity ratio increases, the viscous contribution of  $CO_2$  relative to capillary forces becomes more significant, improving its

connectivity and flow efficiency. The increase in brine relative permeability is related to the reduction in brine viscosity when the viscosity ratio increases, which lowers the resistance to brine flow in its wetting films and channels. The high residual brine saturation persists because, despite the change in viscosity ratio, capillary trapping remains the dominant mechanism under the fixed flow rate conditions of the experiment [42].

#### Influence of Interfacial Tension

To have the same viscosity ratio but different interfacial tension, they performed one experiment with  $CO_2$  in gas phase and the other one in supercritical phase. The viscosity ratio for both experiments was 0.034, while IFT for  $scCO_2$ /brine is 35.9 mN/m and for  $gCO_2$  was 53.7 mN/m [42]. The results are illustrated in the following figure:

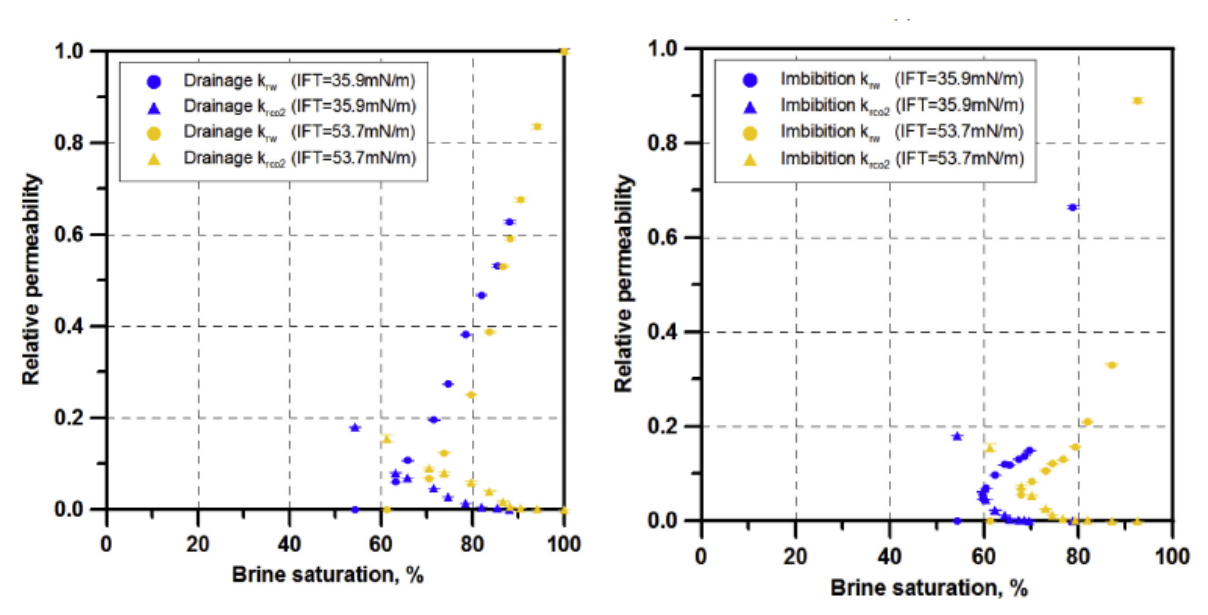


Figure 6.7: Comparison of  $CO_2$ -brine relative permeability curves at IFT of 35.9 mN/m and 53.7 mN/m under constant viscosity ratio (0.034) during drainage and imbibition [42]

The relative permeability curves shows a lower saturation of brine for lower IFT values during drainage, a shift to the lower brine saturation is observed in the relative permeability curves, where the residual brine saturation decreased from 61,23% to 54.12% when moving from higher to lower IFT. This can be explained by the adhesion force which is less when IFT decreases, that leads to less energy required to maintain the interface between two immiscible fluids and porous medium, which results in more effective removal of the wetting phase [42].

The relative permeability curves show lower brine saturation for lower IFT values during drainage. A clear shift toward lower brine saturation is observed, where the residual brine saturation decreased from 61.23% to 54.12% when moving from higher to lower IFT. This behavior can be explained by the adhesion force: as IFT decreases, the adhesion force between brine and the pore walls is reduced, which means less energy is required to maintain the interface between the immiscible fluids and the porous medium. Consequently, the wetting phase can be removed more effectively, leading to lower residual brine saturation and more efficient  $CO_2$  displacement. During imbibition, the brine saturation increases with increasing IFT, and therefore the  $CO_2$  saturation in the high-IFT system is lower

than in the low-IFT system. This occurs because as IFT increases, the adhesion force between the brine and the pore walls also increases, enabling brine to invade smaller pores more effectively. As a result, less CO<sub>2</sub> remains trapped in the pore space under high-IFT conditions [42].

## 6.2.3 Equilibration of the Fluids

It is crucial to equilibrate the brine and  $CO_2$  at the desired pressure, temperature, and salinity prior to performing relative permeability measurements. The fluids are chemically unstable in the absence of equilibration; during the experiment,  $CO_2$  will dissolve into the brine and the brine will evaporate into the  $CO_2$ -rich phase. During the displacement test, this uncontrolled mass movement modifies density, viscosity, interfacial tension, and phase compositions, causing systematic inaccuracies in the relative permeability curves that are recorded. The experiment begins with thermodynamically stable phases that are indicative of reservoir conditions since the fluids have been pre-equilibrated. This guarantees that only pore-scale displacement mechanisms, not temporary dissolution processes, are reflected in the measured flow behavior.

To equilibrate fluids, they are first placed in two separate cells at the experimental pressure and temperature: one for brine saturated with  $CO_2$  and one for  $CO_2$  saturated with brine. The equilibration volumes can be calculated using Henry's law. After equilibration, the fluids are transferred to pumps at experimental pressure but ambient temperature [16].

Because solubility depends on temperature at constant pressure, cooling alters the equilibrium state:

- Brine phase:  $CO_2$  solubility in brine decreases with temperature. When the equilibrated brine is cooled at constant pressure, it becomes *under-saturated* (it could hold more  $CO_2$ ). This does not cause exsolution. When reheated before injection, it still represents the correct equilibrated state at reservoir conditions.
- $CO_2$  phase: Water solubility in  $CO_2$  increases with temperature. When  $CO_2$  is cooled to ambient temperature, some water condenses out. When the  $CO_2$  is reheated, this condensed brine does not fully re-dissolve, leaving the injected  $CO_2$  under-equilibrated compared to reservoir conditions.

Thus, the brine phase remains representative, while the  $CO_2$  phase is slightly under-equilibrated; however, this under-equilibration has only a minor impact on relative permeability measurements at the core scale. This is supported by quantitative estimates: approximately 500 PV of under-equilibrated  $CO_2$  would need to be injected at reservoir conditions to dissolve about 20% of the residual brine saturation, which is far larger than the PV typically injected during the experiment. In contrast, if brine were injected under-equilibrated, only about 3 PV would be required to dissolve around 40% of the residual  $CO_2$ , which would strongly bias the relative permeability measurements[16].

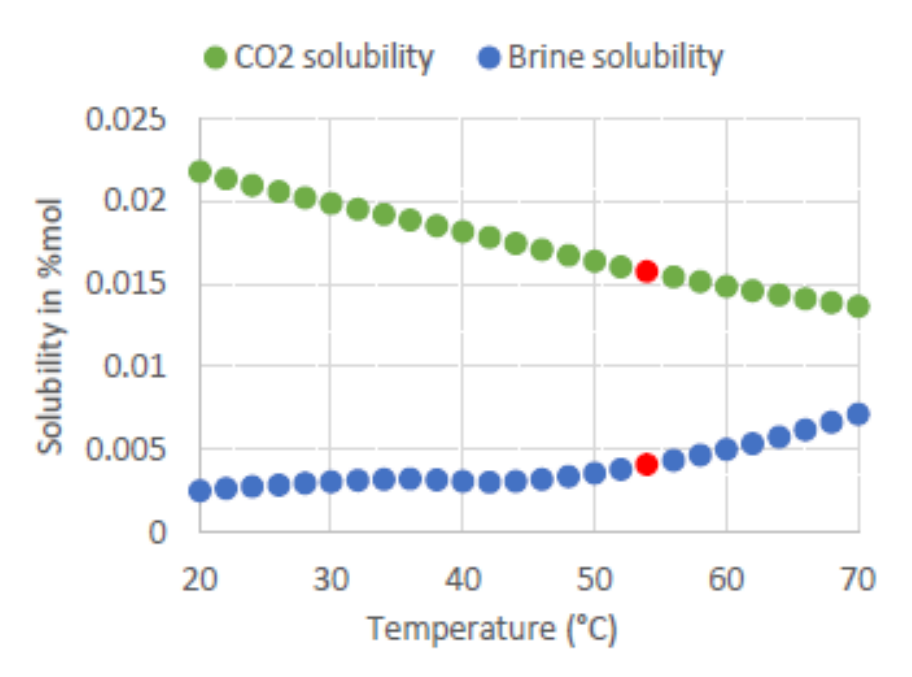


Figure 6.8: Illustration of the variation of  $CO_2$  and brine solubility with temperature at constant pressure (90 bars)[16]

# Chapter 7

# Discussion

Carbon dioxide is usually preferred to be stored in supercritical phase, where it is characterized by high density which allows higher storage capacity and low viscosity which enhance injectivity. In order for  $CO_2$  to be stored in its supercritical phase it must exceed its critical point (31°C and 73.8 bar), and this is achieved at depth higher than 1000 m to maintain stability. Under these reservoir conditions,  $scCO_2$  has a density ranging between 600 and 800 kg/m³, while the density of brine is approximately 1000 kg/m³. This pronounced density contrast promotes **gravity segregation**, where the denser brine tends to migrate downward and the lighter  $scCO_2$  rises upward.

In steady-state (SS) experiments, which assume a uniform saturation profile within the core once dynamic equilibrium is achieved, gravity segregation causes the upper region of the core to become dominated by  $scCO_2$ , while the lower zone remains brine-rich. This leads to a mixed flow pattern rather than a uniform two-phase distribution, resulting in biased relative permeability measurements. Furthermore, segregation delays the attainment of steady-state conditions, thereby prolonging the stabilization time required for accurate data collection.

In unsteady-state (USS) experiments, gravity segregation violates one of the fundamental assumptions behind the Johnson-Bossler-Naumann (JBN) method, which is one-dimensional horizontal flow. The density-driven movement of fluids creates vertical flow paths, and the displacement is no longer piston-like as assumed by the model. Consequently, the derived relative permeability curves become non-representative of the true rock-fluid system.

To minimize gravity-induced errors, it is recommended to orient the core and core holder vertically, thereby reducing segregation and improving the accuracy of relative permeability measurements.

Another important step when working with supercritical  $CO_2$ -brine systems is to equilibrate the fluids outside the core before injection. This step is essential to avoid any mass transfer between the two phases during injection and to ensure that the experiment starts with thermodynamically stable fluids. By doing so, the measured flow behavior reflects only the pore-scale displacement mechanisms rather than additional compositional effects.

For steady-state experiments, obtaining reliable measurements of relative permeability curves for  $scCO_2$ -brine systems requires maintaining a small pressure drop across the core whenever possible. This ensures that the properties of the compressible fluid,  $scCO_2$ , remain nearly constant along the core length. Since Darcy's law assumes the flow of incompressible fluids with constant viscosity and density, keeping the pressure gradient low ( $\Delta P < 40$ -50 psi) helps to satisfy this assumption and minimize property variation. However, when the core characteristics or experimental conditions result in a relatively high pressure drop, the variation in  $scCO_2$  properties becomes significant, and a correction factor should be applied to the measured relative permeability data to account for this compressibility effect.

Regarding the capillary end effect (CEE), which is more pronounced in  $scCO_2$ -brine systems than in conventional oil-brine systems, it introduces a laboratory artifact that distorts the uniform saturation profile and affects the measured pressure drop across the core. The most effective approach to overcome this issue is the Modified Intercept Method (MIM), a mathematical correction technique. This method requires a small region of the core that is not influenced by the capillary end effect (corresponding to the uniform saturation zone in the absence of CEE) and performing at least three experiments at a constant fractional flow ratio,  $F = q_w/q_{nw}$ , for each saturation level. Using the biased pressure drop and saturation data, the method extrapolates to determine the true values, effectively removing the end-effect distortion. Although this process is time-consuming and experimentally demanding, it provides more accurate and physically representative relative permeability curves.

When it comes to unsteady-state (USS) experiments, the situation becomes more complex as several fundamental assumptions are violated by  $scCO_2$ . The Johnson–Bossler–Naumann (JBN) method assumes a piston-like, one-dimensional displacement at the saturation front and relies on the pressure drop and effluent volumes to determine the relative permeability and saturations. However, in  $scCO_2$ –brine systems, the presence of the **capillary end effect (CEE)** causes the outlet fractional flow to deviate from that expected under a piston-like displacement. Near the outlet, the capillary pressure approaches zero, resulting in an accumulation of the wetting phase near the outlet. Consequently, the outlet fractional flow is no longer governed solely by saturation variation but also by local capillary redistribution. This leads to biased determinations of the outlet saturation and relative permeability, and the average water saturation in the core becomes higher than expected due to fluid accumulation near the outlet.

To mitigate these effects in imbibition experiments, the pressure drop can be measured locally by drilling pressure taps along the core and installing pressure transducers, while the saturation in each section is determined by CT scanning. The fractional flow can then be calculated using the fractional flow approach discussed previously. This localized measurement strategy provides faster estimation of relative permeability with reduced influence of end effects, though the results remain less precise because the distortions are mitigated rather than completely eliminated.

For drainage experiments, the results are often less reliable due to the presence of **viscous fingering**, which arises from the large viscosity contrast between  $scCO_2$  and brine. This phenomenon disrupts the piston-like displacement assumption of the JBN method, even when using local measurements. Therefore, USS drainage experiments involving  $scCO_2$ 

should be interpreted with caution, and wherever possible, the results should be validated against steady-state measurements corrected for end effects.

# Chapter 8

# Conclusion

The goal of this thesis was to identify the most reliable approach for measuring relative permeability curves in  $CO_2$ -brine systems, as these curves are crucial for predicting plume migration, injectivity, and residual trapping in CCS projects. The two main experimental approaches were considered: the steady-state (SS) co-injection method and the unsteady-state (USS) displacement method. The greatest challenge in both approaches is the capillary end effect (CEE), a laboratory artifact that distorts saturation and pressure measurements and leads to biased relative permeability curves. This effect is particularly severe in  $CO_2$ -brine systems due to the low viscosity of  $CO_2$ , which results in a mobility ratio below unity and makes capillary forces dominate over viscous forces.

Different strategies have been proposed to mitigate CEE, such as increasing flow rates, using longer cores, or employing more viscous fluids. However, these approaches are not always feasible and cannot guarantee the complete removal of the artifact.

For SS experiments, a mathematical approach that totally removes CEE from calculation, named the modified intercept method, is one consistet solution. It requires running at least 3 SS experiment at constant  $F = \frac{q_w}{q_{\text{CO2}}}$ , to obtain the saturation of the unaffected region from the y-intercept of average water saturation vs. reciprocal flow rate of  $CO_2$ , and the relative permeability from the phase mobility obtained from the slope of pressure drop vs  $CO_2$  flow rate. This process is repeated for different F to obtain full relative permeability curves. This method relies only on mass balance and general pressure equations, and requires only a small unaffected region of the core, which can be achieved using long cores. Numerical forward models verified the approach: back-calculated points lie on the "true" curves when CEE is present, establishing both the rigor and robustness of the correction.

For USS, an extended JBN analysis that relies on local measurements, mitigate CEE. Local pressure taps provide sectional pressure drops; in-situ X-ray CT yields spatial saturation fields; and the JBN inversion is applied locally along the core by estimating the fractional flow from the fractional flow method. This works for imbibition, while for drainage it produces unreliable results due to viscous fingering,

For both experiments, endpoints are hard to reach, Corey's model can be used to obtain relative permeabilities at irreducible and residual saturations.

Beyond the choice of experimental method, obtaining representative relative permeability curves requires strict attention to core and fluid preparation as well as reservoir-like conditions. If preserved cores are not used, cleaning and drying can alter the natural wettability of the rock, leading to reduced irreducible brine saturation and lower residual  $CO_2$  saturation. Similarly, if experiments are conducted at pressures, temperatures, or salinities different from reservoir conditions, the fluid properties—such as density, viscosity, interfacial tension, and contact angle—will be altered. This directly affects the shape of the curves, and residual saturations. In addition, neglecting fluid equilibration causes uncontrolled mass transfer:  $CO_2$  dissolves into brine and water evaporates into the  $CO_2$ -rich phase, which modifies density, viscosity, interfacial tension, and phase compositions, causing systematic inaccuracies in the relative permeability curves that are recorded. Therefore, reliable experimental outcomes depend not only on mitigating capillary end effects but also on ensuring preserved rock samples, representative reservoir thermodynamic conditions, and properly equilibrated fluids, so that the measured relative permeability curves truly reflect in-situ displacement mechanisms.

In conclusion, SS experiments provide the most precise results for  $scCO_2$ -brine systems, but the procedure is time consuming and exhausting, while the USS experiments can provide a qualitative fast results for imbibition, but a totally non-reliable results for drainage due to viscous fingering phenomena.

# Bibliography

- [1] European Commission. The European Green Deal. https://commission.europa.eu/strategy-and-policy/priorities-2019-2024/european-green-deal\_en. Accessed: 2025-07-24 (cit. on p. 1).
- [2] United States Environmental Protection Agency. Global Greenhouse Gas Emissions Data. Accessed: July 29, 2025. 2023. URL: https://www.epa.gov/ghgemissions/global-greenhouse-gas-overview (cit. on p. 1).
- [3] United Nations Framework Convention on Climate Change. *The Paris Agreement*. Accessed: July 29, 2025. 2015. URL: https://unfccc.int/process-and-meetings/the-paris-agreement (cit. on p. 2).
- [4] S. Rezaei, A. Hormaza Mejia, Y. Wu, J. Reed, and J. Brouwer. «Global warming impacts of the transition from fossil fuel conversion and infrastructure to hydrogen». In: *Applied Energy* 397 (July 2025), pp. 1–2. DOI: 10.1016/j.apenergy.2025. 126363 (cit. on p. 2).
- [5] Berkeley Earth. Global Temperature Report for 2022. Accessed: July 29, 2025. 2023. URL: https://berkeleyearth.org/global-temperature-report-for-2022/(cit. on p. 2).
- [6] Natural Resources Defense Council. *Greenhouse Effect 101*. Accessed: July 30, 2025. 2023. URL: https://www.nrdc.org/stories/greenhouse-effect-101#gases (cit. on p. 2).
- [7] Hannah Ritchie and Max Roser. CO emissions. https://ourworldindata.org/co2-emissions. Accessed: 2025-07-24. 2023 (cit. on p. 2).
- [8] National Grid. What Is Carbon Capture and Storage (CCS) and How Does It Work. Accessed: 06-Aug-2025. 2024. URL: https://www.nationalgrid.com/stories/energy-explained/what-is-ccs-how-does-it-work (cit. on p. 3).
- [9] Bert Metz, Ogunlade Davidson, Heleen de Coninck, Manuela Loos, and Leo Meyer. IPCC Special Report on Carbon Dioxide Capture and Storage. Prepared by Working Group III of the Intergovernmental Panel on Climate Change. Cambridge, United Kingdom and New York, NY, USA: Cambridge University Press, 2005. ISBN: 978-0-521-86643-9 (cit. on pp. 3, 5).
- [10] Mari Voldsund et al. «Low carbon power generation for offshore oil and gas production». In: *Energy Conversion and Management:* X 17 (2023). Available online 3 January 2023, p. 8. DOI: 10.1016/j.ecmx.2023.100347. URL: https://doi.org/10.1016/j.ecmx.2023.100347 (cit. on p. 3).

- [11] U.S. Department of Energy, Office of Fossil Energy and Carbon Management. *Pre-Combustion Carbon Capture Research*. https://www.energy.gov/fecm/pre-combustion-carbon-capture-research. Accessed: 2025-08-07. 2025 (cit. on p. 4).
- [12] British Geological Survey. *Understanding carbon capture and storage*. https://www.bgs.ac.uk/discovering-geology/climate-change/carbon-capture-and-storage/. Accessed: 2025-08-07. 2025 (cit. on p. 4).
- [13] Global CCS Institute. Fact Sheet: Transporting CO. https://www.globalccsin stitute.com/archive/hub/publications/191083/fact-sheet-transporting-co2.pdf. Accessed: 2025-08-08. 2015 (cit. on p. 4).
- [14] National Energy Technology Laboratory. Carbon Storage FAQs. https://www.netl.doe.gov/carbon-management/carbon-storage/faqs/carbon-storage-faqs. Accessed: 2025-08-09. 2019 (cit. on pp. 4, 59).
- [15] A. Sahlani. «Impact of Relative Permeabilities on CO Geological Storage». Master's Thesis. MA thesis. Politecnico di Torino, 2022 (cit. on pp. 5, 6).
- [16] Matthieu Mascle, Ameline Oisel, Per Kristian Munkerud, Einar Ebeltoft, Olivier Lopez, Colin Pryme, and Souhail Youssef. «CO<sub>2</sub>-Brine Relative Permeability Measurements at Reservoir Conditions: How to Reconciliate SS and USS Methods?» In: Proc. 36th Int. Symp. Soc. Core Analysts (SCA). Paper SCA2023-002. 2023 (cit. on pp. 6, 25–27, 42, 55, 64, 65).
- [17] S. Benson, R. Pini, C. Reynolds, and S. Krevor. *Relative Permeability Analyses to Describe Multi-Phase Flow in CO<sub>2</sub> Storage Reservoirs*. Tech. rep. Accessed: 2025-08-09. Global CCS Institute, Targeted Report No. 2, 2012 (cit. on pp. 6, 59–62).
- [18] Sally M. Benson, Ferdinand Hingerl, Lin Zuo, Ronny Pini, Sam Krevor, Catriona Reynolds, Ben Niu, Ran Calvo, and Auli Niemi. Relative Permeability for Multi-Phase Flow in CO Storage Reservoirs. Part II: Resolving Fundamental Issues and Filling Data Gaps. Research Report. Prepared for the Global CCS Institute. Stanford, California: Stanford University, 2015. URL: https://www.globalccsinstitute.com/publications/relative-permeability-analysis-describe-multi-phase-flow-co2-storage-reservoirs (cit. on p. 6).
- [19] Tarek H. Ahmed. Reservoir Engineering Handbook. 4th. Burlington, MA, USA: Gulf Professional Publishing, Elsevier, 2010. ISBN: 978-1-85617-803-7 (cit. on p. 7).
- [20] Tarek H. Ahmed. Reservoir Engineering Handbook. 4th. Burlington, MA, USA; Kidlington, Oxford, UK: Gulf Professional Publishing (Elsevier), 2010. ISBN: 978-1-85617-803-7 (cit. on pp. 7, 10, 12, 15–17, 34).
- [21] Abhijit Y. Dandekar. *Petroleum Reservoir Rock and Fluid Properties*. 2nd. Boca Raton, FL, USA: CRC Press, Taylor & Francis Group, 2013. ISBN: 978-1-4398-7645-9 (cit. on pp. 7–16, 18, 24, 25, 27–37, 40, 41, 58).
- [22] Richard Nolen-Hoeksema. «Defining Permeability». In: Oilfield Review (Mar. 2021). Part of the Inside SLB Transformative Technology series. URL: https://careers.slb.com/inside-slb/transformative-technology/defining-permeability (cit. on p. 11).
- [23] Biolin Scientific. What is the difference between surface and interfacial tension? Accessed: 2025-08-15. May 2018. URL: https://www.biolinscientific.com/blog/what-is-the-difference-between-surface-and-interfacial-tension (cit. on p. 14).

- [24] Endz Education Technical Team (EditorEndz). Cohesive force –. Accessed: 2025-08-15. 2025. URL: https://endz.in/cohesive-force-%e0%b4%95%e0%b5%8a%e0%b4%b9%e0%b4%bf%e0%b4%b7%e0%b5%bb-%e0%b4%ac%e0%b4%b2%e0%b4%82/ (cit. on p. 14).
- [25] Nanoscience Instruments. Surface & Interfacial Tension. Nanoscience Instruments Techniques: Tensiometry. Accessed: 2025-08-16. URL: https://www.nanoscience.com/techniques/tensiometry/surface-and-interfacial-tension/(cit. on p. 15).
- [26] Reza Masoodi, Ehsan Languri, and Alireza Ostadhossein. «Dynamics of liquid rise in a vertical capillary tube». In: *Journal of Colloid and Interface Science* 389 (2013), pp. 268–272. DOI: 10.1016/j.jcis.2012.09.004 (cit. on p. 16).
- [27] A. Mohammadi Alamooti and F. Karimi Malekabadi. «Fundamentals of Enhanced Oil and Gas Recovery from Conventional and Unconventional Reservoirs». In: *Title of the Book (if any)*. Chapter, ScienceDirect. Available: https://www.sciencedirect.com/science/article/Elsevier, 2018. DOI: 10.1016/B978-0-12-813027-8.00001-1 (cit. on p. 18).
- [28] Haiqing Wu, Bing Bai, Xiaochun Li, Shuai Gao, Mingze Liu, and Lei Wang. «An explicit integral solution for pressure build-up during CO<sub>2</sub> injection into infinite saline aquifers». In: *Greenhouse Gases: Science and Technology* 6.2 (2016), pp. 1–15. DOI: 10.1002/ghg.1601 (cit. on p. 18).
- [29] VINCI Technologies. RPS-700 Relative Permeameter System User Guide, Version 1.0. Operating Manual, Revision 1.0, April 15, 2014. VINCI Technologies Inc. Nanterre, France, 2014 (cit. on p. 19).
- [30] M. Honarpour and S. M. Mahmood. «Relative-Permeability Measurements: An Overview». In: Journal of Petroleum Technology 40.8 (1988). SPE 18565, pp. 963–966. DOI: 10.2118/18565-PA (cit. on pp. 24, 25, 28, 58).
- [31] C.-W. Kuo and S. M. Benson. «Reliability of Relative Permeability Measurements for Heterogeneous Rocks Using Horizontal Core Flood Experiments». In: Sustainability 13.5 (2021), p. 2744. DOI: 10.3390/su13052744. URL: https://doi.org/10.3390/su13052744 (cit. on p. 25).
- [32] National Institute of Standards and Technology. National Institute of Standards and Technology (NIST). https://www.nist.gov/. Accessed: 21-Oct-2025 (cit. on pp. 26, 38).
- [33] T.S. Ramakrishnan and N.V. Chugunov. «Compressibility corrections to relative permeability from the non-uniform steady-state method». In: *Chemical Engineering Science* 95 (2013), pp. 73–77. DOI: 10.1016/j.ces.2013.03.009 (cit. on p. 27).
- [34] Liam C. Morrow, Callum Cuttle, and Christopher W. MacMinn. «Gas Compression Systematically Delays the Onset of Viscous Fingering». In: *Physical Review Letters* 131.22 (2023), p. 224002. DOI: 10.1103/PhysRevLett.131.224002 (cit. on p. 37).
- [35] Taylor & Francis. Viscous Fingering. Accessed: Oct. 27, 2025. 2025. URL: https://taylorandfrancis.com/knowledge/Engineering\_and\_technology/Chemical\_engineering/Viscous\_fingering/ (cit. on p. 38).
- [36] Yulia Petrova. Viscous Fingering Phenomenon. Accessed: Oct. 28, 2025. 2025. URL: https://yulia-petrova.github.io/project/viscous\_fingering/ (cit. on p. 38).

- [37] Saleh Goodarzian and K. S. Sorbie. «Correct relative permeability data from steady-state experiments for capillary end effects». In: *Geoenergy Science and Engineering* 224 (2023), p. 211626. DOI: 10.1016/j.geoen.2023.211626. URL: https://doi.org/10.1016/j.geoen.2023.211626 (cit. on pp. 40, 42-49).
- [38] Yanyan Li, Shuoliang Wang, Zhihong Kang, Qinghong Yuan, Xiaoqiang Xue, Chunlei Yu, and Xiaodong Zhang. «Research on the Correction Method of the Capillary End Effect of the Relative Permeability Curve of the Steady State». In: *Energies* 14.15 (2021), p. 4528. DOI: 10.3390/en14154528. URL: https://doi.org/10.3390/en14154528 (cit. on p. 40).
- [39] Xiongyu Chen, Amir Kianinejad, and David A. DiCarlo. «An Extended JBN Method of Determining Unsteady-State Two-Phase Relative Permeability». In: Water Resources Research 52.10 (2016), pp. 8374–8383. DOI: 10.1002/2016WR019204 (cit. on pp. 50–55).
- [40] J. J. Buckles, R. D. Hazlett, S. Chen, K. G. Eggert, D. W. Grunau, and W. E. Soll. «Toward Improved Prediction of Reservoir Flow Performance». In: Los Alamos Science 22 (1994), pp. 112–121. URL: https://www.researchgate.net/publication/248126597 (cit. on p. 58).
- [41] Azhar Ahmed Abed. «An experimental study on the effect of salt concentration on physical properties». In: *International Journal of Mechanical and Thermal Engineering* 5.2 (2024), pp. 49–57. DOI: 10.22271/27078043.2024.v5.i2a.68. URL: https://www.mechanicaljournals.com/ijmte (cit. on p. 61).
- [42] G. S. Jeong, J. Lee, S. Ki, D. G. Huh, and C. H. Park. «Effects of viscosity ratio, interfacial tension and flow rate on hysteric relative permeability of CO<sub>2</sub>/brine systems». In: *Energy* 133 (2017), pp. 62–69. DOI: 10.1016/j.energy.2017.05.138 (cit. on pp. 62–64).